SYNRIFT AND POSTRIFT DEFORMATION OF THE FUNDY RIFT BASIN, NOVA SCOTIA, CANADA: EVIDENCE FROM MESOSCALE FRACTURE DATA

By

CÉSAR SEQUEIRA PERAZA

A thesis submitted to the

Graduate School – New Brunswick

Rutgers, The State University of New Jersey

in partial fulfillment of the requirements

for the degree of

Master of Science

Graduate Program in Geological Sciences

written under the direction of

Dr. Martha O. Withjack

Dr. Roy W. Schlische

and approved by

____

____

____

____

New Brunswick, New Jersey

October 2014

ABSTRACT OF THE THESIS

Synrift and Postrift Deformation of the Fundy Rift Basin, Nova Scotia, Canada:

Evidence from Mesoscale Fracture Data

By César Sequeira Peraza

Thesis Directors:

Dr. Martha O. Withjack

Dr. Roy W. Schlische

Previous studies have shown that multiple phases of deformation affected the passive margin of eastern North America during and after rifting. The number, style and timing of postrift deformational events, however, are poorly constrained. To address this issue, I collected fracture data (faults with slickenlines, conjugate faults and tension fractures) from the Fundy rift basin and applied a stress inversion method. My analysis of these data suggests that at least two distinct faulting regimes and tectonic phases affected the basin during and after rifting. The relative chronology of the tectonic phases, based on crosscutting relationships and overprinting slickenlines, is: 1) rifting characterized by normal faulting and produced by SE displacement of the hanging wall, and 2) basin inversion, characterized by strike-slip faulting and produced by an average NE movement of the hanging wall. The relationship between the strain states and displacement directions suggests that counterclockwise vertical-axes rotations of fractures likely occurred during the second event due to left-lateral strike slip on the border-fault zone.

Seismic data from the Fundy, Orpheus and Scotian basins, which share a common border-fault zone, provide insight on the absolute timing of the tectonic phases. The

Fundy data show that Late Triassic/Early Jurassic strata thicken toward the border-fault zone. Thus, the normal-faulting phase likely occurred during Late Triassic/Early Jurassic rifting. Seismic data from the Orpheus and Scotian basins, with a more complete stratigraphic record, show multiple episodes of postrift deformation mostly evidenced by three major angular unconformities. Although the NE-directed shortening produced during basin inversion is similar to the present-day strain state, its correlation with the postrift unconformities is unclear.

ACKNOWLEDGMENTS

The completion of this study was possible thanks to the involvement of many awesome people along the process. First of all, thanks to my parents Viviana and Irving, whose care, love and hard work have allowed me to reach the most brilliant goals in life. Equal gratitude goes to my sisters Karina, Natalie and Vivian, and my rugrats Santi and Seyi, for being my constant source of cheer and inspiration.

I give special thanks to my advisors Martha Withjack and Roy Schlische for providing me with so much guidance and mentoring along this long path without putting aside the values of friendship. I also thank Husky Energy, Inc. for the field and summer support.

My gratitude also goes to each of my friends at EPS for being part of my growing geofamily. Finally, I send my most sincere appreciation to all my friends in and from the happiest country of the world, those who always kept me in their thoughts and stood by my side at all times.

TABLE OF CONTENTS

LIST OF TABLES

LIST OF FIGURES

1. INTRODUCTION

The passive margin of eastern North America (Fig. 1) is a favorable location to understand postrift deformation associated with basin inversion. Mesozoic rift basins, such as the Fundy, Hartford and Newark basins, have structures that indicate synrift and postrift deformation (De Boer & Clifton, 1988; De Boer, 1992; Wade et al., 1996, Olsen, 1997; Withjack et al., 1995, 2009, 2010; Baum, 2002, 2006; Schlische, 2003; Schlische et al., 2003). Conversely, the structural record in Paleozoic and older rocks commonly includes prerift and younger tectonic events (Wade et al., 1996; Murphy et al., 2011), complicating the relative chronology. Seismic data from offshore rift basins, such as the Orpheus and Jeanne d'Arc basins (Sinclair, 1995; Durcanin, 2009; Syamsir, 2010; Etikha, 2012; Hanafi, 2013), provide valuable information on timing of deformation; however, they do not offer details on slip indicators to reconstruct stress states and displacement directions of major and mesoscale faults.

Previous studies demonstrated a phase of positive tectonic inversion in the Fundy rift basin. Withjack et al. (1995) explained that some folds, reverse faults, uplift and tilting are the consequence of NW shortening. In the Emerald/Naskapi basin (offshore Nova Scotia), anomalous structures possibly associated with shortening developed before the formation of the early Middle Jurassic breakup unconformity (Withjack et al., 1995). Elder Brady (2003), using field data from small-scale structures, recognized NW-SE extension followed by NE-SW shortening. Baum et al. (2008) confirmed the latter event by analyzing field structural data and multi-phase analogue clay models. Withjack et al. (2010) proposed that, during NE displacement of the basin, strain partitioning occurred in the hanging wall of the Cobequid-Chedabucto border-fault zone (Fig. 2); therefore, large-scale buttress/detachment folds and left-lateral strike-slip faults are both present. Regardless of limited controls on the timing of postrift deformation (e.g. absence of syntectonic datable minerals), seismic data from the Orpheus rift basin and the Scotian basin suggest that three postrift events with uplift and fault reactivation during the Early Jurassic, Early Cretaceous and Late Oligocene/Miocene alternated with subsidence and salt movement (Louden, 2002; Durcanin, 2009; Syamsir, 2010; Hanafi, 2013).

Despite evidence of tectonic inversion in the Fundy rift basin, reconstructing the postrift deformation history becomes problematic in terms of number of tectonic episodes, their kinematic characteristics and age. Based on the existing data, I hypothesize that at least two episodes of deformation occurred in the Fundy basin as a result of rifting and subsequent shortening. Therefore, the present study seeks to answer the following questions:

1) How many deformational episodes occurred?
2) What is the stress state associated with each tectonic episode?
3) What are the relative ages of the postrift deformation episodes?

To address the first two questions, I use stress inversion of mesoscale faults, conjugate faults and tension fractures collected in the Minas subbasin, the eastern branch of the Fundy rift basin (Fig. 2). I constrain the relative ages using overprinting slickenlines, and more indirectly, identifying synrift and postrift deformation in seismic lines from onshore and offshore Nova Scotia. The results from this study may be relevant to other inverted rift basins in eastern North America and other passive margins, such as Norway (e.g., Lundin et al., 2013) and Brazil (e.g., Cobbold et al., 2010).

1.1.Study Area and Stratigraphy

The Fundy rift basin is a half graben with beds generally dipping to the NW (Withjack et al., 2012b) divided into three structural subbasins, each one with its respective border faults (Fig. 2). The NE-striking Fundy and Chignecto border-fault zones bound the Fundy and Chignecto subbasins, respectively. The ENE-striking Cobequid-Chedabucto fault zone bounds the Minas subbasin as well as the adjacent Orpheus basin (Figs. 1, 2). This study focuses on the northern part of the Minas subbasin (Fig. 3).

The Horton, Windsor and Mabou Groups form the prerift units (undifferentiated in Fig. 4). They are of Late Devonian to Late Carboniferous age, and accumulated during and/or between the Acadian and Alleghanian orogenies (Ryan & Boehner, 1994; Keppie, 2000; Hamblin, 2001). Therefore, the rocks from this unit exhibit more faulting and folding than younger rocks, and cleavage is present.

The Honeycomb Point Formation may represent the earliest stages of rifting (Fig. 4; Olsen et al., 2000), but is absent in the study area. Wade et al. (1996) described it as conglomerates of alluvial fan origin, and interbedded fluvial and eolian sandstones. The age of the unit is uncertain, although it possibly is as old as Permian (Olsen et al., 2000).

In the study area, the Wolfville Formation unconformably overlies the prerift section and possibly the oldest synrift rocks (Fig. 4), and has a possible Anisian ("Lower Economy beds" of Middle Triassic age; Olsen, 1997) to Carnian age (Late Triassic). The Wolfville Formation is predominantly fluvio-alluvial bioturbated sandstones and clast-supported conglomerates, with two thick beds of eolian sandstones near the base (Olsen et al., 2000; Leleu & Hartley, 2010).

At the northern edge of the Minas subbasin, the Blomidon Formation unconformably overlies the Wolfville Formation, and locally, the prerift section (Fig. 4; Olsen et al., 2000). Seismic data also likely shows this unconformity (line BF-20 in Withjack et al., 2009). The "lower" part of the unit, previously interpreted as uppermost Wolfville Formation (Hubert & Mertz, 1984; Olsen et al., 1989; Olsen, 1997), consists of eolian sandstones and minor fluvial conglomerate and sandstones. The "upper" part represents a predominantly shallow lacustrine facies, consisting of laterally continuous red mudstones with minor evaporites and sandstones (Olsen et al., 2000). The uppermost portion of the Blomidon Formation consists of thin red, grey and black mudstones, thermally metamorphed by the emplacement of the overlying North Mountain Basalt (NMB; Olsen et al., 2000). The age of the Blomidon Formation is Norian to Rhaetian (Late Triassic; Olsen et al., 2000).

The NMB is part of a large igneous province known as Central Atlantic Magmatic Province (CAMP), which occurred during rifting in the central segment of the eastern North America margin (Schlische et al., 2003; Withjack et al., 1998, 2012b). Kontak (2008) subdivided the NMB in the Fundy basin into three flow units. Sediment-filled fissures, which are abundant in the middle unit, occupy columnar joints (Schlische & Ackermann, 1995). The feeders of the NMB are uncertain; however, its age and geochemical composition similar to the Shelburne and Avalon dikes in eastern Canada (Pe-Piper et al., 1997; Dunn at al., 1998; McHone, 2003). $^{238}U/^{206}Pb$ (Schoene et al., 2010; Blackburn et al., 2013) and $^{40}Ar/^{39}Ar$ (Jourdan et al., 2009) analyses yield an age of ~201 Ma.

On the northern shore of the Minas Basin, the McCoy Brook Formation consists of talus-slope basaltic breccias near faults, indicating syntectonic deposition (Olsen & Schlische, 1990; Tanner & Hubert, 1991). Other facies, such as alluvial-fan conglomerates, fluvial sandstones and mudstones, lacustrine red sandstones and shales, and eolian dune sandstones are also present (Tanner & Hubert, 1991; Tanner, 1995; Wade et al., 1996), including minor gypsum-rich and limestones horizons (Olsen, 1997). Palynological assemblages in the Scots Bay Member suggest a basal age of latest Late Triassic (Fig. 4; Lucas et al., 2011). Finally, the upper contact of the unit is an unconformity with unconsolidated Quaternary gravels and sands of glacial origin (Stea & Wightman, 1987).

2. METHODOLOGY

This study involves kinematic analysis of quantitative and qualitative fracture data from the northern part of the Minas subbasin. This section describes the process of acquisition and analysis of the data to obtain paleostress orientations and relative timing of tectonic events.

2.1. Types of Fractures

The data are from Economy Point, Five Islands, Blue Sac and Wasson Bluff, all located along the northern part of the Minas subbasin (Figs. 2, 3). The data (see Appendix A) consist of dip angle and dip direction of mesoscale fractures, namely faults, conjugate faults, and tension fractures (Figs. 5, 6). In this thesis, the class ‘faults’ applies exclusively to those with slip indicators; thus, the data include values of trend and plunge of slickenlines, as well as sense of relative movement based on kinematic indicators (e.g., Petit, 1987; Doblas, 1998). The term 'conjugate faults' refers to pairs of primary slickensided faults that intersect at an angle of approximately 60º, which presumably formed under the same stress state at approximately 30º from the maximum principal stress direction (σ_1). 'Tension fractures' are those with no evident shear, and could be voids or filled with minerals or sediments (e.g., Hancock, 1985; Schlische & Ackermann, 1995). A number of fractures exhibit additional features such as cross-cutting relationships and overprinting slickenlines. These features provide valuable insights into the number and relative timing of tectonic events.

2.2.Data Separation and Stress Inversion (Fig. 7)

Given the occurrence of a synrift phase, at least one postrift tectonic event (Elder Brady, 2003; Baum, 2006; Withjack et al., 2009, 2010), and the structural variability between sites (i.e., differences in faulting styles and fold development), the field data are heterogeneous and require independent processing from one location to another. Therefore, I first separate the data into four subgroups, corresponding to the four field sites.

For each site, I use Win_TENSOR v.4.0.2 software (Sperner et al., 1993; Delvaux & Sperner, 2003) to iteratively separate data and compute reduced stress tensors composed of four basic parameters: the principal stress axes, σ_1 (maximum), σ_2 (intermediate) and σ_3 (minimum), and the stress ratio $R = (\sigma_2-\sigma_3)/(\sigma_1-\sigma_3)$. σ_2 and σ_3 are perpendicular to σ_1. The vertical stress axis by itself determines the stress regime: normal faulting when σ_1 is vertical, strike-slip faulting when σ_2 is vertical, and reverse faulting when σ_3 is vertical (Fig. 8). If none of the principal stress axes is vertical, the axis with a higher plunge determines the stress regime. If two of the three principal stress axes have the same plunge value, the stress regime is uncertain. Finally, R refines the classification of the stress regime, such as pure, transtensional, transpressional or radial, shown in a stress symbol as arrows representing the horizontal projection of the principal stress axes (S_{Hmax} for maximum, S_{Hint} for intermediate and S_{hmin} for minimum; Fig. 8).

I performed further data separation and stress inversion using two different tools from Win_TENSOR (see Appendix B). In general, the user follows an iterative process of data selection and rejection that aims to group fractures by similar strike and individual principal stress axes. Each time, the software calculates the mean principal stress axes applying least-squares minimization. Finally, the user must generate a stable tensor solution in which fractures are compatible with the orientation of the mean principal stress axes and stress ratio. A stress symbol represents the horizontal principal stress axes and stress ratio.

2.3. Analysis

Uncertainty exists about the relative timing of fracturing and tilting of bedding in areas where faults with anomalous dip angles are present. The complexity increases with the number of tectonic events and the presence of oblique-slip faults. For this reason, the stress inversion in this study considers two possible scenarios. 'Scenario 1' assumes that faults formed after bedding tilting; thus, the input data are fractures in the present-day orientation. 'Scenario 2' assumes that fractures formed before bedding tilting, so the input data are the same fractures from Scenario 1 but rotated about a horizontal axis (see Appendix A). The correction consists of restoring the bedding plane to a horizontal position (e.g., Hippolyte et al., 2012). Because the orientation of bedding varies significantly between field sites and within a field site, the nearest bedding plane to a given fracture determines the magnitude and direction of horizontal-axis rotations.

Raw-data corrections do not include vertical-axes rotations because of a lack of suitable indicators, such as local paleomagnetic declination data. However, I consider the potential vertical-axis rotations of the most significant stress states by comparing them with strain states and possible displacement directions (see Figs. 28, 29).

3. RESULTS

Based on the subdivision of the complete data set by field site, the stress inversion yields 23 tensor solutions. The assumption for ‘Scenario 1’ solutions, yielding a total of 10 stress states for the four field sites, is that factures formed and/or were reactivated after tilting of bedding; thus, the stress inversion utilizes the present-day orientation of the fractures. The assumption for ‘Scenario 2’ solutions, yielding 12 stress states, is that fractures formed and/or were reactivated before tilting of bedding; therefore, the inversion utilizes bedding-corrected fracture orientations. For the remaining stress tensor solution, the strata are horizontal; hence, tilt corrections are unnecessary. The presentation order of the reduced stress states in each scenario does not imply a temporal sequence. These are simply the distinctive stress regimes derived from the stress inversion.

The second section of results describes the overprinting and cross-cutting relationships among multiple structural features. Given the grouping of such features into specific reduced stress tensors, these relationships are given in the relative order of stress states. Data from Blue Sac and Wasson Bluff contain some information on relative timing.

3.1.Economy Point (Figs. A1 to A3 in Appendix A)

The lithology in Economy Point consists of predominantly eolian medium-grained sandstones. They are classified as Wolfville Formation (Fig. 9; Olsen et al., 2000); however, their interpretation is ambiguous. For instance, seismic line EC-10 shows two tectonostratigraphic packages separated by an angular unconformity (Fig. 10). From bottom to top, they could be either the Honeycomb Point and Wolfville formations, or the Wolfville and “Lower” Blomidon formations.

A fault-propagation fold associated with a fault with reverse separation is present at depth, and deforms the angular unconformity and the beds above (Fig. 10). Other major faults near the study area, such as the E-striking Gerrish Mountain fault, also have reverse separation, are gently-dipping at depth, becoming steep near the surface (Fig. 10). The steep dip angle of the Gerrish Mountain fault produces a buttress fold, whereas the gently-dipping Cobequid fault acts as a detachment level (Fig. 10). The sampling area, consisting of three subsites in the western part of Economy Point, is near the trough of an E-W-trending large-scale syncline (Figs. 9, 10; Withjack et al., 2010). Therefore, strata are practically horizontal. Thus, the fracture data do not need a correction for bedding, and only one scenario applies to this field site.

A single stress state results from the data. Vertical and subvertical conjugate strike-slip faults and tension fractures striking in two preferred orientations yield stress state E-A, a pure strike-slip-faulting regime with the maximum horizontal principal stress

(S_{Hmax}) oriented NW-SE (Fig. 11; Table 1). Left-lateral strike-slip faults and tension fractures strike NNW and NNW-NW, respectively. Right-lateral strike-slip faults strike WNW to W.

3.2.Five Islands (Figs. A4, A5 in Appendix A)

Three units with no apparent growth beds are present in this study site. At Red Head, a NE-striking normal fault juxtaposes eolian sandstones and lacustrine shales of the "Lower" and "Upper" Blomidon Formation, respectively located in the footwall and hanging wall. The NMB overlies conformably the Blomidon Formation except at Old Wife Point, where the two units exhibit a fault contact (Fig. A4 in Appendix A). To the north, the same fault zone juxtaposes the NMB and the sandstones and mudstones facies of the McCoy Brook Formation.

Fracture data from Five Islands are from the southern limb of a large-scale syncline (Fig. 3). Thus, bedding in the central part of study area is N-dipping, with variations to the WNW east of Red Head. Near this site, large-scale faults strike to the NE and have normal slip, whereas others near the Red Head fault have anomalous dip angles. At Old Wife Point, however, a NE-striking left-lateral strike-slip fault zone (Withjack et al., 2010) approximately 100 m wide tilts originally vertical basaltic columns to a subhorizontal position.

3.2.1. Scenario 1 (Figs. 12, 13; Table 2; Fig. A6 in Appendix A)

The stress inversion of the data yields four stress states, assuming that fracture formation and/or reactivation occurred after tilting (Fig. 13). Stress state F1-A consists of

E-striking, conjugate and high-angle normal faults. It is a transtensional-faulting regime, with the minimum horizontal principal stress (S_{hmin}) oriented N-S, an intermediate horizontal principal stress (S_{Hint}) oriented to the E, and σ_1 plunging subvertically. Faults belonging to this stress state are located at and to the east of Red Head (Fig. 12).

Stress state F1-B is a transpressional-faulting regime with a N-trending S_{Hmax}, characterized by subvertical conjugate strike-slip faults striking N and ENE. High-angle left-lateral faults striking NNE and NE are also present in this solution. Conjugate strike-slip faults striking approximately NW and W define a stress state F1-C, a strike-slip-faulting regime with a WNW-trending S_{Hmax}. The intersection of these faults yields a subvertical σ_2. Stress state F1-D represents the large-scale normal-faulting regime at Red Head and the faults between that site and Old Wife Point (Fig. 12). σ_1 is subvertical in F1-D, and S_{hmin} strikes to the NW, perpendicularly to the strike of the faults.

3.2.2. Scenario 2 (Figs. 14, 15; Table 3; Fig. A7 in Appendix A)

Assuming that fractures formed and/or were reactivated before bedding tilting, the stress inversion produces a very minor change in stress state F2-A compared to scenario 1, with a nearly vertical σ_1 and a horizontal σ_3. The result is a transtensional-faulting regime, with S_{hmin} oriented N-S and an E-trending S_{Hint}. Faults in F2-B become slightly steeper, producing a slightly steeper σ_2 and shallower σ_1, and insignificant variation in the principal horizontal stress directions.

Stress state F2-C exhibits a significant change relative to F1-C. Correction for bedding of about 76º causes the present-day vertical conjugate strike-slip faults to become steeply-dipping conjugate oblique-slip faults with a major normal component.

The resulting stress regime is normal faulting with a NE-oriented S_{hmin}, located in the fault zone at Old Wife Point (Fig. 14).

The normal faults represented by F2-D, with a similar orientation to F1-D, consist of large-scale faults located in the Blomidon Formation (Fig. 14). All faults in this stress regime are moderately to steeply dipping and predominantly normal faults, suggesting a formation before bedding tilting.

3.3. Blue Sac (Figs. A8, A9 in Appendix A)

The lithology at Blue Sac consists of fluvial-lacustrine and talus-slope facies of the McCoy Brook Formation. Strata dip in multiple directions. In the northeast, beds are moderately dipping to the WNW. Moreover, mesoscale faulting is widespread, faults strike in multiple directions, and overprinting slickenlines are present. Near the Blue Sac fault, beds dip to the north at steeper dip angles. Near the Pinnacle, a SE-plunging overturned anticline is present (Withjack et al., 2010). In the southwest, strata are nearly horizontal. Elder Brady (2003) also reported anomalous orientations for bedding, faults, and slickenlines relative to an idealized rift basin, where beds dip towards the border fault and normal faults are perpendicular to the extension direction.

3.3.1. Scenario 1 (Figs. 16, 17; Table 4; Fig. A10 in Appendix A)

The stress inversion of the Blue Sac data yields three stress states, assuming that fracture formation and/or reactivation occurred after bedding tilting. Stress state B1-A is a normal-faulting regime with S_{hmin} oriented E-W. Faults in this subset are NW-striking, have a moderate dip angle, and exhibit normal slip and oblique slip with normal and right-lateral strike-slip components. Normal faults associated with B1-A are present to the east of the Pinnacle (Fig. 16).

Stress state B1-B is a transtensional-faulting regime with S_{Hmax} trending NNE. Only faults determine this solution, and they have two general orientations. One set consists of steeply-dipping, NE-to-E-striking, left-lateral strike-slip and oblique-slip faults with a predominant left-lateral component. The second set generally has NW-striking, right-lateral strike-slip faults with moderate to steep dip angles. Faults corresponding to stress state B1-B are present throughout the Blue Sac area irrespective of the degree of deformation of the rocks and the orientation of the major faults.

Conversely, two sets of faults represent the transpressional stress regime B1-C with S_{Hmax} trending NW, located at the two extremes of the study area (Fig. 16). A NNW-trending set is steeply dipping and exhibits left-lateral strike slip. The second set of faults contains subvertical, right-lateral strike-slip faults.

3.3.2. Scenario 2 (Figs. 18, 19; Table 5; Fig. A11 in Appendix A)

The stress inversion of the Blue Sac data yields four stress states, assuming that fracture formation and/or reactivation occurred before tilting. Stress state B2-A is a normal-faulting regime with a WNW-trending S_{hmin} and two sets of faults. One set has a moderate-to-steep dip angle and strikes from NW to N. Faults from this group exhibit mostly oblique slip with a predominant normal component. The second set is a group of WSW-striking normal faults. All faults in this regime are located at and east of the Pinnacle (Fig. 18).

Stress state B2-B consists of a pure strike-slip regime with S_{Hmax} oriented NNE-SSW. The correction for bedding tilting of most faults produced minor changes in the slickenline orientation relative to those on faults in B1-B. Solution B2-B also introduces mesoscale faults that were part of other stress regimes in Scenario 1.

Two stress states with fewer faults than the minimum required for the stress inversion were selected because their faults have similarities in strike, dip and slip sense. Stress state B2-C is a transpressional-faulting regime with a S_{Hmax} trending WNW. It contains a series of subvertical and steeply-dipping, left-lateral, strike-slip faults with strikes ranging from NNW to WNW. Moreover, one fault has two sets of slickenlines belonging to the same stress state (Fig. 19). B2-C appears at the two extremes of the study area, near the Portapique and Blue Sac faults.

Another stress state with few faults is B2-D, a normal-faulting regime with NE-trending S_{hmin} located east of the Pinnacle (Fig. 18). N-trending, steeply-dipping normal and oblique-slip with predominant normal component belong to this stress state.

3.3.3. Relative Timing

At Blue Sac, evidence of relative timing of events consists of overprinting slickenlines (Fig. 20A; Table 6). The relative order of stress states is B1-A followed by B1-B. In scenario 2, the order is B2-D followed by B2-A. No information on relative age is available for stress states B1-C and B2-B. Unlike other sites, at Blue Sac, up to three sets of overprinting slickenlines are present on the same fault plane (Fig. 20B; Tables A10, A11 in Appendix A), which has a dip direction and dip angle of 065º/43º in scenario 1, and 082º/74º in scenario 2. The oldest one consists of a thin layer of fibrous quartz ± zeolite covering the fault plane. The fibers are perpendicular to the strike of the fault and indicate pure dip slip. A younger set consists of grooves carved into the quartz layer filled with precipitates of quartz ± zeolite. The slickenlines suggest oblique slip with normal and left-lateral strike-slip components. The youngest set of slickenlines is composed by relatively thinner grooves oriented parallel to the strike of the fault and cutting across the second set. They indicate left-lateral strike-slip motion.

Two of the three sets of overprinting slickenlines belong to the same stress states in both scenarios (Table 6). Similarly, one set of slickenlines from stress state B2-C overprints another one of the same stress regime (Table 6) on a fault plane that has a dip direction and dip angle of 247º/65º. Those two sets do not show overprinting or cross-cutting relationships with fractures from other stress states, yielding an uncertain relative age. A possible explanation for overprinting slickenlines from the same stress state is that movement along the faults episodically induces rotations of the faults blocks. Consequently, each stage of motion produces a slightly different set of slickenlines.

3.4.Wasson Bluff (Figs. A12, A13 in Appendix A)

Wasson Bluff is the most complex site of the four study areas. In the northern part, the ENE-striking Portapique fault branches out in a fault system composed of segments that strike to the N, NE, ENE and E. As a result, bedding exhibits local variability. A general dip direction to the south reflects the geometry of the northern limb of a major syncline that trends parallel to the Portapique fault system and plunges to the ENE. The southern limb, located near Clarke Head, consists of strata dipping to the N and NE and a steeply dipping basaltic layer, locally overturned, bounded by a NE-striking fault with reverse separation and a major ENE-striking fault.

The structural complexity at Wasson Bluff also has implications for the stratigraphic and sedimentological architecture of this part of the basin. For instance, the Blomidon Formation exhibits a decrease in grain size and an increase in thickness toward the west, suggesting that the fault system was active during deposition (Olsen & Schlische, 1990). On the northern limb, the NMB shows pre-existing columnar jointing as well as layering generally dipping to the south at moderate angles. Near the faults, the cooling joints are filled with mudstone and sandstone (called sediment-filled fissures by Schlische & Ackermann, 1995), as well as silica ± zeolite veins (Kontak, 2008). The overlying unit, the McCoy Brook Formation, consists of eolian sandstones that locally exhibit matrix-supported, angular basaltic clasts near the faults. Those are part of the talus-slope facies and are indicators of activity of the adjacent faults during deposition (Olsen & Schlische, 1990).

3.4.1. Scenario 1 (Figs. 21, 22; Table 7; Fig. A14 in Appendix A)

Assuming that fractures post-date tilting of bedding, three reduced stress tensors result from the Wasson Bluff data. Stress state W1-A corresponds to a normal-faulting regime with S_{hmin} oriented WNW-ESE. The fractures from this group consist of faults, conjugate faults and a group of tension fractures that have a NNE strike. Slip on most faults ranges from normal to oblique with a major normal component. Nearly all fractures have a moderate dip angle. W1-A is present near major faults with N to ENE strikes, in both complex (center) and more simple (east) areas of the Portapique fault system (Fig.

21). Tension fractures are particularly common in the basalt, and they are pre-existing cooling joints that became reactivated and filled with red mudstone during extension (Fig. 6B).

Stress state W1-B corresponds to another normal-faulting regime with S_{hmin} oriented NNW-SSE. The stress state is composed exclusively of moderately-to-steeply dipping tension fractures in the basalt. The fractures, which are pre-existing cooling joints, are filled with silica ± zeolite and generally have a strike ranging from ESE to ENE. Less widespread than W1-A, W1-B is only present near major fault segments with N and NE strikes (Fig. 21). However, stress state W1-B commonly occurs at the same locations as W1-A.

Stress state W1-C is transpressional faulting regime with a NE-trending S_{Hmax}. Steeply-dipping right-lateral strike-slip faults strike N to NE, whereas left-lateral strike-slip faults with similar dip angles strike E to NE. W1-C is present in the central and western parts of the study area, especially near the ENE- and E-striking fault contacts between the NMB and the McCoy Brook Formation (Fig. 21). The WNW-striking reverse fault in the central part of the study area, which links to one of those faults, most likely is associated with W1-C as deformation compatible with a transpressional stress regime.

3.4.2. Scenario 2 (Figs. 23, 24; Table 8; Fig. A15 in Appendix A)

Assuming that fracture formation and/or reactivation occurred before bedding tilting, the data from Wasson Bluff yield four stress states. Stress state W2-A is a normal-faulting regime with S_{hmin} oriented NW-SE. It is defined by generally steeply-dipping normal faults and tension fractures that strike perpendicular to S_{hmin}. A small number of fractures are oblique-slip faults with a major normal component. Also, one low-angle oblique-slip fault striking NE-SW is compatible with this solution. In this scenario, W2-A is the predominant stress state in the study area, and is characteristic of sites near major faults with N to ENE strikes (Fig. 23).

Corrections for bedding of tension fractures in W1-B produce steeper structures with an E-W to NNE strike, as shown in stress state W2-B (Fig. 24). This normal-faulting regime differs from W1-B in terms of orientation of principal stress axes, where σ_1 becomes steeper and σ_3 becomes more horizontal. However, S_{Hmax} invariably trends to the NNW.

Stress state W2-C contains tension fractures and oblique-slip faults with a predominant normal component, all of them striking from the NNW to the NE. The result is a normal-faulting regime with S_{hmin} trending approximately E-W. The tension fractures are present only in the columnar basalt, whereas faults are present in the NE part of the study area (Fig. 23).

Stress state W2-D represents a transpressional-faulting regime with S_{Hmax} oriented NE-SW. The majority of faults are steeply-dipping to vertical strike-slip conjugate faults striking N and ENE, with S_{Hmax} bisecting the acute angle between them. Similar to W1-C, W2-D is present in areas near the ENE- and E-striking faults juxtaposing the NMB and the McCoy Brook Formation (Fig. 23).

3.4.3. Relative Timing

At Wasson Bluff, cross-cutting relationships of tension fractures are indicators of the relative timing of deformational events (Table 9). In one group, a tension fracture filled with red mudstone exhibits slickenlines on the plane of the filler material. Another group involves two sets of tension fractures filled with red mudstone and silica ± zeolite, respectively (Fig. 25); the silica ± zeolite veins cut across the sediment-filled fractures.

The relative age at Wasson Bluff is well constrained only for the normal-faulting regime in scenario 1, in which relationships show that W1-A precedes W1-B. In scenario 2, the data suggest that W2-A and W2-C preceded W2-B, but at the same time W2-B preceded W2-C. Two possible alternatives may account for this contradiction in the data. One is that W2-A and W2-C belong to the same tectonic phase and are older than W2-B. The second alternative is that W2-A, W2-B and W2-C are all part of one tectonic phase. In this case, the differences in the S_{hmin} orientations would be an artifact of the tension fractures in pre-existing cooling joints that become reactivated during a normal faulting phase.

4. INTERPRETATION AND DISCUSSION

In general, the stress states from the four field sites group into normal-faulting and strike-slip faulting regimes (Fig. 26). Normal-faulting regimes are the dominant category assuming that fractures formed before tilting of bedding (Scenario 2). However, the largest group in the case of formation after tilting of bedding (Scenario 1) is fractures belonging to strike-slip, transpressional and transtensional faulting regimes. A regional pattern of two stress states, one from each scenario, suggests that fractures formed in at least two distinct tectonic events. Based on overprinting and geologic evidence, the older event consists of normal faulting with S_{hmin} generally oriented NW-SE, whereas the younger event is a strike-slip faulting regime with S_{Hmax} trending N-S to NE-SW (Fig. 27).

4.1.Relationships Among Stress, Strain and Displacement Directions

In this section, I infer the displacement direction of the hanging wall during the two tectonic events using the relationships of Withjack & Jemison (1986) and the extension and shortening directions derived from the stress states. Regional patterns of stress states reflect the movement of the hanging wall relative to the footwall along the Cobequid-Chedabucto border-fault zone. Under conditions of infinitesimal strain, the principal stress and strain directions are coaxial (Withjack & Jamison, 1986). Therefore, the orientation of S_{hmin} is equivalent to the extension direction and the orientation of S_{Hmax} is equivalent to the shortening direction.

A correlation exists between strain state and displacement direction (e.g., Withjack & Jamison, 1986; Fig. 28). During rifting, the extension direction lies midway between the normal to the deformation zone (or preexisting zone of weakness) and the displacement direction, forming the angle γ (Fig. 28). Normal faults form when the angle between the deformation zone and displacement direction (i.e., α) is $30^{o}<\alpha\leq90^{o}$. Consequently, the associated extension direction lies between $60^{o}<\gamma\leq90^{o}$, and the shortening direction is vertical. Similarly, during shearing and oblique convergence, the shortening direction lies midway between the normal to the deformation zone (or preexisting zone of weakness) and the displacement direction, forming the angle β (Fig.

29). In this strain state, strike-slip faults form when $0° \leq \alpha < 30°$ (Fig. 29). Thus, the shortening direction lies in the range of $45° < \beta < 60°$. The sense of slip (i.e., left-lateral or right-lateral strike slip) depends on the strain state (Fig. 29).

4.2. Tectonic Event #1: Rifting

According to previous studies, the extension direction during rifting was NW-SE (Olsen & Schlische, 1990; Schlische & Ackermann, 1995; Withjack et al., 2009). Evidence of normal faulting associated with rifting is present at Five Islands, Blue Sac and Wasson Bluff. The valid stress states, which belong to Five Islands and one to Wasson Bluff (i.e., F1-D, W1-B and W2-B), yield an extension direction consistent with a hanging-wall displacement ranging from SSE to SE, and possibly reaching more easterly-oriented directions (Figs. 30, 31). Conversely, the extension directions derived from the predominant stress states at Blue Sac and three from Wasson Bluff (i.e., B1-A, W1-A, B2-A, W2-A and W2-C) fall outside of the range of possible extension directions associated with the major E- to ENE-striking faults (Figs. 30, 31). Therefore, the extension directions from those four stress states are invalid for conditions of infinitesimal strain, regardless the timing of formation relative to tilting of bedding.

To be valid, the extension directions from Blue Sac and Wasson Bluff must be rotated no more than approximately 40º counterclockwise relative to the range of possible extension directions. A counterclockwise vertical-axis rotation of fractures that formed during rifting is possible if left-lateral strike slip occurred on the major faults possibly during and/or after tilting of bedding. In fact, the evidence from both sites supports the presence of a postrift strike-slip-faulting regime with a shortening direction in the NE quadrant (Fig. 27), which is compatible with left-lateral strike slip on the major faults. At Wasson Bluff, however, the different extension directions (i.e., W1-A/W2-A and W1-B/W2-B/W2-C; Figs. 22, 24) are also the result of the opening of columnar joints in the basalt during extension and not necessarily because of subsequent vertical-axis rotations. Nonetheless, the widest fissures indicate NW-SE extension (Schlische & Ackermann, 1995).

Elder Brady (2003) proposed that dip-slip faults and bedding at Blue Sac rotated counterclockwise about a vertical axis after their formation. She noted that the present-day orientations of dip-slip faults indicate an ENE-WSW-extension direction, in contrast to the direction suggested by field evidence. The dip direction of bedding is also anomalous. Instead of dipping toward the border fault (i.e., NNW), beds dip to the west. Thus, a counterclockwise vertical-axis rotation from a more reasonable extension direction and an idealized dip direction of bedding is plausible. Similarly, the rotation is compatible with postrift left-lateral strike slip on the Portapique and Blue Sac faults (Elder Brady, 2003; Baum, 2006; Withjack et al., 2010).

The average ENE strike of the Shelburne dike suggests NNW-SSE extension direction, equivalent to a SSE displacement of the southern block (Fig. 32). The dikes surrounding the Fundy basin, which have a similar strike (Fig. 2), also yield a comparable extension and displacement directions. A SSE displacement direction is only similar to that at Five Islands, suggesting that vertical-axis rotations near the Red Head fault are minimal. At the same time, a disagreement between extension directions inferred for Five Islands and the Shelburne dike versus the stress states for Blue Sac and partially for

Wasson Bluff reinforces the hypothesis of the presence of vertical-axis rotations at Blue Sac and Wasson Bluff.

4.2.1. Absolute Timing Constraints

The rifting stage with an average SE displacement of the hanging wall (Fig. 33) is the best-constrained episode of the deformational history of the Fundy basin. Growth strata thickening towards the border fault (Withjack et al., 1995, 2010, 2012a) suggest an age of rifting ranging from Permian (if the Honeycomb Point Formation is, in fact, synrift) or Middle Triassic (Anisian) to Early Jurassic (Sinemurian) in the Fundy basin (Fig. 2). Cyclostratigraphic, biostratigraphic and radiometric age controls are available for these rocks (Olsen et al., 1987; Olsen et al., 1997; Whiteside et al., 2007; Jourdan et al., 2009; Schoene et al., 2010; Blackburn et al., 2013). The sediment-filled tension fractures have very tight chronological constraints; they formed between the cooling of the basalt and the deposition of the basal McCoy Brook Formation in the latest Late Triassic (Schlische & Ackermann, 1995; Lucas et al., 2011).

4.3. Tectonic Event # 2: Basin Inversion

Evidence from Five Islands, Blue Sac and Wasson Bluff indicates that postrift, NE-directed displacement produced strike-slip faulting along the northern margin of the Minas subbasin. Assuming that fractures formed after tilting of bedding, all the dominant stress states at those sites (i.e., F1-B, B1-B and W1-C) yield a shortening direction compatible with a hanging-wall displacement ranging from NNE to NE and possibly to the ENE (Fig. 34). A similar displacement direction results from the assumption that fractures formed before tilting of bedding (i.e., F2-B, B2-B and W2-D; Fig. 35). If a general NE displacement is valid, it would produce at least a component of left-lateral strike slip on the border-fault zone. Consequently, counterclockwise vertical-axis rotations likely occurred on mesoscale fractures that formed before or during this tectonic event. An example of rotated preexisting structures is the set of fractures yielding invalid extension directions from the first event (rifting). These stress/strain states exhibit counterclockwise vertical-axis rotations relative to the idealized orientations. Faults formed during the second event, such as the ones located at Five Islands, most likely rotated about a vertical axis in a counterclockwise sense due to left-lateral shear produced in the Old Wife fault zone (Withjack et al., 2010) or by the overall ENE-striking border-fault zone.

4.3.1. Strain Partitioning

Strain partitioning is the separation of oblique shortening into discrete zones of strike-slip faulting, dip-slip faulting and folding (e.g., Nicol & van Dissen, 2002; Withjack et al., 2010). The shortening direction associated with a general NE displacement of the hanging wall is compatible with the left-lateral strike slip on the border-fault zone and the trend of only some folds. This suggests that faulting and folding developed at two different tectonic events, or they are coeval and strain is partitioned (Fig. 35). My inferred displacement direction during the phase of basin inversion only reflects the movement along the border-fault zone; thus, it supports the idea of separate tectonic phases. If strain partitioning occurred, then the average NE displacement along the border-fault zone accommodates the left-lateral strike-slip component, whereas folding (trending from NE to ENE) accommodates the NE-to-WNW-directed shortening component. The net result of the strain partitioning would be a mean NE displacement direction of the hanging wall (Fig. 36), which is similar to the direction proposed by Withjack et al. (2010).

4.3.2. Comparison of Postrift Deformation with Previous Studies

Previous studies have explained that many structures at Blue Sac and Wasson Bluff formed during a postrift stage of NE-directed displacement. For instance, Baum (2006) explained that a series of oblique-slip faults, NW-trending synclines and anticlines, NNW- and NE-striking conjugate strike-slip faults and an E-W-striking reverse fault at Blue Sac are the result of a NE displacement of the hanging wall. Elder Brady (2003) concluded a similar displacement direction based on neoformed strike-slip faults and reactivated normal faults as strike-slip faults. At Wasson Bluff, anomalously dipping faults, oblique-slip and strike-slip faults are among the structures that are compatible with postrift NE-directed movement of the hanging wall (Withjack et al., 1995; Elder Brady, 2003; Withjack et al., 2010).

At a regional scale, multiple studies have yielded shortening directions comparable to those obtained in this study for the postrift deformation. In the Newark basin, postrift deformation, such as folds adjacent to the border-fault zone (some with very steep limb dips) (Withjack & Schlische, 2005), calcite twinning (Lomando & Engelder, 1984) and axial-planar cleavage (Lucas et al., 1988), suggests a N-S to NE-SW shortening direction. In the Hartford basin, De Boer & Clifton (1988) proposed two postrift stages based on fault data and crosscutting relationships. The first stage consists of NE shortening related to the “shifting” phase from rifting to drifting. De Boer (1992) also determined a similar shortening direction in the Fundy basin. The second phase is NW shortening, which De Boer & Clifton (1988) related to the drifting stage.

Seismic data from the offshore Orpheus, Scotian and Emerald/Naskapi basins (Withjack et al., 1995; Durcanin, 2009; Syamsir, 2010; Etikha, 2012; Hanafi, 2013), with a more complete synrift and postrift stratigraphic section than the Fundy basin, show a number of faults with reverse separation, buckle folds, and shortened synrift salt structures (Fig. 37). Although some of this evidence might be associated with postrift deformation, it does not provide information on strain states.

4.3.3. Absolute Timing Constraints

Although the age of rifting is reasonably well constrained, the absence of postrift strata has led to a debate on the absolute timing of the postrift event in the Fundy basin (Withjack et al., 2012b). However, the seismic data from the offshore Orpheus, Scotian and Emerald/Naskapi basins (Withjack et al., 1995; Durcanin, 2009; Syamsir, 2010; Etikha, 2012; Hanafi, 2013) provide insight on the timing of the basin inversion event. Three major unconformities, associated with postrift faulting, folding, regional uplift and erosion, indicate that several significant tectonic events affected parts of the eastern North American margin after rifting (Figs. 37, 38). The breakup unconformity marks the transition from rifting to drifting in the Sinemurian/Pliensbachian (Early Jurassic). The Avalon unconformity developed in the Early Cretaceous (Etikha, 2012; Hanafi, 2013), and may be related to compressional pulses associated with ridge push and/or basal drag of the continental lithosphere during the initiation of seafloor spreading (Withjack et al., 1995; Withjack et al., 1998; Withjack et al., 2012b). The third unconformity developed during late Oligocene to Miocene time (MacLean & Wade, 1992; Etikha, 2012). In the Scotian basin, the unconformity is an erosional surface that forms deeply incised canyons and separates faulted and folded Paleocene-Oligocene strata and undeformed Pliocene-Pleistocene units (Fig. 37; Durcanin, 2009; Syamsir, 2010; Etikha, 2012; Hanafi, 2013).

Uplift occurred in the Newark and Taylorsville basins, with 2-6 km and up to 3 km of postrift erosion, respectively (Malinconico, 1999, 2003). The timing of this deformation is unknown. Gallen et al. (2013), conversely, reported uplift since the Miocene in the Cullasaja River basin in North Carolina. Finally, stress data from earthquake focal mechanisms indicate that a NE-oriented S_{Hmax}, thus a NE-trending shortening (assuming coaxial deformation), is the current stress state in central and eastern United States and southeastern Canada (Hurd & Zoback, 2012). The focal mechanism solution of the M_s 7.2 Grand Banks earthquake (Bent, 1995), as well as the orientation of the possible seismic source (Etikha, 2012), are compatible with this stress state. Because the plate-tectonic setting has not changed since breakup, the NE-shortening direction possibly has been the same one operating in the central segment of the eastern North America margin since then (Fig 38), producing mostly strike slip along the border fault of the Minas subbasin.

4.4. Stress States of Unknown Origin

Many stress regimes obtained from the stress inversion of fracture data do not fit in the rifting or the postrift deformation with NE-directed displacement scenarios (e.g., E-A, F1-A, F1-C, F2-A, F2-C, B1-C, B2-C and B2-D). The origin of those stress states is unknown. More evidence is necessary to determine whether they are the result of actual geologic processes or unrealistic stress inversion products.

4.5. Limitations of the Approach

The stress inversion method involves a series of uncertainties that limit the significance of the findings in my study. First, the stress inversion method does not resolve time constraints. At most, cross-cutting relationships and overprinting slickenlines provide a relative order of events, which can change depending on the inferred stress states.

The inferred stress states are sensitive to the quality of the input data. Thus, the fracture data must be reliable and tied closely to the geology of the area. Uncertainty increases in the stages of data separation and inversion, especially because the software works with numerical algorithms and does not involve geologic criteria. Although the data require a preliminary separation based on field criteria, subsequent stages of separation can produce multiple possible reduced stress tensors. This number increases with the structural complexity and number of tectonic events.

Vertical-axis rotations are another limitation of the approach. A lack of indicators for vertical-axis rotations, such as local paleomagnetic declination data, restricts the inversion of fractures to the use of present-day orientations or corrected orientations for tilting of bedding. This issue has special significance in areas where the evidence indicates the presence of strike slip. Consequently, the processing of strike-slip faults might result in biased stress states.

Strain partitioning also limits the approach, which only involves fractures. Therefore, the stress states, extension directions and displacement directions only reflect the brittle behavior along the border-fault zone. This is problematic in the Fundy basin, where folding is also present and strain partitioning likely occurred (Withjack et al., 2010).

5. CONCLUSIONS

Faults, conjugate faults and tension fractures from the eastern part of Fundy rift basin provide information on the stress states produced by multiple stages of deformation. The fracture data, processed through stress inversion, yield reduced stress tensors that are partially compatible with the local geology. The major cause of discrepancies is the rotation of fractures by tilting of bedding and strike slip, which bias the resulting orientation of some of the stress states. The analysis through horizontal-axis corrections show little difference from those derived from unrotated fractures within the same site. Furthermore, I inferred counterclockwise vertical-axis rotations of stress states mostly due to a left-lateral strike-slip component on the border-fault zone.

Two tectonic events describe most of the formation and/or reactivation of structures from the northern shore of the Minas subbasin. One of them belongs to postrift deformation. Tentatively, I propose the following order of events:

1) Rifting characterized by a normal faulting and produced by an average SE displacement of the hanging wall during Late Triassic/Early Jurassic.
2) Basin inversion characterized by a strike-slip faulting and produced by left-lateral shear along the border-fault zone. The average movement of the

hanging wall is NE regardless faulting and folding are or not coeval. Its absolute age is unclear.

The presence of multiple stages of deformation, the quality of the input data and processing, vertical-axis rotations and strain partitioning are among the factors that limit the approach used in this study.

5.1.Future Work

- Collect and analyze additional fracture data from the northern shore of the Minas Basin to confirm or reject the postrift westward shear of the hanging wall.
- Collect and analyze fracture data from the southern shore of the Minas subbasin to confirm if the postrift stress states obtained in this study are widespread or just localized along the border-fault system.
- Collect and analyze fracture data from onshore Cretaceous units near Middle Musquodoboit, Nova Scotia (Keppie, 2000), to have a better control of timing of deformation.

REFERENCES

Anderson, E.M. (1951). The dynamics of faulting and dyke formation (2nd Edition). Oliver & Boyd, Edinburgh.

Angelier, J. (1984). Tectonic analysis of fault slip data sets. *Journal of Geophysical Research*, 89, (B7), 5835-5848.

Baum, M.S. (2002). *3-D geometry of inversion structures in the Mesozoic Fundy rift basin* (M.S. Thesis). Rutgers University, New Jersey.

Baum, M.S. (2006). *Controls on the deformation produced by oblique inversion of rift basins: which structures reflect the paleostrain state?* (Doctoral thesis). Rutgers University, New Jersey.

Baum, M. S., Withjack, M. O. & Schlische, R. W. (2008). The ins and outs of buttress folds: Examples from the Fundy rift basin, Nova Scotia, Canada. In Brown, D. E. (Ed.), *Central Atlantic Conjugate Margins, Program and Extended Abstracts*. Dalhousie University, Halifax, Nova Scotia, 53-61 p.

Bent, A. L. (1995). A complex double-couple source mechanism for the M_s 7.2 1929 Grand Banks earthquake. *Bulletin of the Seismological Society of America*, 85 (4), 1003-1020.

Blackburn, T. J., Olsen, P. E., Bowring, S. A., McLean, N. M., Kent, D. V., Puffer, J., McHone, G., Rasbury, E. T. & Et-Touhami, M. (2013). Zircon U-Pb geochronology links the end-Triassic extinction with the Central Atlantic Magmatic Province. *Science*, doi:10.1126/science.1234204.

Cobbold, P. R., Chiossi, D., Green, P. F., Japsen, P. & Bonow, J. (2010). Compressional reactivation, Atlantic margin of Brazil: Structural styles and consequences for hydrocarbon exploration. *Search and Discovery*, 2010: 30114.

de Boer, J. Z. (1992). Stress configurations during and following emplacement ENA basalts in the northern Appalachians. In Puffer, J. H. & Ragland, P. C. (Eds.), *Eastern North American Mesozoic magmatism*. Geological Society of America Special Paper, 268, 361-378.

de Boer, J. Z. & Clifton, A. E. (1988). Mesozoic tectonogenesis: Development and deformation of 'Newark' rift zones in the Appalachians (with special emphasis on the Hartford basin, Connecticut). In Manspeizer, W. (Ed.), *Triassic-Jurassic rifting: Continental breakup and the origin of the Atlantic Ocean and passive margins*. Elsevier, New York, 275-306.

Delvaux, D. & Sperner, B. (2003). New aspects of tectonic stress inversion with reference to the TENSOR program. In D. A. Nieuwland (Ed.), *New Insights into*

Structural Interpretation and Modeling. Geological Society, London, Special Publications, 212, 75-100.

Delvaux, D., Moeys, R., Stapel, G., Melnikov, A., & Ermikov, V. (1995). Paleostress reconstructions and geodynamics of the Baikal region, Central Asia, Part 1: Paleozoic and Mesozoic pre-rift evolution. *Tectonophysics*, 252, 61-101.

Delvaux, D., Moeys, R., Stapel, G., Petit, C., Levi, K., Miroshnichenko, A., Ruzhich, V., & San'kov, V. (1997). Paleostress reconstructions and geodynamics of the Baikal region, Central Asia, Part 2: Cenozoic rifting. *Tectonophysics*, 282, 1-38.

Doblas, M. (1998). Slickenside kinematic indicators. *Tectonophysics*, 295, 187-197.

Donohoe, H.V. & Wallace, P.I. (1982). Geological map of the Cobequid Highlands: Colchester, Cumberland & Pictou Counties, Nova Scotia [map]. 1:50,000. Map 82-7. Halifax, Nova Scotia: Nova Scotia Department of Mines and Energy.

Dunn, A. M., Reynolds, P. H., Clarke, D. B. & Ugidos, J. M. (1998). A comparison of the age and composition of the Shelburne dyke, Nova Scotia, and the Mesejana dyke, Spain. *Canadian Journal of Earth Sciences*, 35, 1110-1115.

Durcanin, M. A. (2009). *Influence of synrift salt on rift-basin development: Application to the Orpheus basin, offshore eastern Canada* (M.S. Thesis). Rutgers University, New Jersey. 152 p.

Elder Brady, J. A. (2003). *Effectiveness on small-scale structures in deciphering the tectonic history of the Mesozoic Fundy rift basin* (M.S. Thesis). Rutgers University, New Jersey.

Etikha. (2012). *Postrift deformation of the Scotian basin, offshore Nova Scotia and Newfoundland, Canada: Insights from 2D and 3D seismic-reflection data* (M.S. Thesis). Rutgers University, New Jersey.

Fisher, B.E., Poole, J.C., & McKinnon, J.S. (2006). Shaded relief images derived from a 25 metre digital elevation model of the province of Nova Scotia, DP ME 56, Version 2, [DEM]. Halifax, Nova Scotia: Nova Scotia Department of Natural Resources, Mineral Resources Branch.

Gallen, S. F., Wegmann, K. W., & Bohnenstiehl, D. R. (2013). Miocene rejuvenation of topographic relief in the southern Appalachians. *GSA Today*, 23 (2), 4-10.

Hamblin, A. P. (2001). Stratigraphy, sedimentology, tectonics, and resource potential of the Lower Carboniferous Mabou Group, Nova Scotia. Geological Survey of Canada, Bulletin 568, 164 p.

Hanafi, B. R. (2013). *The influence of basin architecture and synrift salt on structural evolution during and after rifting: A case study of the Orpheus rift basin, offshore Nova Scotia and Newfoundland, Canada* (M.S. Thesis). Rutgers University, New Jersey.

Hancock, P. L. (1985). Brittle microtectonics: principles and practice. *Journal of Structural Geology*, 7 (3), 437-457.

Hippolyte, J. C., Bergerat, F., Gordon, M. B., Bellier, O., & Espurt, N. (2012). Keys and pitfalls in mesoscale fault analysis and paleostress reconstructions, the use of Angelier's methods. *Tectonophysics*, doi:10.1016/j.tecto.2012.01.012.

Hubert, J. F. & Mertz, K. A. (1984). Eolian sandstones in Upper Triassic-Lower Jurassic red beds of the Fundy Basin, Nova Scotia. *Journal of Sedimentary Petrology*, 54, 798-810.

Hurd, O. & Zoback, M. D. (2012). Intraplate earthquakes, regional stress and fault mechanics in the Central and Eastern U.S. and Southeastern Canada. *Tectonophysics*, 581, 182-192.

Jourdan, F., Marzoli, A., Bertrand, H., Cirilli, S., Tanner, L. H., Kontak, D. J., McHone, G., Renne, P. R., & Bellieni, G. (2009). ^{40}Ar/^{39}Ar ages of CAMP in North America: Implications for the Triassic-Jurassic boundary and the ^{40}K decay constant bias. *Lithos*, 110, 167-180.

Keppie, J. D. (compiler) (2000). Geological map of the province of Nova Scotia [map]. 1:500,000. Map ME 2000-1. Halifax, Nova Scotia: Nova Scotia Department of Natural Resources, Minerals and Energy Branch.

Kipata, M.L., Delvaux, D., Sebagenzi, M.N., Cailteux, J., & Sintubin, M. (2012). Brittle tectonic and stress field evolution in the Pan-African Lufilian arc and its foreland (Katanga, DRC): from orogenic compression to extensional collapse, transpressional inversion and transition to rifting. *Geologica Belgica*, 16 (1-2), 1-17.

Kontak, D. J. (2008). On the edge of CAMP: Geology and volcanology of the Jurassic North Mountain Basalt, Nova Scotia. *Lithos*, 101, 74-101.

Leleu, S. & Hartley, A. J. (2010). Controls on the stratigraphic development of the Triassic Fundy Basin, Nova Scotia: implications for the tectonostratigraphic evolution of Triassic Atlantic rift basins. *Journal of the Geological Society of London*, 167, 437-454.

Lomando, A. J. & Engelder, T. (1984). Strain indicated by calcite twinning: Implications for deformation of the early Mesozoic northern Newark basin, New York. *Northeastern Geology*, 6, 192-195.

Louden, K. (2002). Tectonic evolution of the east coast of Canada. *CSEG Recorder*, 27 (2), 37-48.

Lucas, M., Jull, J. & Manspeizer, W. (1988). A foreland-type fold and related structures in the Newark rift basin. In Manspeizer, W. (Ed.), *Triassic-Jurassic rifting, continental breakup and the origin of the Atlantic Ocean passive margins, part A*. New York, Elsevier, 307-332 p.

Lucas, S. G., Tanner, L. H., Donohoo-Hurley, L. L., Geissman, J. W., Kozur, H. W., Heckert, A. B. & Weems, R. E. (2011). Position of the Triassic-Jurassic boundary and timing of the end-Triassic extinctions on land: Data from the Moenave Formation on the southern Colorado Plateau, USA. *Palaeogeography, Palaeoclimatology, Palaeoecology*, doi:10.1016/j.palaeo.2011.01.009.

Lundin, E. R., Doré, A. G., Røning, K. & Kyrkjebø, R. (2013). Repeated inversion and collapse in the Late Cretaceous-Cenozoic northern Vøring Basin, offshore Norway. *Petroleum Geoscience*, doi:10.1144/petgeo.2012-022.

MacLean, B. C. & Wade, J. A. (1992). Petroleum geology of the continental margin south of the islands of St. Pierre and Miquelon, offshore eastern Canada. *Bulletin of Canadian Petroleum Geology*, 40, 222-253.

Malinconico, M.L. (1999). Thermal history of the Early Mesozoic Newark (NJ/PA) and Taylorsville (VA) basins using borehole vitrinite reflectance: conductive and advective effects. *Geological Society of America*, Abstracts with Programs 31, A–31.

Malinconico, M.L. (2003). Paleo-maximum thermal structure of the Triassic Taylorsville (Virginia) basin: evidence for border fault convection and implications for duration of syn-rift sedimentation and long-term elevated heat flow. In LeTourneau, P. M. & Olsen, P. E. (Eds.), *Aspects of Triassic-Jurassic Rift Basin Geoscience*. State Geological and Natural History Survey of Connecticut Miscellaneous Reports, 1, 25–26.

McHone, J. G. (2003). Fissure dike source(s) for the North Mountain Basalt Group. *Geological Society of America's 38th Annual Meeting, Northeast Section*, Paper No. 37-6.

Murphy, J. B., Waldron, J. W., Kontak, D. J., Pe-Piper, G., & Piper, D. J. (2011). Minas Fault Zone: Late Paleozoic history of an intra-continental orogenic transform fault in the Canadian Appalachians. *Journal of Structural Geology*, 33, 312-328.

Nicol, A. & van Dissen, R. (2002). Up-dip partitioning of displacement components on the oblique-slip Clarence fault, New Zealand. *Journal of Structural Geology*, 24, 1521-1535.

Olsen, P. E. (1997). Stratigraphic record of the early Mesozoic breakup of Pangea in the Laurasia-Gondwana rift system. *Annual Review of Earth and Planetary Sciences*, 25, 337-401.

Olsen, P. E., Kent, D. V., Fowell, S. J., Schlische, R. W., Withjack, M. O., & LeTourneau, P. M. (2000). Implications of a comparison of the stratigraphy and depositional environments of the Argana (Morocco) and Fundy (Nova Scotia, Canada) Permian-Jurassic basins. In Oujidi, M & Et-Touhami, M. (Eds.), *Le Permien et le Trias du Maroc: Actes de la Première Réunion du Groupe Marocain du Permien et du Trias*. Ouijda, Hilal Impression, 165-183.

Olsen, P. E. & Schlische, R. W. (1990). Transtensional arm of the early Mesozoic Fundy rift basin: Penecontemporaneous faulting and sedimentation. *Geology*, 18, 695-698.

Olsen, P. E., Schlische, R. W. & Gore P. J. W. (1989). *Field Guide to the Tectonics, Stratigraphy, Sedimentology, and Paleontology of the Newark Supergroup, Eastern North America.* International Geological Congress, Guidebooks for Field Trips T351.Washington, DC: American Geophysical Union, 174 p.

Olsen, P. E., Shubin, N. H. & Anders, M. H. (1987). New Early Jurassic tetrapod assemblages constrain Triassic-Jurassic tetrapod extinction event. *Science*, 237, 1025-1029.

Pe-Piper, G., Jansa, L. F., & Lambert, R. S. J. (1997). Early Mesozoic magmatism on the eastern Canadian margin: Petrogenetic and tectonic significance. In Puffer, J. H. & Ragland, P. C. (Eds.), *Eastern North American Mesozoic magmatism*. Geological Society of America Special Paper, 268, 13-36.

Petit, J. P. (1987). Criteria for the sense of movement on fault surfaces in brittle rocks. *Journal of Structural Geology*, 9 (5-6), 597-608.

Ryan, R. J. & Boehner, R. C. (1994). Geology of the Cumberland Basin, Cumberland, Colchester and Pictou Counties, Nova Scotia. Nova Scotia Department of Natural Resources, Memoir 10, Halifax, 222 p.

Schlische, R. W. (2003). Progress in understanding the structural geology, basin evolution, and tectonic history of the Eastern North American Rift System. In LeTourneau, P. M. & Olsen, P. E. (Eds), *The Great Rift Valleys of Pangea in Eastern North America: Tectonics, structure , and volcanism*. Columbia University Press, 1, 21-64.

Schlische, R. W. & Ackermann, R. V. (1995). Kinematic significance of sediment-filled fissures in the North Mountain Basalt, Fundy rift basin, Nova Scotia, Canada. *Journal of Structural Geology*, 17 (7), 987-996.

Schlische, R. W., Withjack, M. O., & Olsen, P. E. (2003). Relative timing of CAMP, rifting, continental breakup, and basin inversion: Tectonic significance. In Hames, W. E., McHone, G. C., Renne, P. R., & Ruppel, C. R. (Eds), *The Central Atlantic Magmatic Province: Insights from fragments of Pangea*. American Geophysical Union Monograph, 136, 33-59.

Schoene, B., Guex, J., Bartolini, A., Schaltegger, U., Blackburn, T. J. (2010). Correlating the end-Triassic mass extinction and flood basalt volcanism at the 100 ka level. *Geology*, 38 (5), 387-390.

Sinclair, I. K. (1995). Transpressional inversion due to episodic rotation of extensional stresses in Jeanne d'Arc basin, offshore Newfoundland. In Buchanan, J.G. & Buchanan, P.G. (Eds.), *Basin Inversion*, Geological Society Special Publication, 88, 249–271.

Sperner, B., Ratschbacher, L., & Ott, R. (1993). Fault-striae analysis: a turbo pascal program package for graphical presentation and reduced stress tensor calculation. *Computers and Geosciences*, 19, 1361-1388.

Stea, R. R. & Wightman, D. M. (1987). Age of the Five Islands Formation, Nova Scotia, and the deglaciation of the Bay of Fundy. *Quaternary Research*, 27 (3), 211-219.

Syamsir, Z. (2010). *The Mesozoic Orpheus rift basin, offshore Nova Scotia and Newfoundland, Canada: Synrift and early postrift evolution of a well-imaged North Atlantic rift basin* (M.S. Thesis). Rutgers University, New Jersey, 142 p.

Tanner, L. H. (1995). Formal definition of the Lower Jurassic McCoy Brook Formation, Fundy rift Basin, eastern Canada. *Atlantic Geology*, 32, 127-135.

Tanner, L. H. & Hubert, J. F. (1991). Basalt breccias and conglomerates of the Lower Jurassic McCoy Brook Formation, Fundy basin, Nova Scotia: differentiation of talus and debris-flow deposits. *Journal of Sedimentary Petrology*, 61, 15-27.

Wade, J. A., Brown, D. E., Traverse, A., & Fensome, R. A. (1996). The Triassic-Jurassic Fundy Basin, eastern Canada: Regional setting, stratigraphy and hydrocarbon potential. *Atlantic Geology*, 32, 189-231.

Weston, J. F., MacRae, A., Ascoli, P., Cooper, M. K., Fensome, R. A., Shaw, D., & Williams, G. L. (2012). A revised biostratigraphic and well-log sequence-stratigraphic framework for the Scotian Margin, offshore eastern Canada. *Canadian Journal of Earth Sciences*, 49, 1417-1462.

Whiteside, J. H., Olsen, P. O., Kent, D. V., Fowell, S. J. & Et-Touhami, M. (2007). Synchrony between the Central Atlantic Magmatic Province and the Triassic-Jurassic mass-extinction event? *Palaeogeography, Palaeoclimatology, Palaeoecology*, 244, 345-367.

Withjack, M. O., Baum, M. S., & Schlische, R. W. (2010). Influence of preexisting fault fabric on inversion-related deformation: A case study of the inverted Fundy rift basin, southeastern Canada. *Tectonics*, doi:10.1029/2010TC002744.

Withjack, M. O. & Jamison, W. R. (1986). Deformation produced by oblique rifting. *Tectonophysics*, 126, 99-124.

Withjack, M. O., Olsen, P. E., & Schlische, R. W. (1995). Tectonic evolution of the Fundy rift basin, Canada: Evidence of the extension and shortening during passive margin development. *Tectonics*, 14 (2), 390-405.

Withjack, M. O. & Schlische, R. W. (2005). A review of tectonic events on the passive margin of Eastern North America. In Post, P. (Ed.), *Petroleum Systems of Divergent Continental Margin Basins*. 25th Bob S. Perkins Research Conference, Gulf Coast Section of SEPM, 203-235.

Withjack, M. O., Schlische, R.W., & Baum, M.S. (2009). Extensional development of the Fundy rift basin, southeastern Canada. *Geological Journal*, 44, 631-651.

Withjack, M. O., Schlische, R. W., Malinconico, M. L., & Olsen, P. E. (2012a). Rift-basin development: Lessons from the Triassic-Jurassic Newark basin of eastern North America. Geological Society, London, Special Publications, 369, 301-321.

Withjack, M. O., Schlische, R. W., & Olsen, P. E. (1998). Diachronous rifting, drifting, and inversion on the passive margin of Central Eastern North America: An analog for other passive margins. *AAPG Bulletin*, 82 (5A), 817-835.

Withjack, M. O., Schlische, R. W., & Olsen, P.E. (2012b). Development of the passive margin of eastern North America: Mesozoic rifting, igneous activity, and breakup. In Roberts, D. G. & Bally, A. W. (Eds.), *Regional geology and tectonics: Phanerozoic rift systems and sedimentary basins*. New York, Elsevier, 301-335.

Table 1. Reduced stress tensor from Economy Point. R and R' are the stress ratio and the stress index, respectively.

Stress State	*N*	σ_1	σ_2	σ_3	*R*	*R'*	*Stress Regime*	*Stress Symbol*
E-A	18	127º/10º	291º/79º	036º/03º	0.50	1.50	Strike-Slip-Faulting	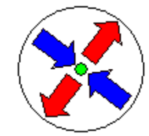

Table 2. Reduced stress tensors from Five Islands assuming fracture formation and/or reactivation after tilting. R and R' are the stress ratio and the stress index, respectively.

Stress State	*N*	σ_1	σ_2	σ_3	*R*	*R'*	*Stress Regime*	*Stress Symbol*
F1-A	9	106º/67º	268º/22º	001º/06º	0.95	0.95	Transtensional Faulting	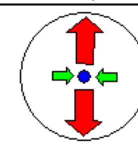
F1-B	10	005º/19º	197º/71º	096º/04º	0.10	1.90	Transpressional Faulting	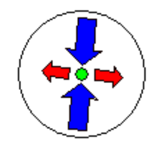
F1-C	7	289º/21º	109º/68º	019º/00º	0.70	1.30	Strike-Slip Faulting	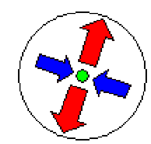
F1-D	3	094º/76º	225º/09º	317º/11º	0.35	0.35	Normal Faulting	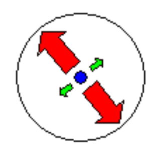

Table 3. Reduced stress tensors from Five Islands assuming fracture formation and/or reactivation before tilting. R and R' are the stress ratio and the stress index, respectively.

Stress State	*N*	σ_1	σ_2	σ_3	*R*	*R'*	*Stress Regime*	*Stress Symbol*
F2-A	9	103º/76º	269º/14º	000º/03º	0.80	0.80	Transtensional Faulting	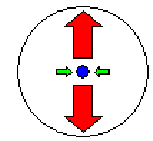
F2-B	8	009º/06º	247º/79º	100º/09º	0.40	1.60	Strike-Slip Faulting	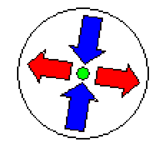
F2-C	6	131º/61º	297º/29º	030º/06º	0.61	0.61	Normal Faulting	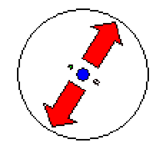
F2-D	3	007º/68º	230º/16º	136º/14º	0.35	0.35	Normal Faulting	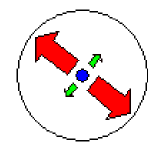

Table 4. Reduced stress tensors from Blue Sac assuming fracture formation and/or reactivation after tilting. R and R' are the stress ratio and the stress index, respectively.

Stress State	*N*	σ_1	σ_2	σ_3	*R*	*R'*	*Stress Regime*	*Stress Symbol*
B1-A	4	156º/80º	000º/09º	270º/04º	0.49	0.49	Normal Faulting	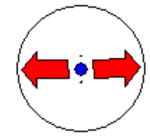
B1-B	17	203º/17º	059º/69º	297º/11º	0.77	1.23	Transtensional Faulting	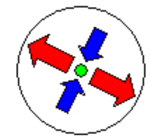
B1-C	4	310º/21º	106º/67º	217º/08º	0.10	1.90	Transpressional Faulting	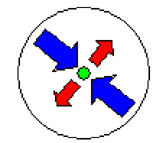

Table 5. Reduced stress tensors from Blue Sac assuming fracture formation and/or reactivation before tilting. R and R' are the stress ratio and the stress index, respectively.

Stress State	*N*	σ_1	σ_2	σ_3	*R*	*R'*	*Stress Regime*	*Stress Symbol*
B2-A	12	170º/68º	023º/19º	289º/11º	0.54	0.54	Normal Faulting	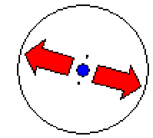
B2-B	8	016º/00º	126º/89º	286º/01º	0.57	1.43	Strike-Slip Faulting	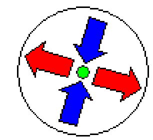
B2-C	5	102º/13º	270º/77º	012º/03º	0.25	1.75	Transpressional Faulting	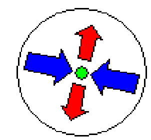
B2-D	4	292º/64º	166º/16º	070º/20º	0.38	0.38	Normal Faulting	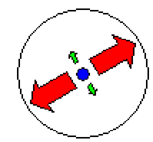

Table 6. Overprinting relationships at Blue Sac.

Fracture ID	*Type of feature*	*Relative timing*	*Stress state (Scenario 1)*	*Stress state (Scenario 2)*
2	Slickenlines	Older	-	B2-C
3	Slickenlines	Younger	B1-C	B2-C
8	Slickenlines	Older	B1-A	B2-D
9	Slickenlines	Younger	B1-B	B2-A
10	Slickenlines	Older	B1-A	B2-D
11	Slickenlines	Younger	-	B2-A
12	Slickenlines	Older	B1-A	B2-D
13	Slickenlines	Younger	B1-B	B2-A
14	Slickenlines	Youngest	B1-B	B2-A
15	Slickenlines	Older	B1-B	B2-A
16	Slickenlines	Younger	B1-B	B2-A

Table 7. Reduced stress tensors from Wasson Bluff assuming fracture formation and/or reactivation after tilting. R and R' are the stress ratio and the stress index, respectively.

Stress State	*N*	σ_1	σ_2	σ_3	*R*	*R'*	*Stress Regime*	*Stress Symbol*
W1-A	19	209º/60º	019º/30º	111º/04º	0.50	0.50	Normal Faulting	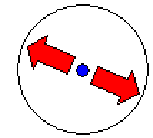
W1-B	13	031º/51º	276º/19º	173º/33º	0.50	0.50	Normal Faulting	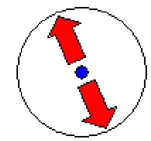
W1-C	13	049º/11º	259º/77º	140º/06º	0.00	2.00	Transpressional Faulting	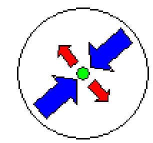

Table 8. Reduced stress tensors from Wasson Bluff assuming fracture formation and/or reactivation before tilting. R and R' are the stress ratio and the stress index, respectively.

Stress State	*N*	σ_1	σ_2	σ_3	*R*	*R'*	*Stress Regime*	*Stress Symbol*
W2-A	12	124º/81º	034º/00º	304º/09º	0.60	0.60	Normal Faulting	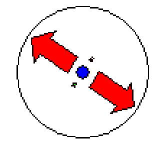
W2-B	12	079º/61º	249º/29º	342º/04º	0.50	0.50	Normal Faulting	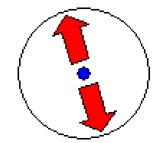
W2-C	13	202º/58º	344º/26º	083º/17º	0.25	0.25	Radial-Normal Faulting	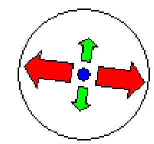
W2-D	7	035º/18º	175º/67º	301º/14º	0.15	1.85	Transpressional Faulting	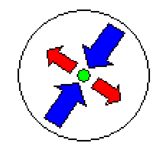

Table 9. Overprinting and cross-cutting relationships at Wasson Bluff.

Fracture ID	*Type of feature*	*Relative timing*	*Stress state (Scenario 1)*	*Stress state (Scenario 2)*
33 to 35	Tension fractures filled with red mudstone	Older	W1-A	W2-A / W2-C
36 to 46	Silica ± zeolite vein	Younger	W1-B	W2-B
46	Tension fracture	Older	W1-B	W2-B
47	Fault with reverse separation. Offsets 46	Younger	-	W2-C

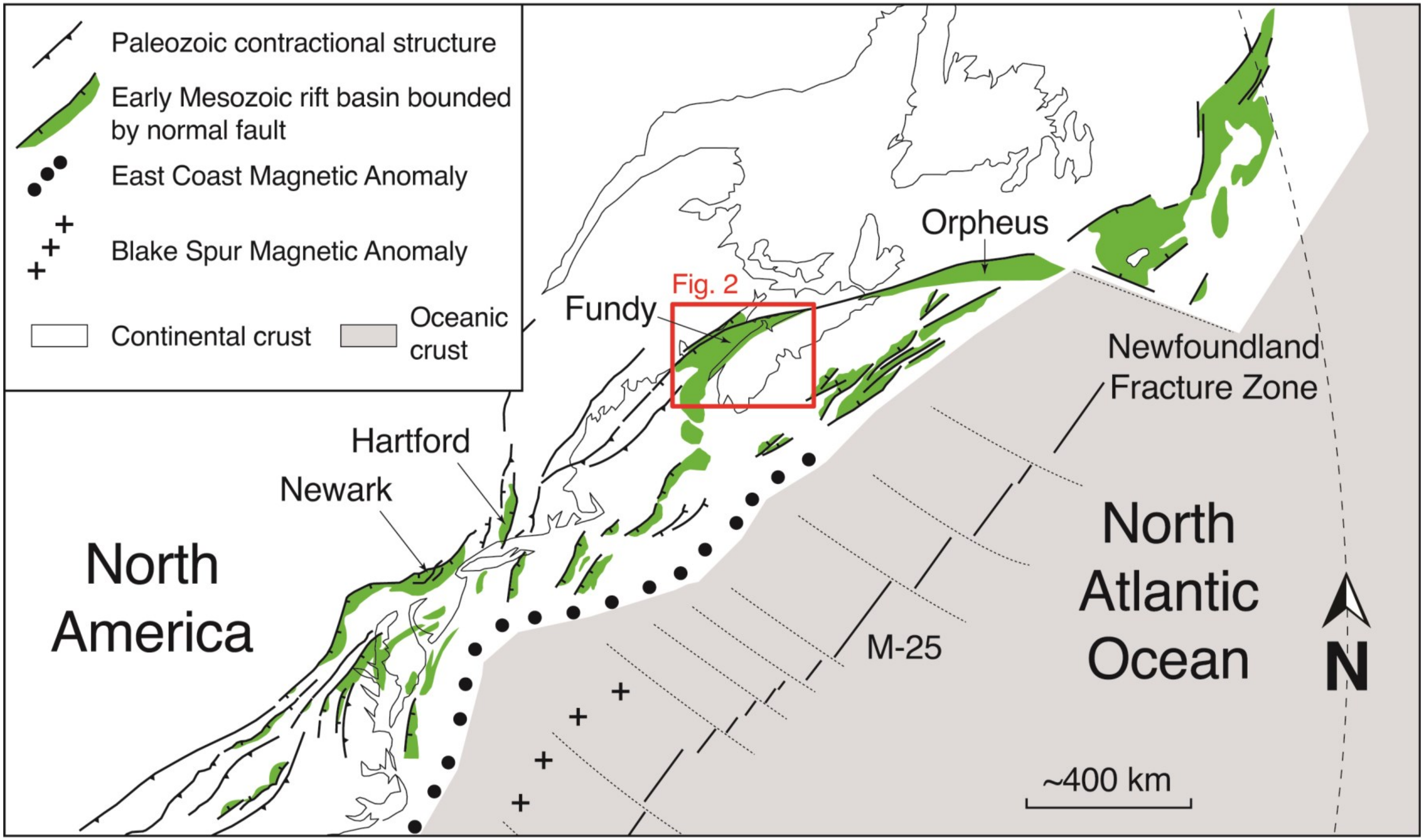

Figure 1. Regional tectonic map showing Mesozoic rift basins in eastern North America (modified from Withjack et al., 2012b). The Fundy and Orpheus rift basins share a common border-fault zone.

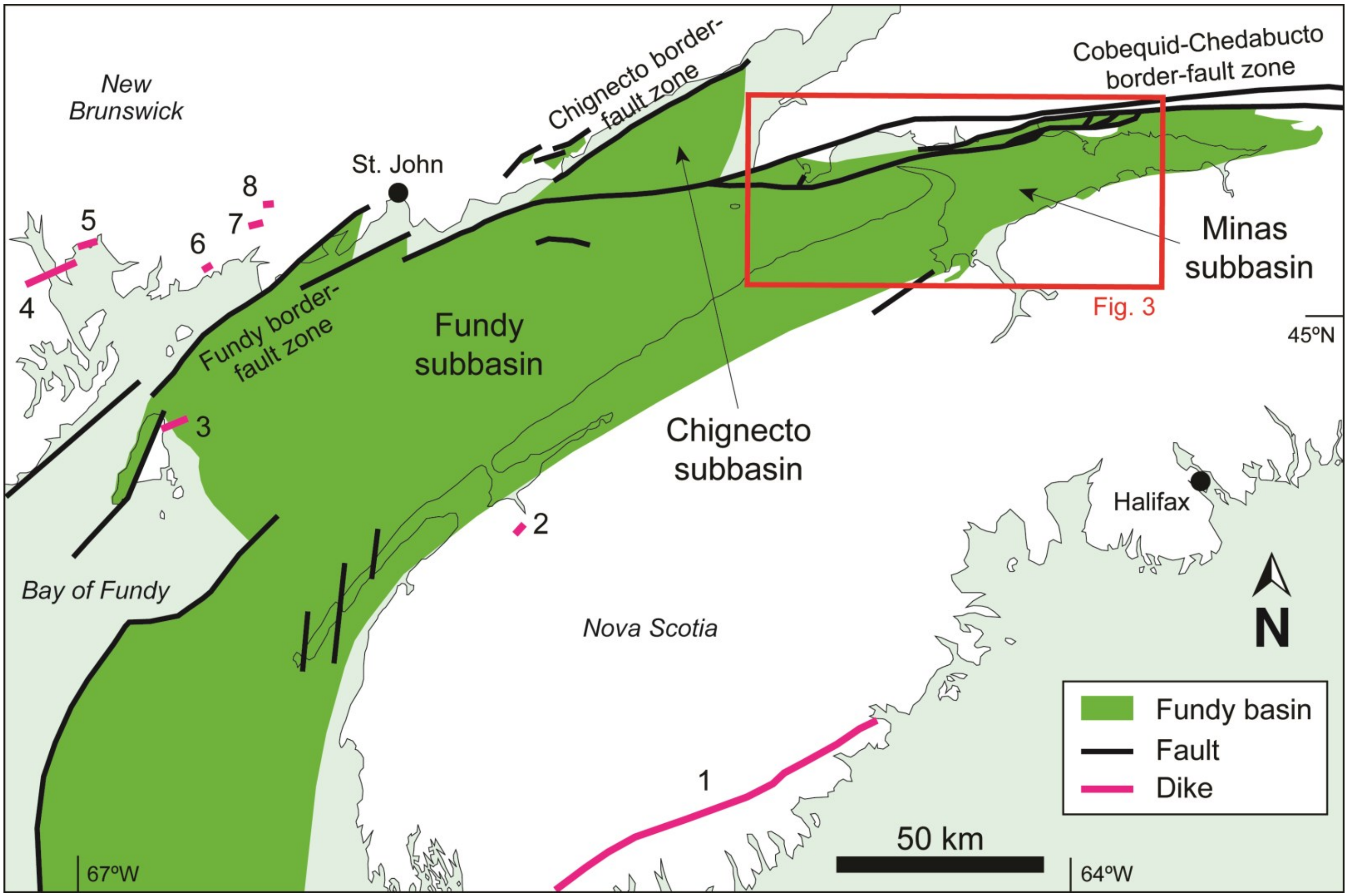

Figure 2. Tectonic map of the Fundy rift basin showing border-fault zones, subbasins and dikes. 1: Shelburne dike; 2: Lansdowne dike; 3: Shallowhead Tail dike; 4 and 5: Minister Island dikes; 6: Buckman's Creek dike; 7: New River dike; 8: Lepreau River dike. Dike location from McHone (2003) and Kontak (2008). Basin geometry and fault location from Withjack & Schlische (2005).

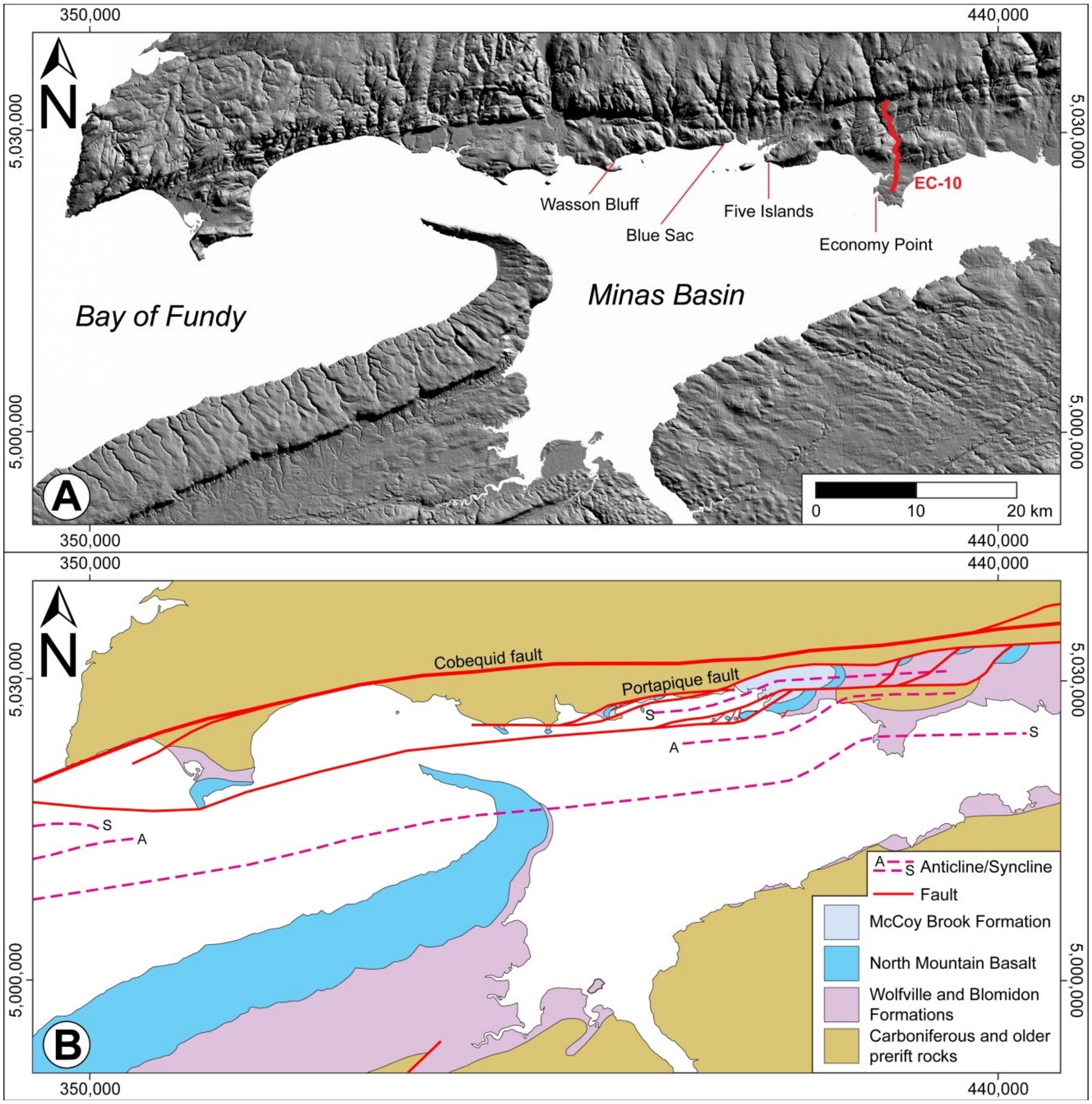

Figure 3. Location and geology of the study area. A) Shaded relief map based on digital elevation model of the eastern part of the Minas subbasin (Nova Scotia) showing the four study sites and seismic line EC-10. The projected coordinate system for this and subsequent maps is NAD 1983 UTM Zone 20N. DEM retrieved from Fisher et al. (2006). B) Geologic map of the same area (modified from Donohoe & Wallace [1982], and Withjack et al. [2009]). The Cobequid (also known as Minas) fault links to the Chedabucto fault in the east and forms the Cobequid-Chedabucto fault zone (Fig. 1), which is the border fault of the Fundy and Orpheus rift basins. See complete stratigraphy in Figure 4.

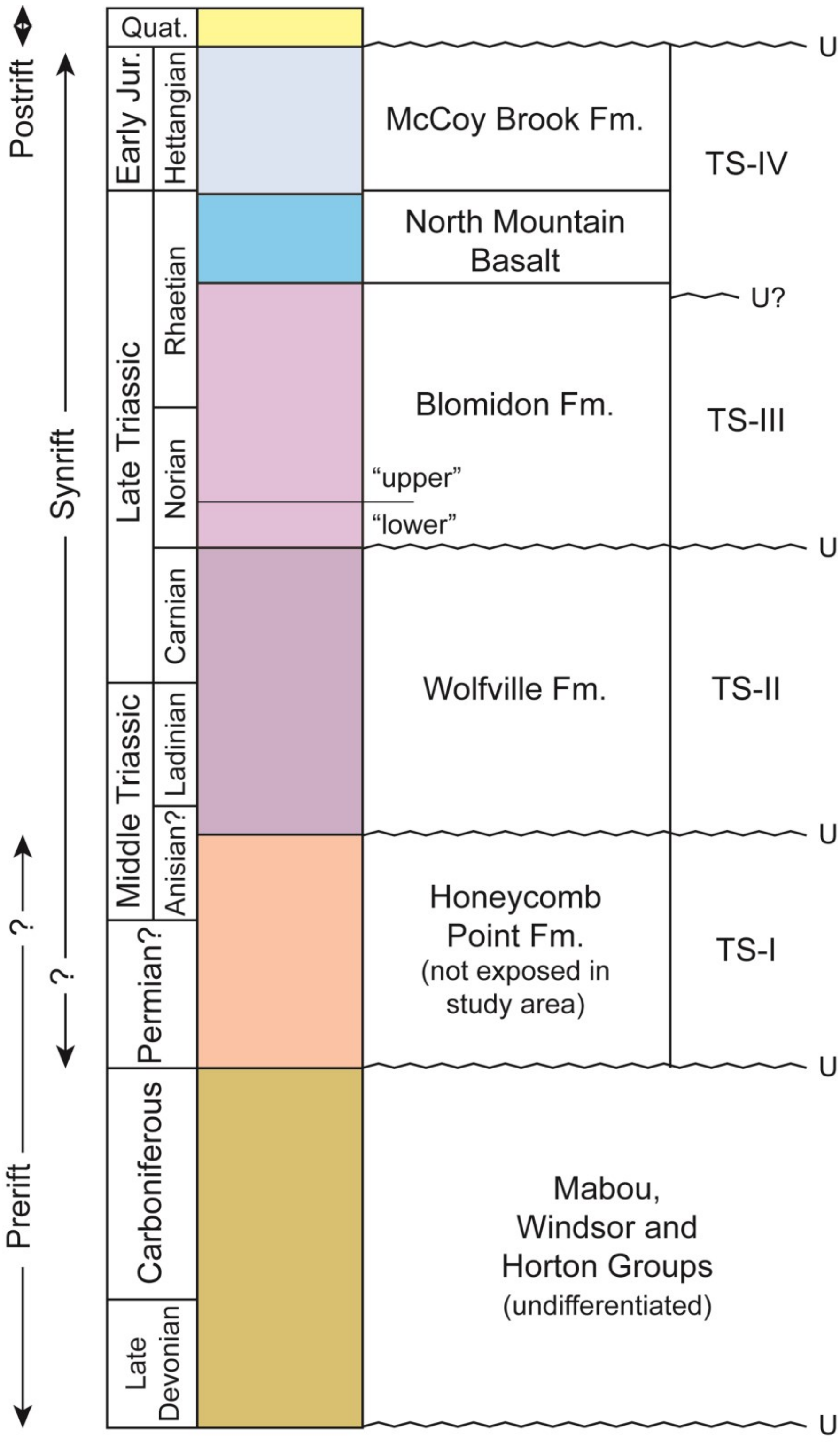

Figure 4. Stratigraphic column of the Fundy rift basin (modified from Wade [1996] and Withjack et al. [2009]). Units in subsequent maps have the same color scheme as the units in this figure. The prerift unit, undifferentiated in this study, only includes rocks from the northern shore of the Minas Basin. TS-I to TS-IV are the four tectonostratigraphic sequences from Olsen et al. (2000). U: unconformity.

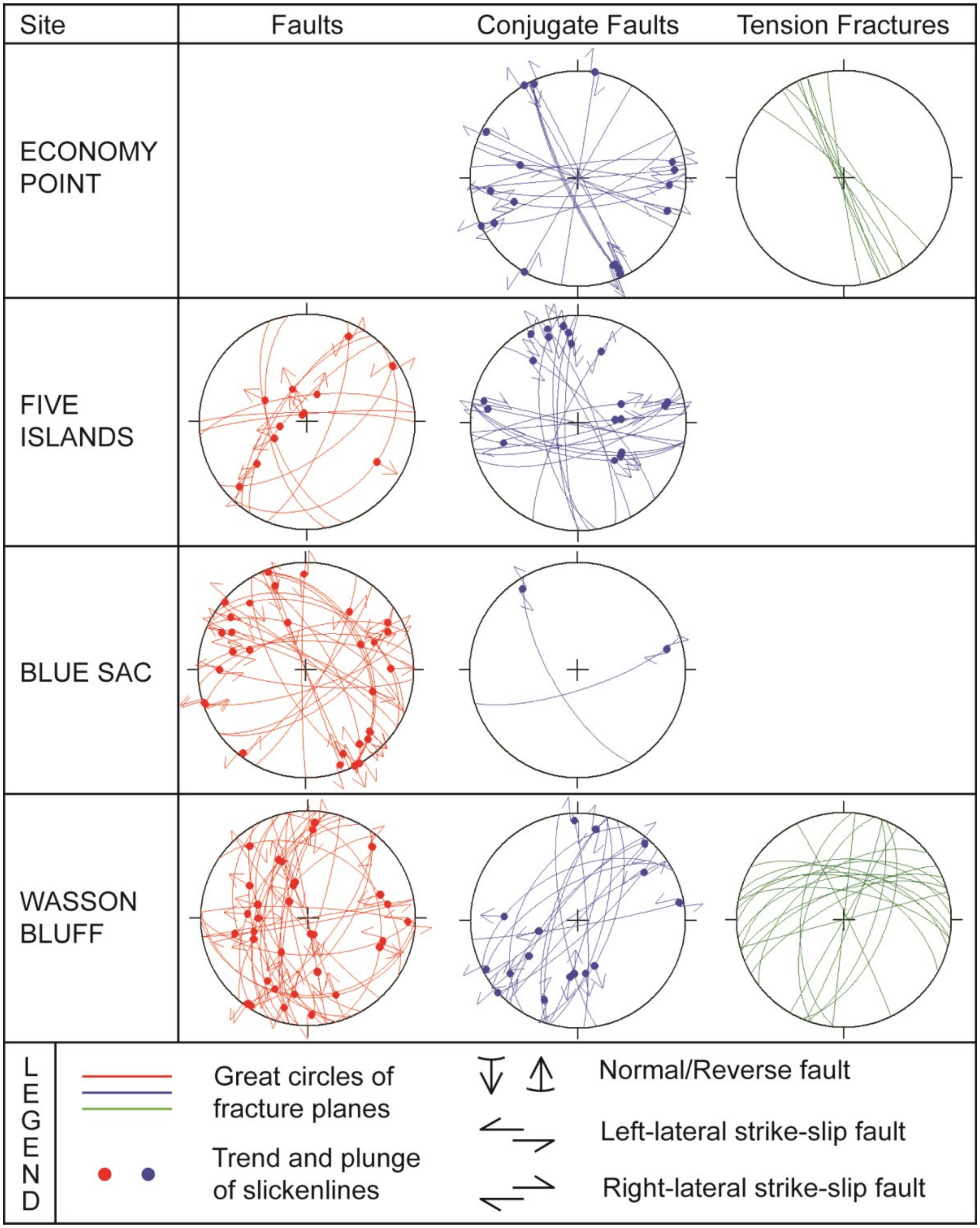

Figure 5. Equal-area stereographic projections of raw field data separated by class and site. The class 'faults' applies to fractures with slickenlines only. 'Conjugate faults' are pairs of primary fractures intersecting each other at ~60º. 'Tension fractures' show no evident shear and could be voids or filled with minerals or sediments.

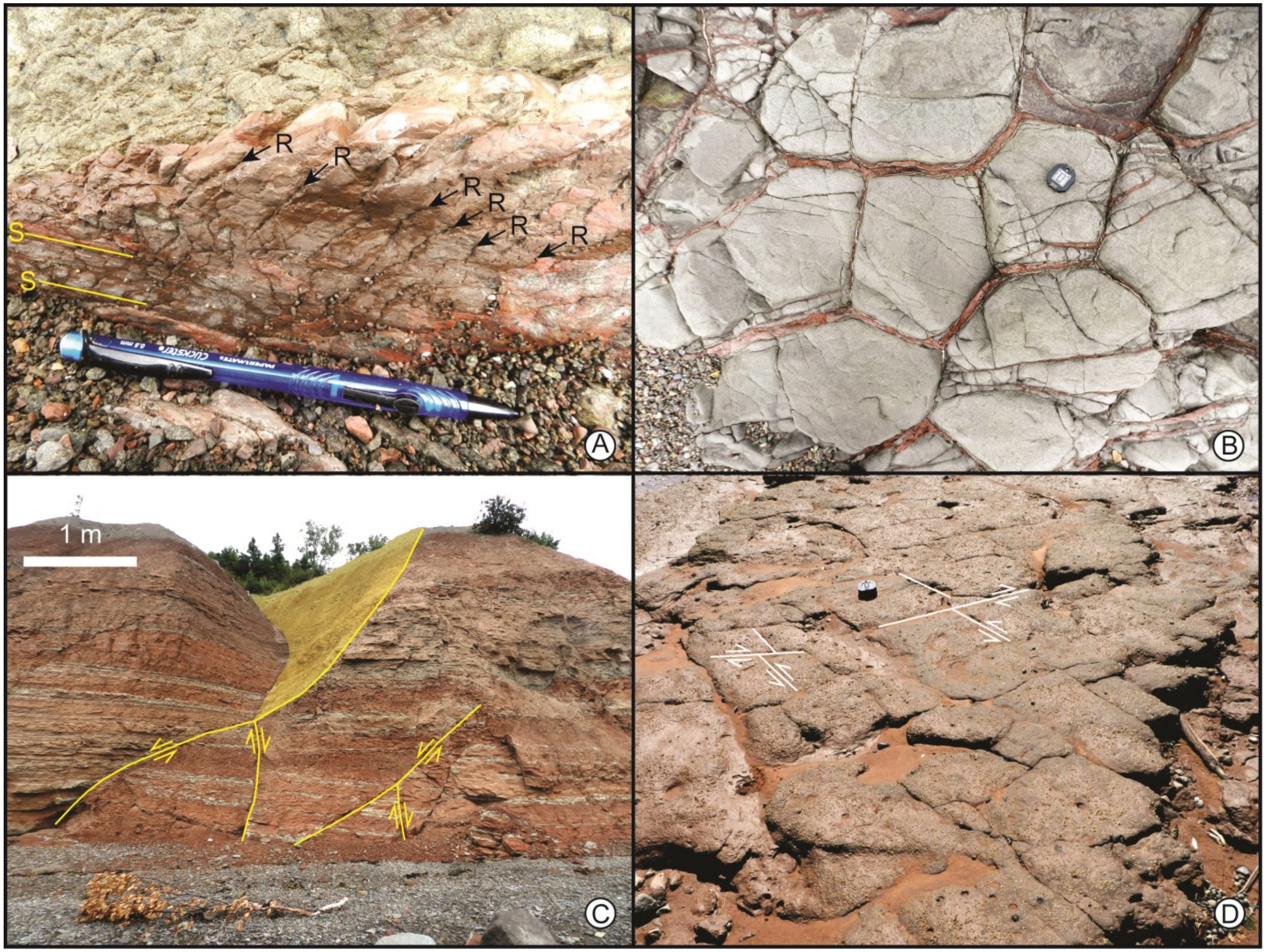

Figure 6. Examples of types of fractures. A) Fault bearing slickenlines (S) and Riedel shears (R) indicating left-lateral movement, and B) sediment-filled tension fractures in columnar basalt at Wasson Bluff. C) Conjugate normal faults at Wasson Bluff and D) conjugate strike-slip faults at Economy Point.

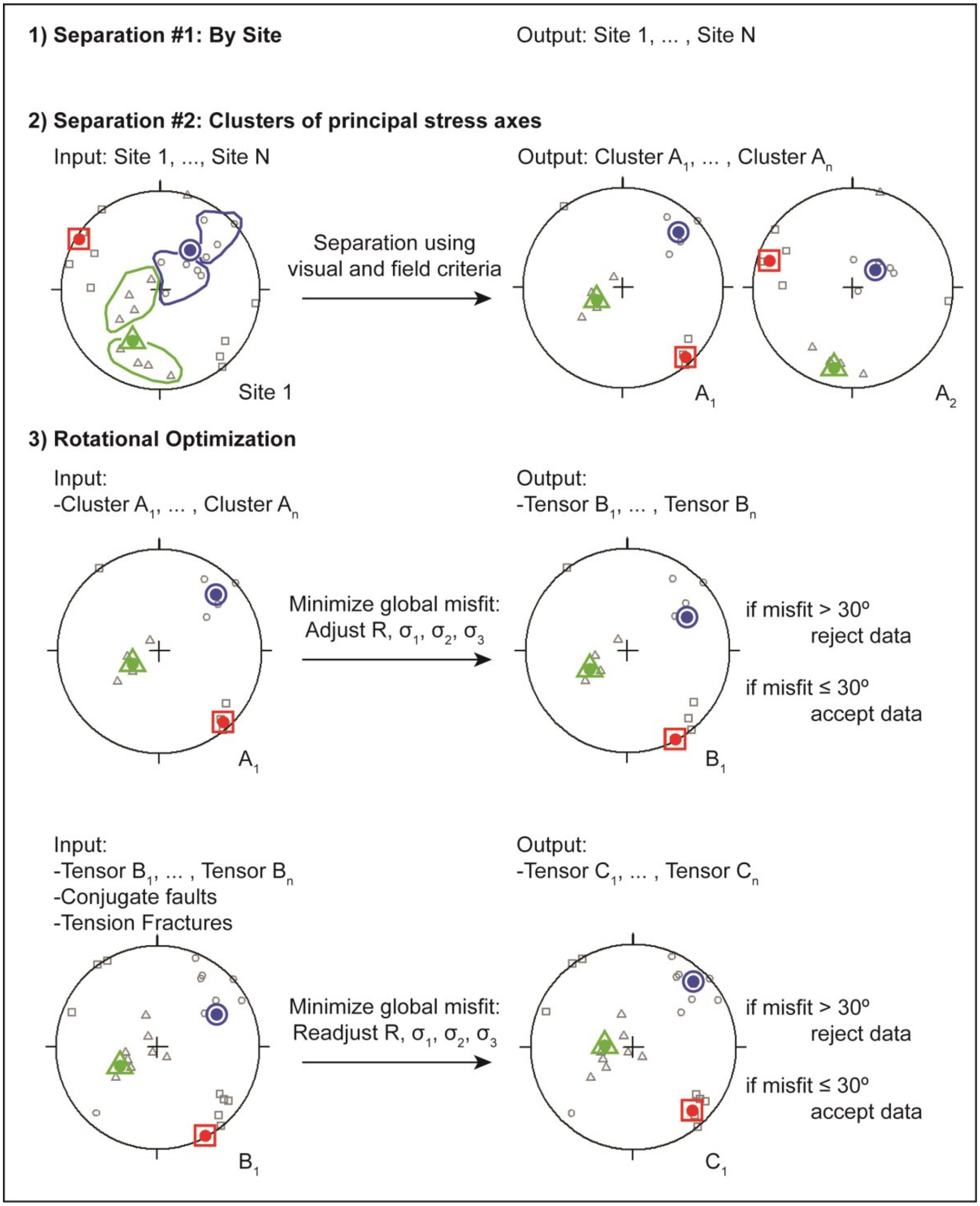

Figure 7. Stress inversion method using Win_TENSOR. Circles are the maximum principal stress (σ_1), triangles are the intermediate principal stress (σ_2) and squares are the minimum principal stress (σ_3). Small symbols represent the principal stress associated with individual fracture data points, whereas large symbols are the average principal stress axes. See text for discussion.

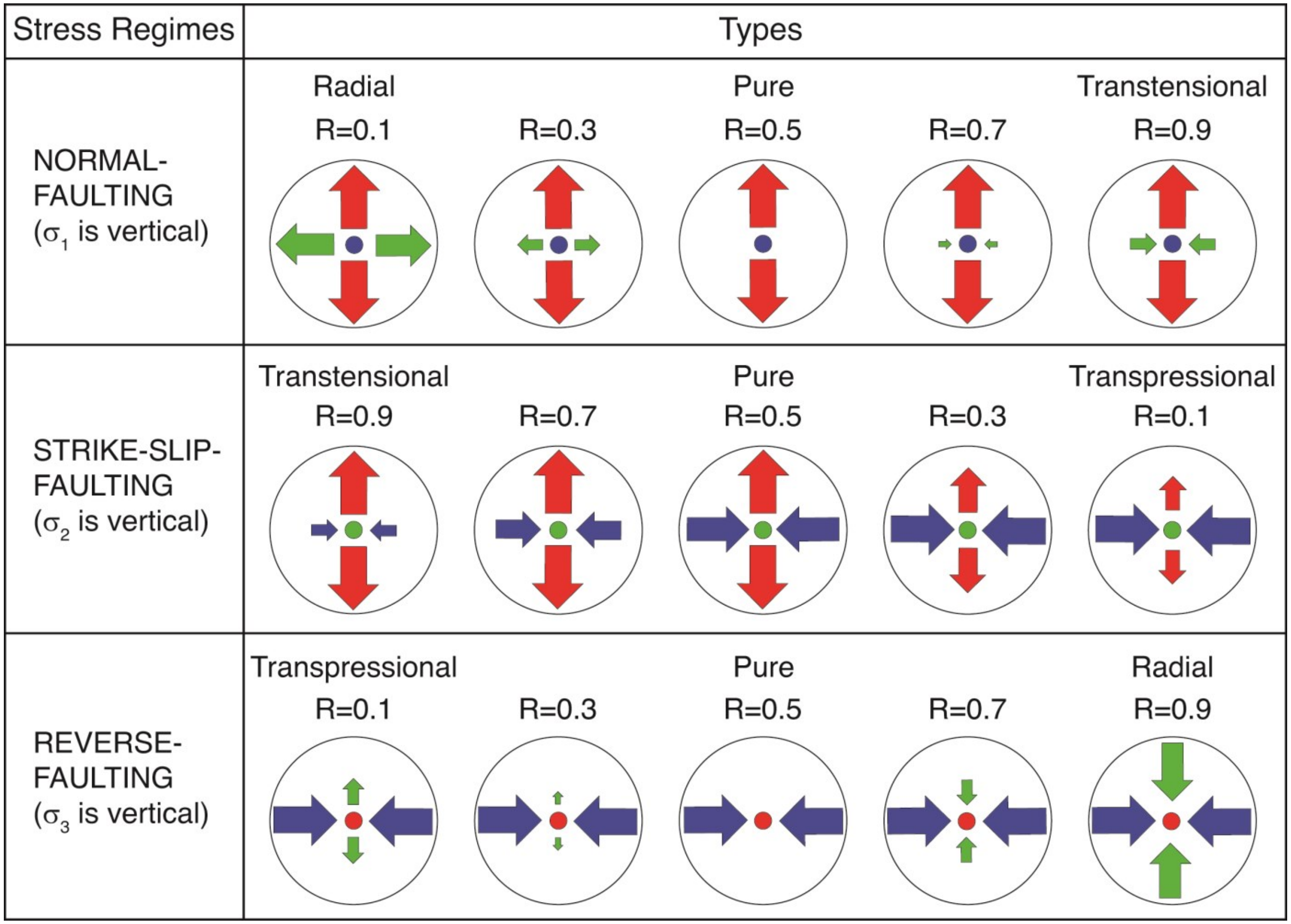

Figure 8. Stress symbols showing the minimum (red arrows), intermediate (green arrows) and maximum (blue arrows) stress directions in the three stress regimes (Delvaux et al.,1995, 1997). The arrows are the projections of the principal stress axes in the horizontal. Arrow lengths and types of stress regimes are function of R (stress ratio, $R = (\sigma_2-\sigma_3)/(\sigma_1-\sigma_3)$) and the stress regime.

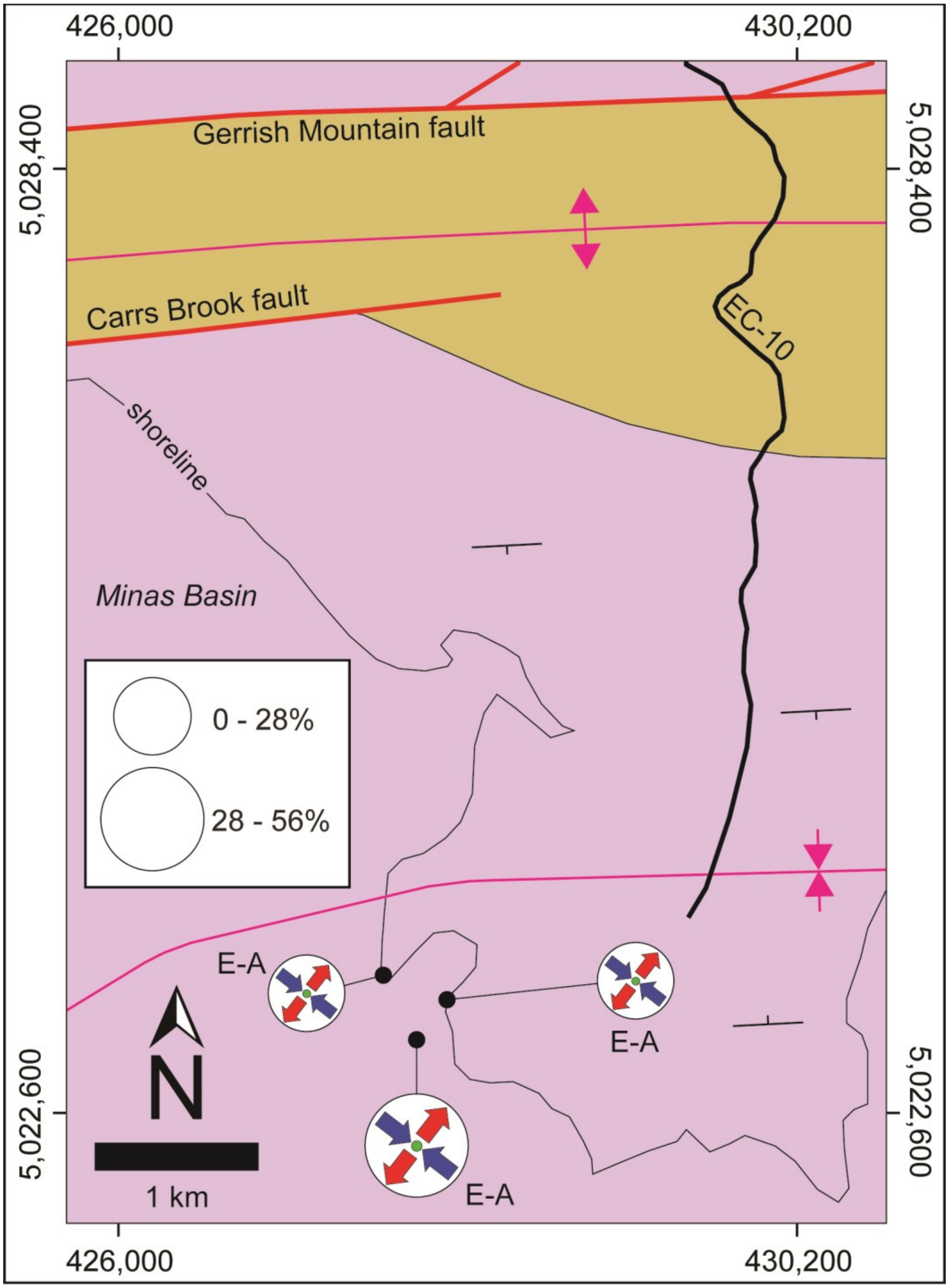

Figure 9. Geologic map of the western part of Economy Point (modified from Donohoe & Wallace, 1982) showing the distribution of stress state E-A at different subsites. The purple unit could be either Wolfville or lower Blomidon Formations. Percentages are based on the number of fractures contained in the stress state at each subsite relative to the total of fractures in the area (Appendices 1 to 3). Location and orientation of bedding symbols are inferred. See Appendix 1 for all symbols. See Figure 3 for full extension of seismic line EC-10.

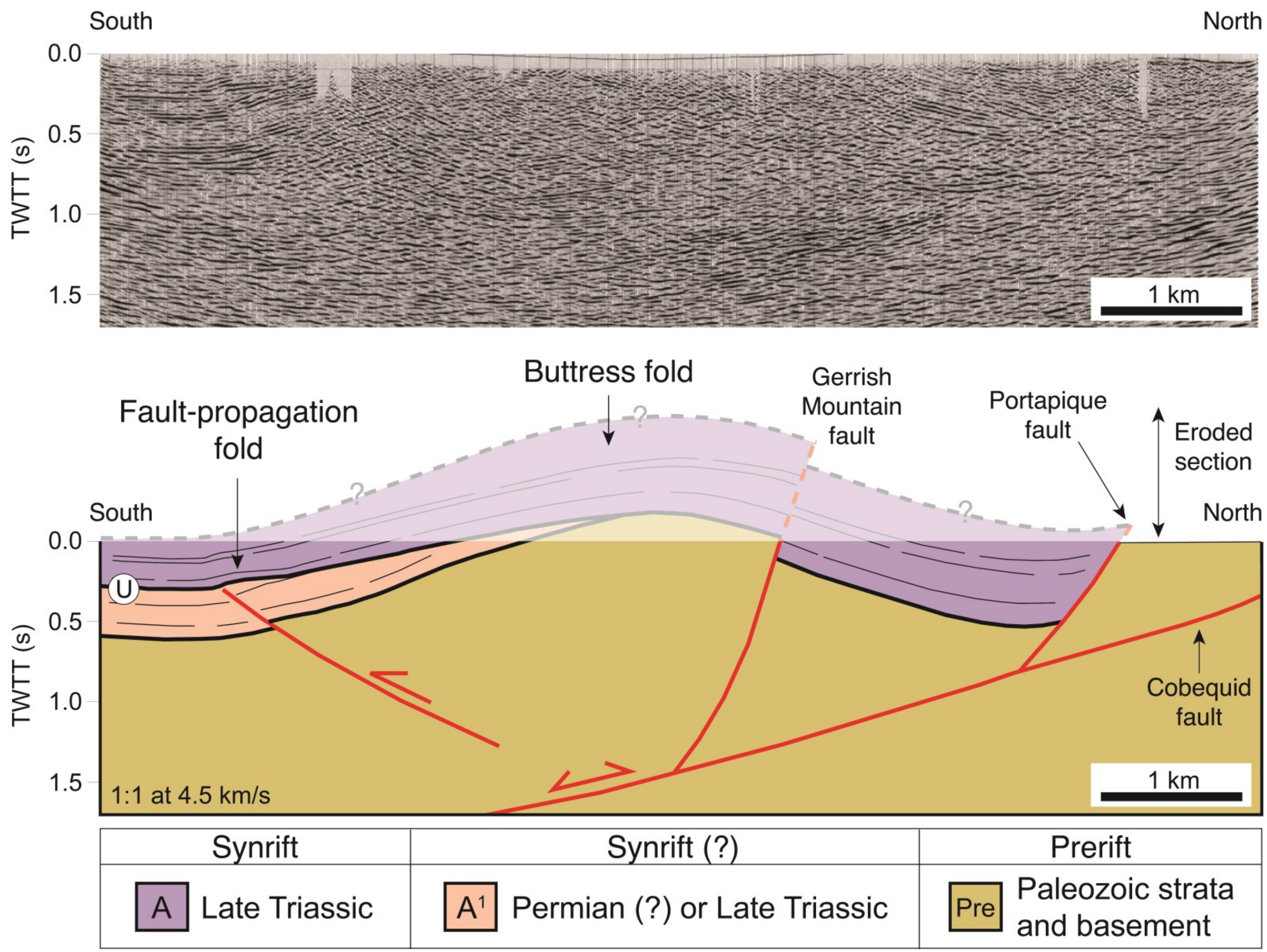
South
North
0.0
0.5
1.0
1.5
TWTT (s)
1 km
Buttress fold
Fault-propagation fold
Gerrish Mountain fault
Portapique fault
Eroded section
South
North
U
Cobequid fault
1:1 at 4.5 km/s
1 km
Synrift
Synrift (?)
Prerift
A
Late Triassic
A1
Permian (?) or Late Triassic
Pre
Paleozoic strata and basement

Figure 10 (on previous page). Uninterpreted (top) and interpreted (bottom) seismic line EC-10 from Economy Point (see Figure 3 for complete location) showing synrift and postrift deformation of three tectonostratigraphic packages. Unit A^1 is either the Honeycomb Point Formation or Wolfville Formation. Unit A is either the Wolfville Formation or "Lower" Blomidon Formation. The angular unconformity U separates Unit A^1 from Unit A. Reinterpreted after Withjack et al. (2010).

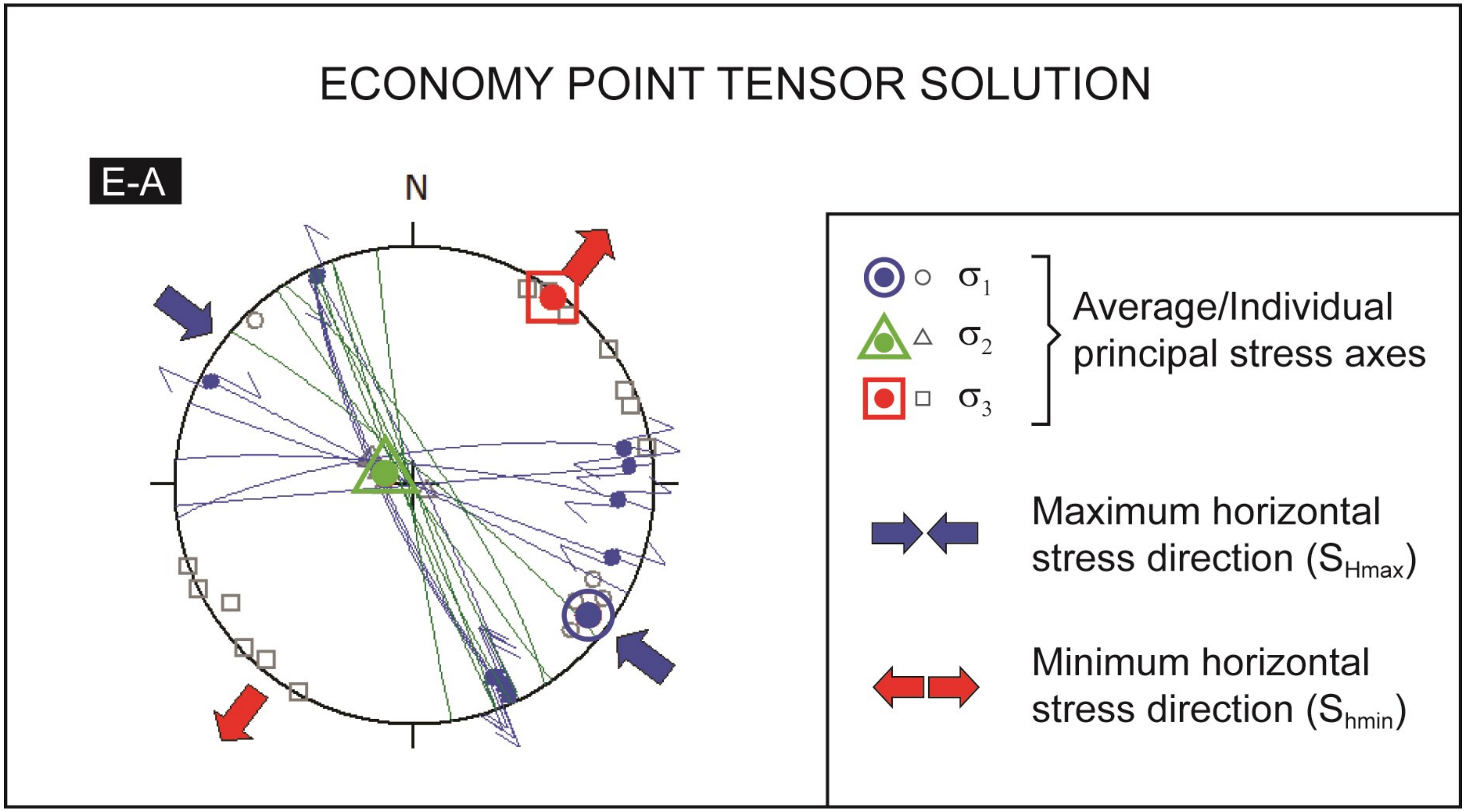

Figure 11. Reduced stress tensors and equal-area stereographic projections of fractures at Economy Point (see Appendices 1 to 3). The solution yields one stress state. The data from this site do not include horizontal-axis rotations because bedding is practically horizontal. See Figure 5 for color scheme of fractures.

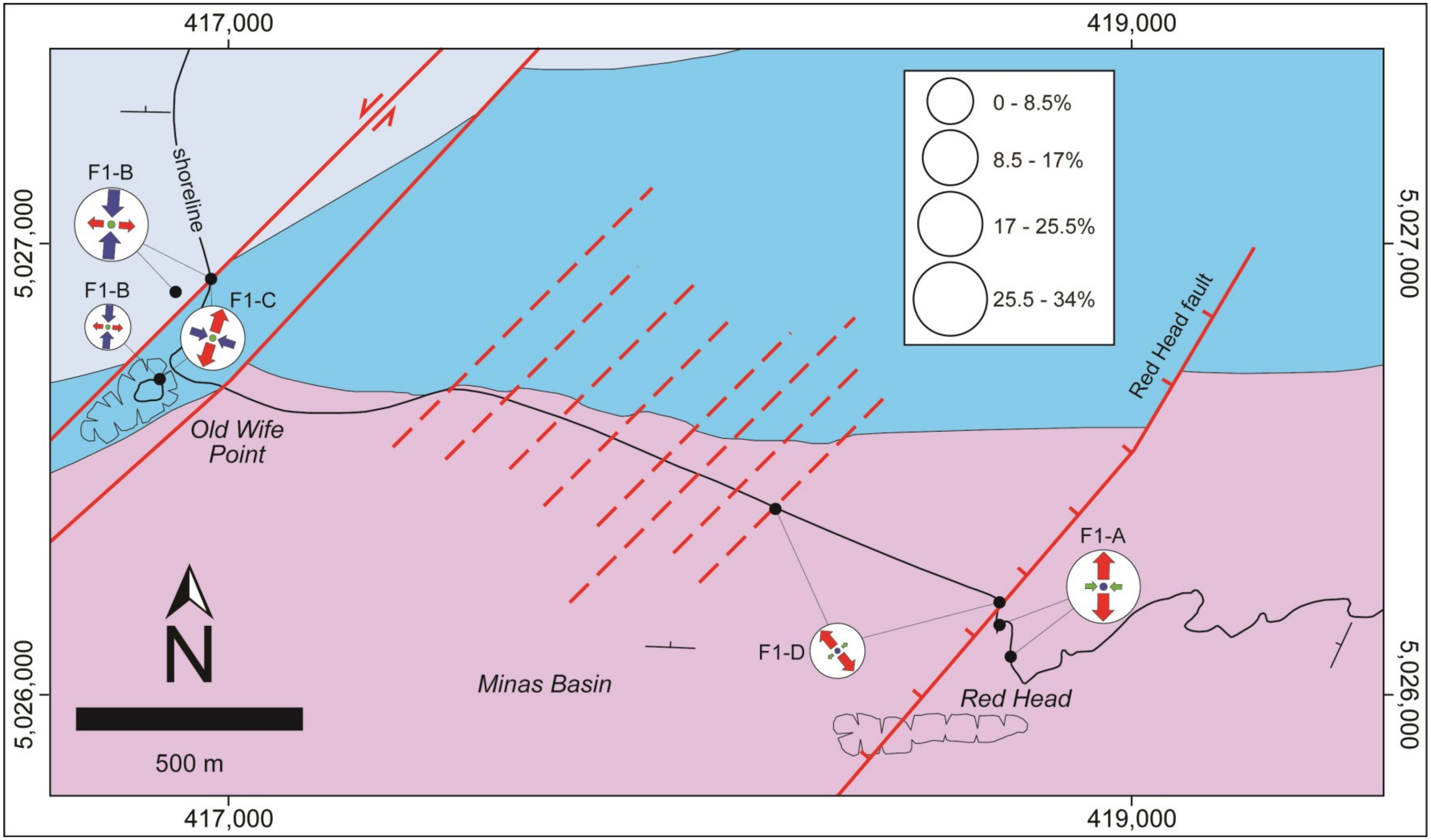

Figure 12. Geologic map of Five Islands (modified from Withjack et al., 2009) showing the distribution of stress states at different subsites, assuming fracture formation and/or reactivation occurred after tilting (scenario 1). Percentages are based on the number of fractures contained in the stress states at each subsite relative to the total of fractures in the area (see Appendices 4 to 6). Location and orientation of bedding symbols are inferred. See Figure 4 for color scheme, and Appendix 5 for all symbols.

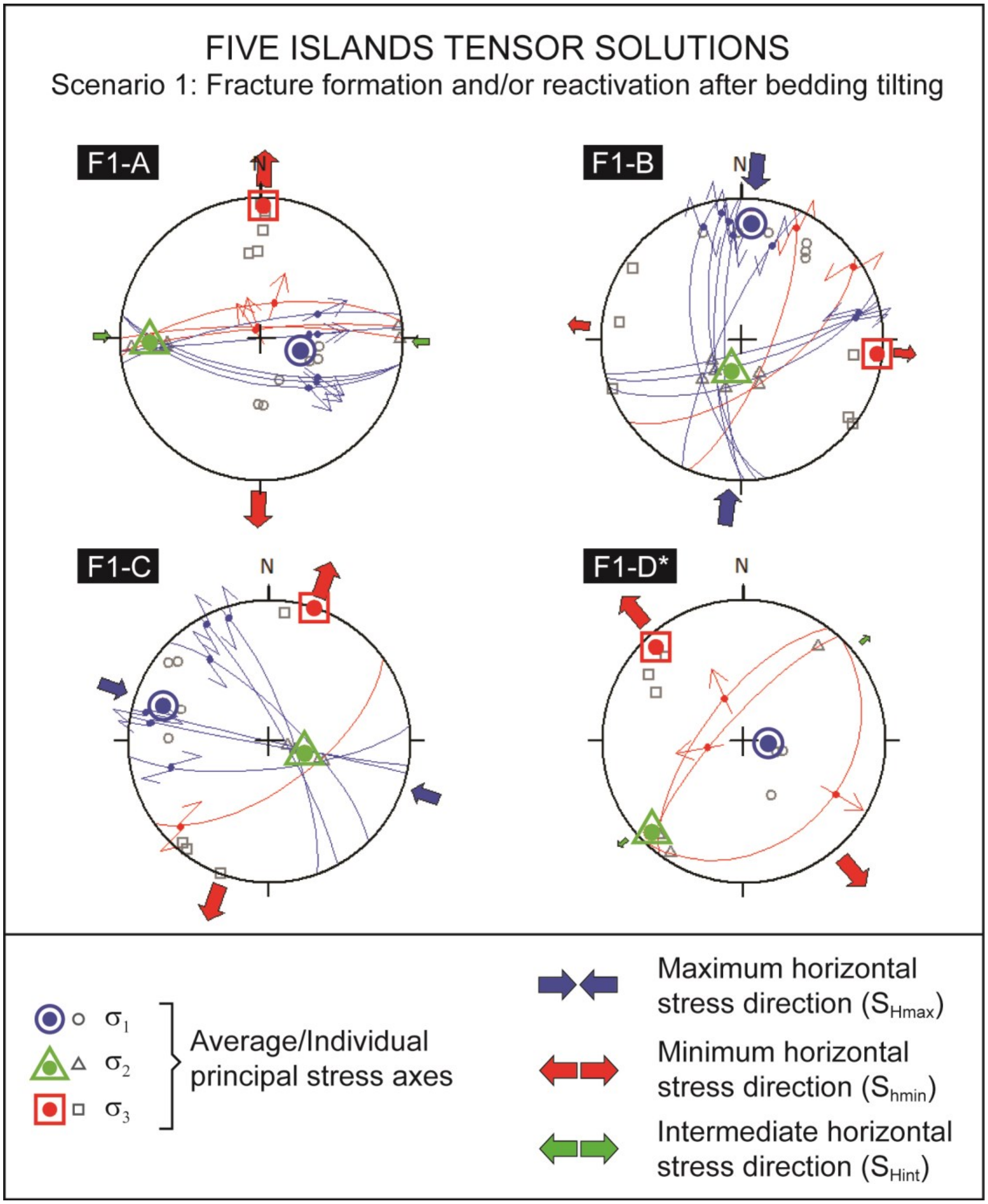

Figure 13. Reduced stress tensors and equal-area stereographic projections of fractures at Five Islands assuming fracture formation and/or reactivation occurred after bedding tilting (i.e., fractures used in stress inversion are in the present-day orientation; see Appendices 4 to 6). The solution yields four distinct stress states (A to D). Stress state D (marked with *) contains a lower number than the minimum required in the stress inversion, but they are key large-scale faults. See Figure 5 for color scheme of fractures.

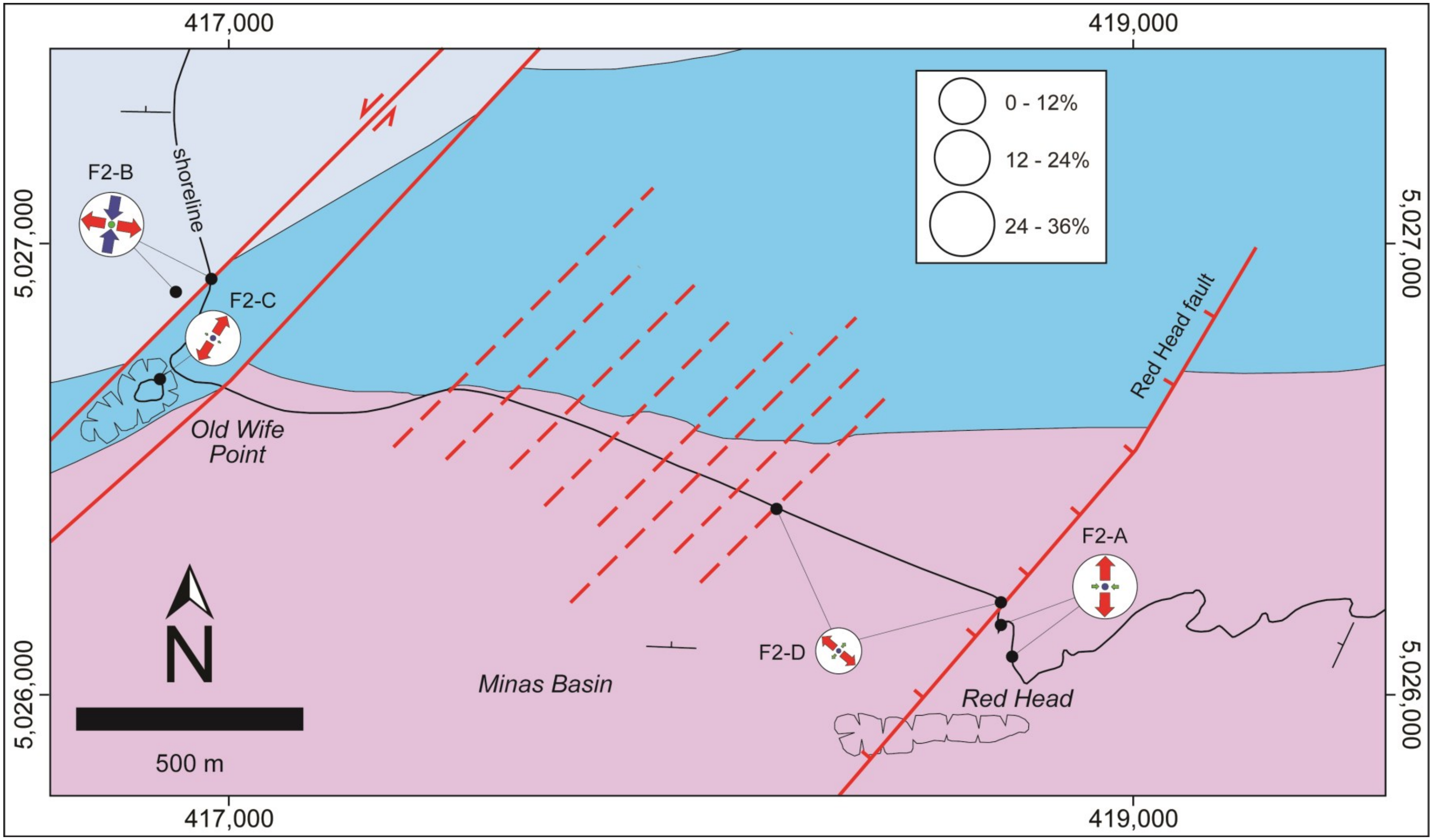

Figure 14. Geologic map of Five Islands (modified from Withjack et al., 2009) showing the distribution of stress states at different subsites, assuming fracture formation and/or reactivation occurred before tilting (scenario 2). Percentages are based on the number of fractures contained in the stress states at each subsite relative to the total of fractures in the area (see Appendices 4, 5 and 7). Location and orientation of bedding symbols are inferred. See Figure 4 for color scheme, and Appendix 4 for all symbols.

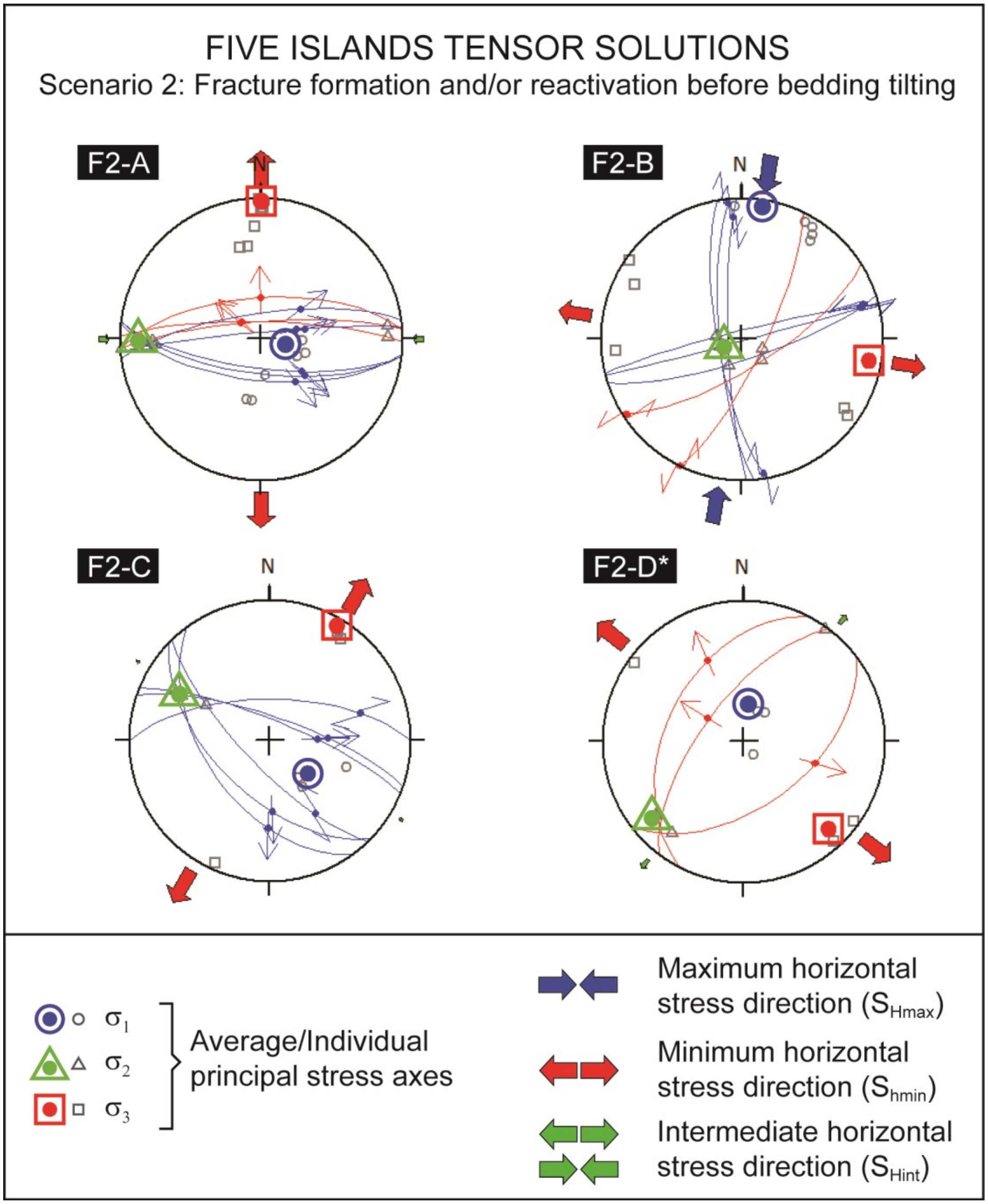

Figure 15. Reduced stress tensors and equal-area stereographic projections of fractures at Five Islands assuming fracture formation and/or reactivation before bedding tilting (i.e., fractures used in stress inversion are corrected for local bedding; see Appendices 4, 5 and 7). The solution yields four distinct stress states (A to D). Stress state D (marked with *) contains key large-scale faults in a smaller number than the minimum required in the stress inversion. See Figure 5 for color scheme of fractures.

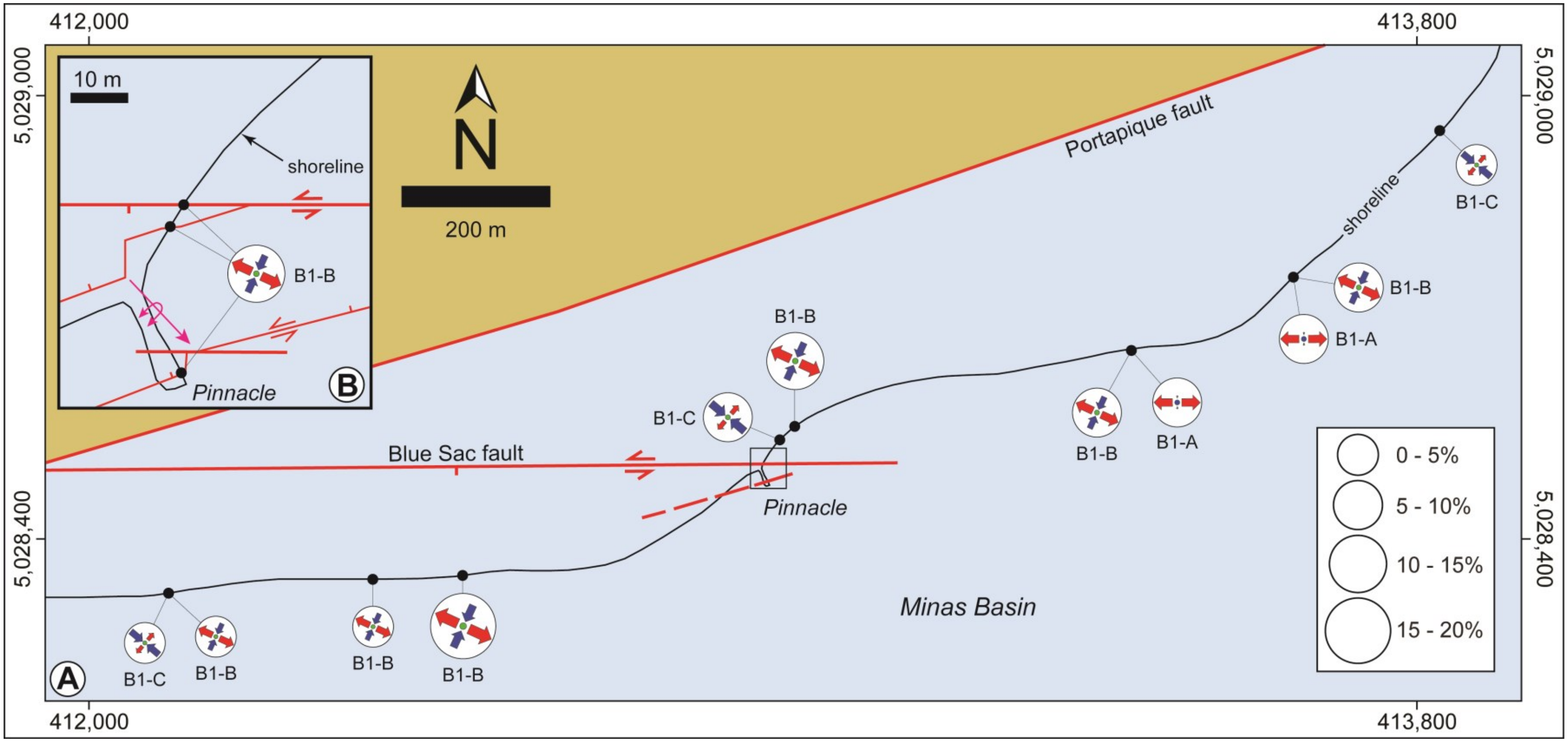

Figure 16. Geologic map of Blue Sac (modified from Withjack et al. [2010] and Donohoe & Wallace [1982]) showing the distribution of stress states at different subsites, assuming fracture formation and/or reactivation occurred after tilting (scenario 1). Percentages are based on the number of fractures contained in the stress states at each subsite relative to the total of fractures in the area (see Appendices 8 to 10). See Figure 4 for color scheme, and Appendix 8 for symbols.

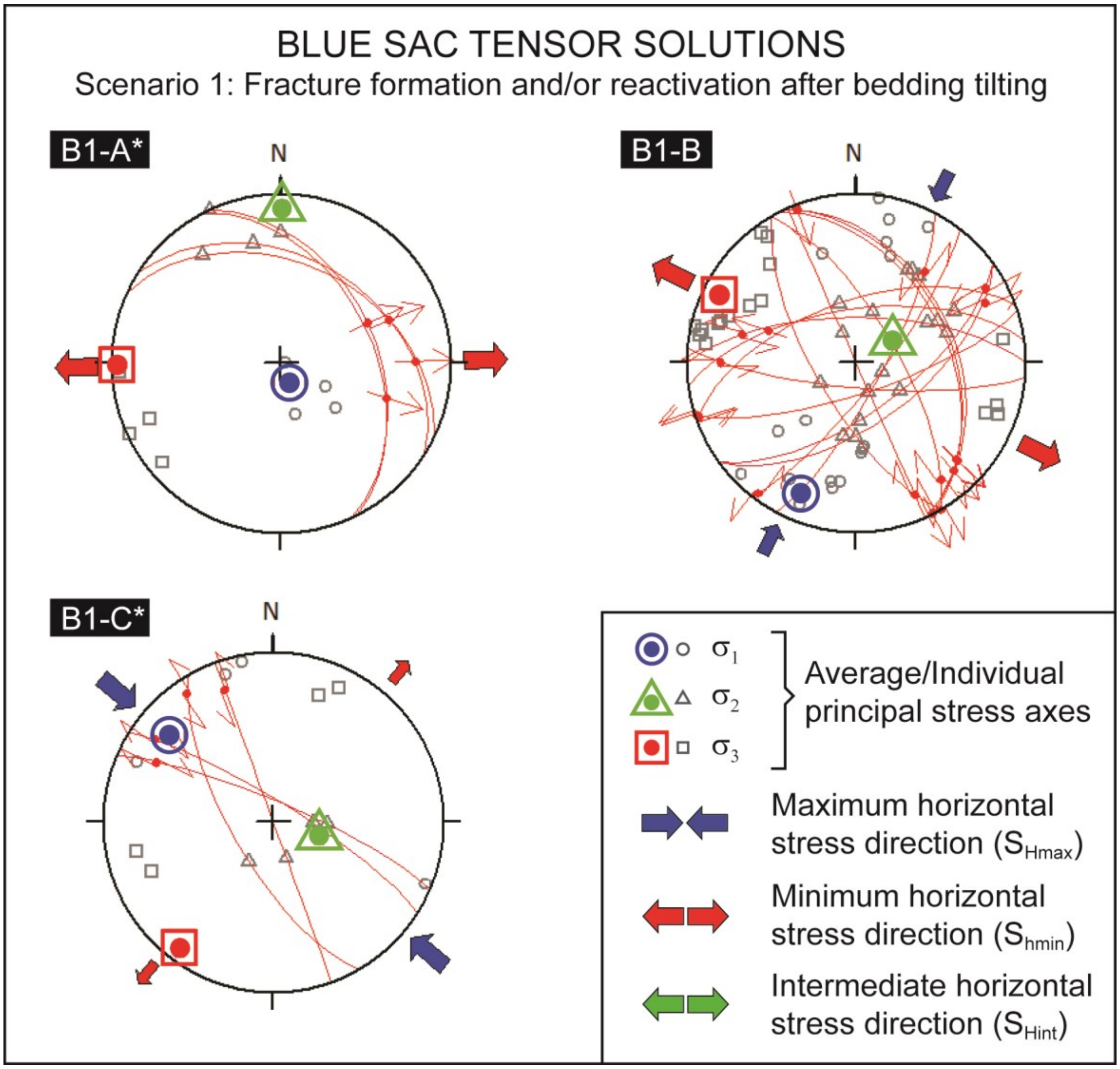

Figure 17. Reduced stress tensors and equal-area stereographic projections of fractures at Blue Sac assuming fracture formation and/or reactivation after bedding tilting (i.e., fractures used in stress inversion are in the present-day orientation; see Appendices 8 to 10). The solution yields three distinct stress states (A to C). Stress states A and D (marked with *) contain key faults in a smaller number than the minimum required in the stress inversion. See Figure 5 for color scheme of fractures.

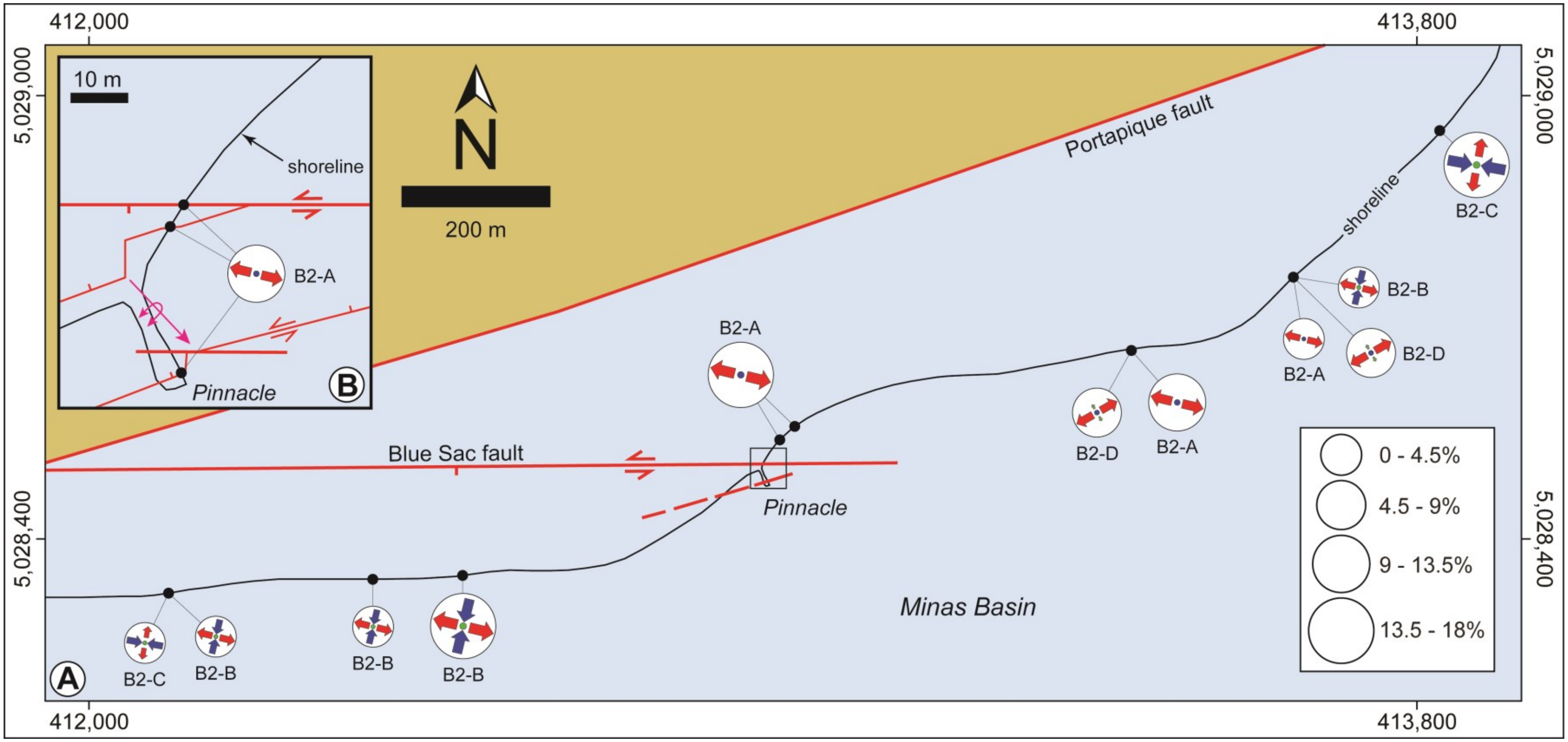

Figure 18. Geologic map of Blue Sac (modified from Withjack et al. [2010] and Donohoe & Wallace [1982]) showing the distribution of stress states at different subsites, assuming fracture formation and/or reactivation occurred before tilting (scenario 2). Percentages are based on the number of fractures contained in the stress states at each subsite relative to the total of fractures in the area (see Appendices 8, 9 and 11). See Figure 4 for color scheme, and Appendix 8 for symbols and bedding information.

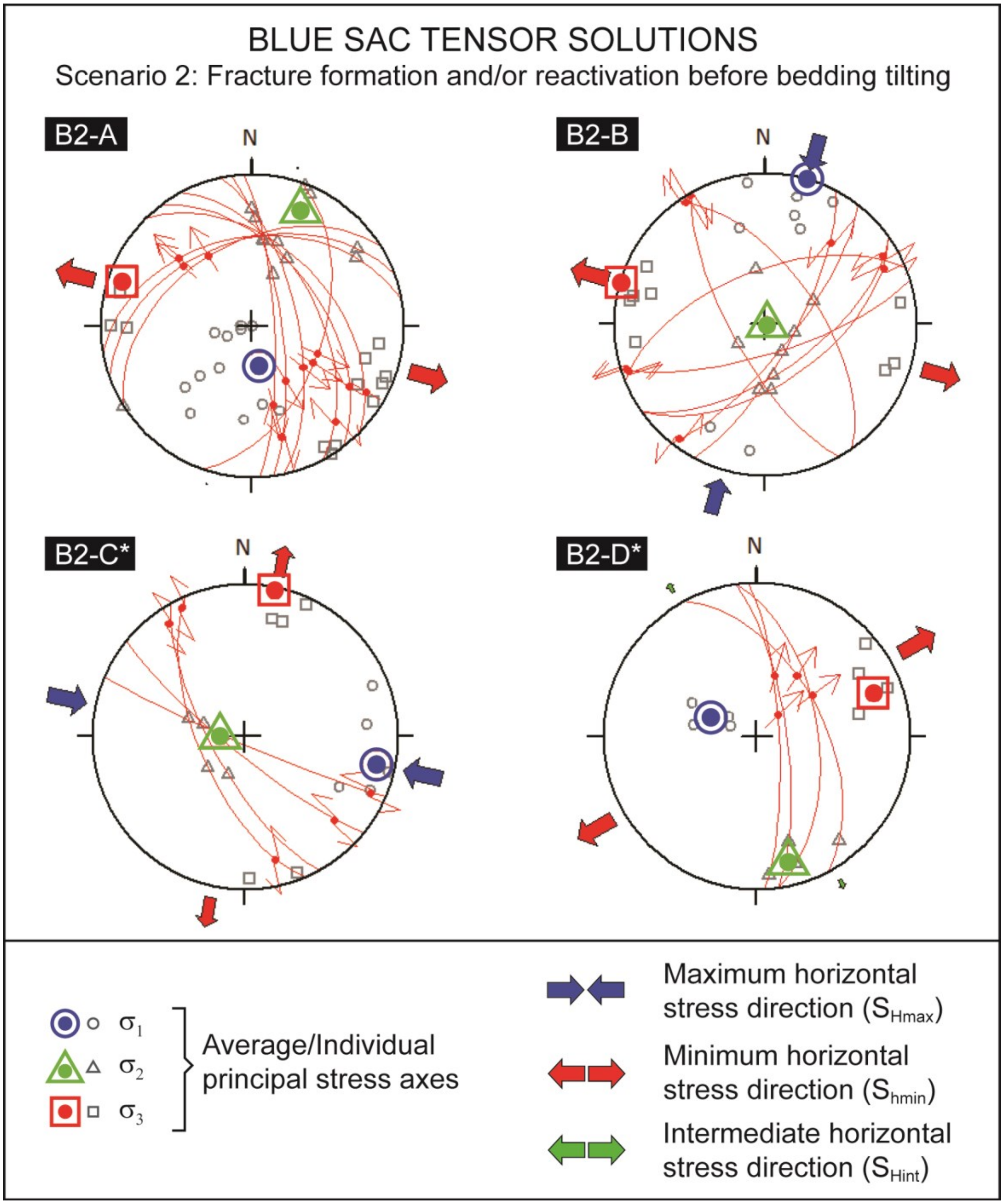

Figure 19. Reduced stress tensors and equal-area stereographic projections of fractures at Blue Sac assuming fracture formation and/or reactivation before bedding tilting (i.e., fractures used in stress inversion are corrected for local bedding; see Appendices 8, 9 and 11). The solution yields four distinct stress states (A to D). Stress states C and D (marked with *) contain key faults in a smaller number than the minimum required in the stress inversion. See Figure 5 for color scheme of fractures.

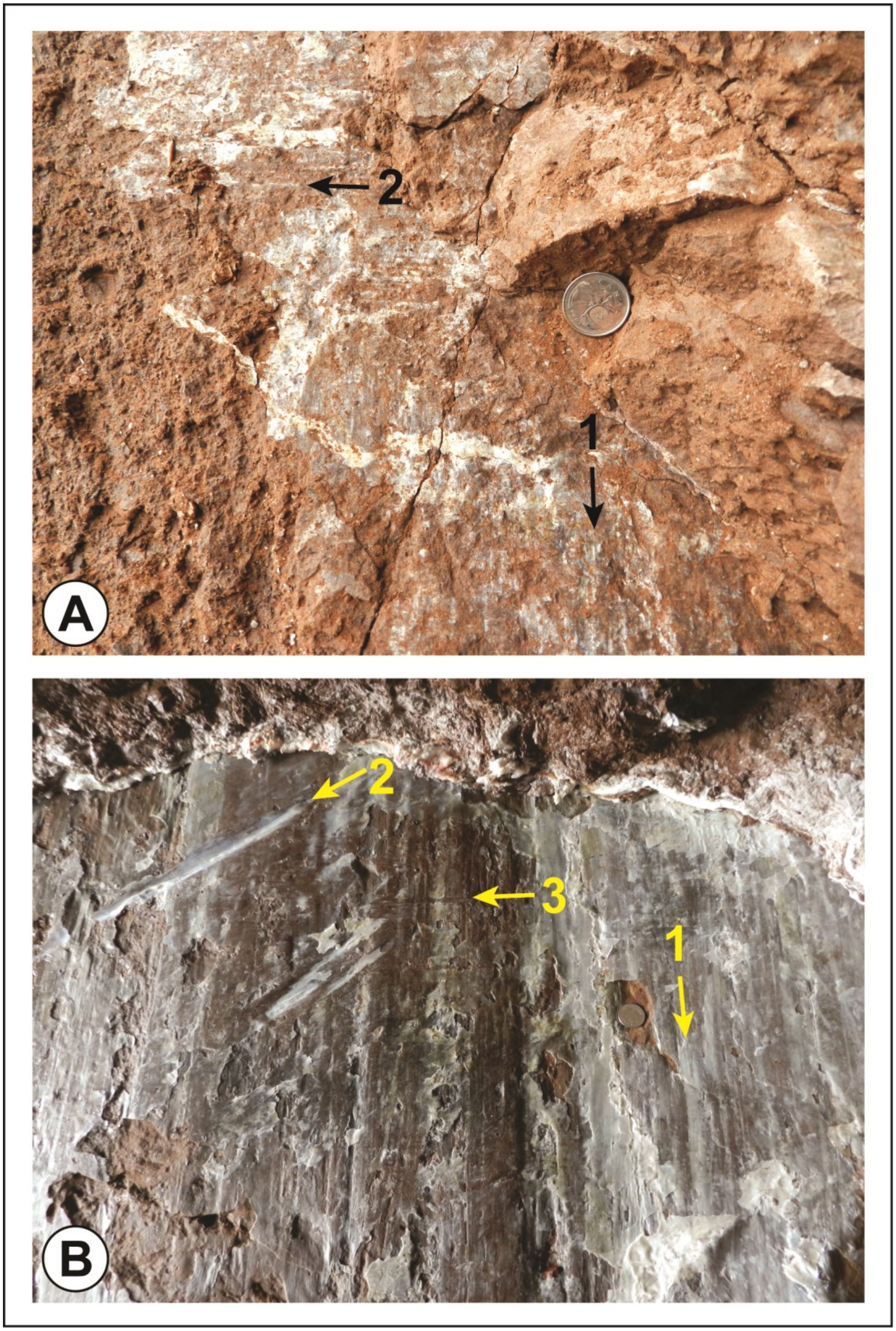

Figure 20. Examples of A) two and B) three sets of overprinting slickenlines at Blue Sac (movement direction of the hanging wall indicated by arrows). The numbers indicate the relative age, where 1 is the oldest and higher values are younger.

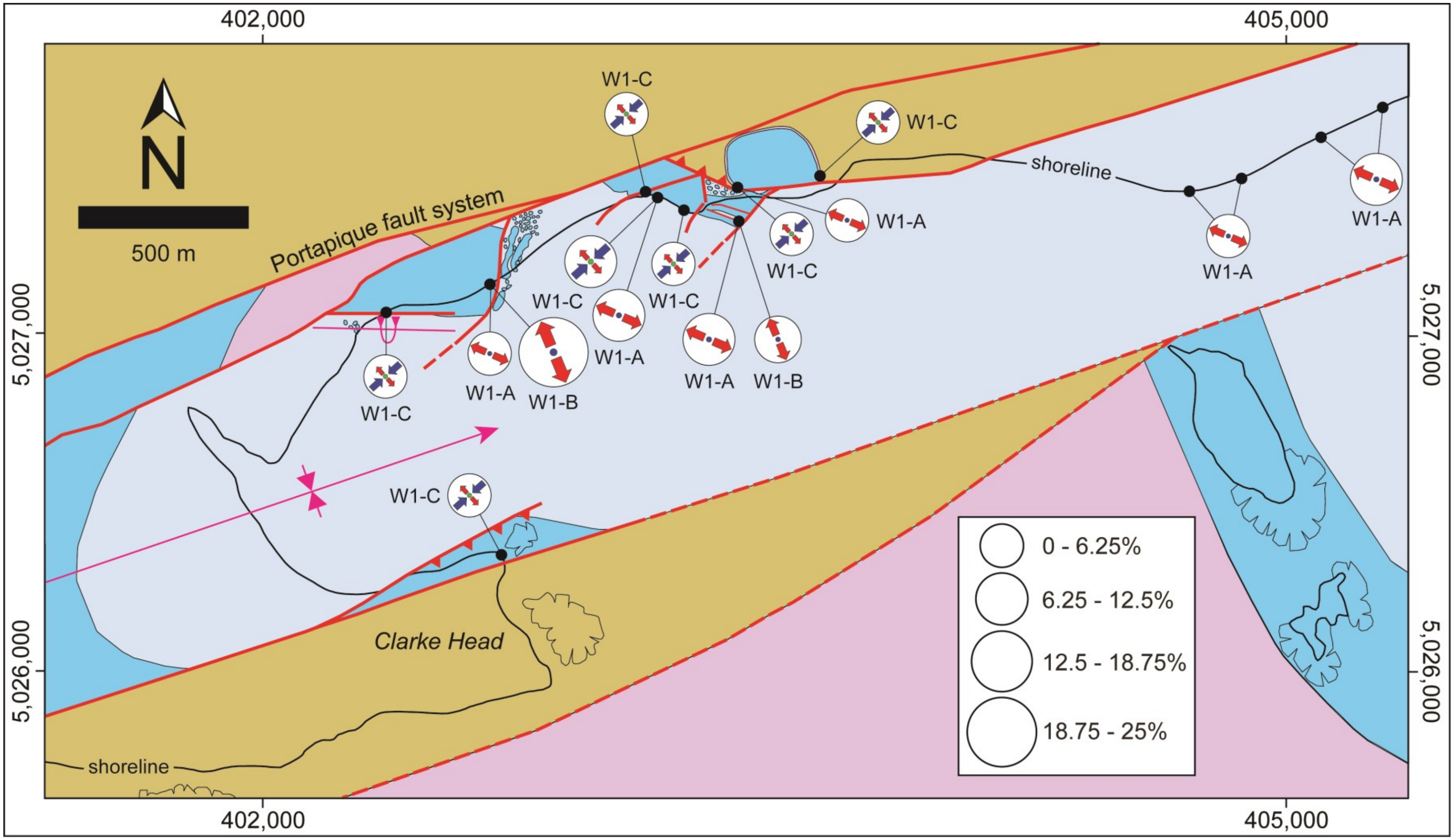

Figure 21. Geologic map of Wasson Bluff (modified from Withjack et al., 2010) showing the spatial distribution of stress states, assuming fracture formation and/or reactivation occurred after tilting (scenario 1). Percentages are based on the number of fractures contained in the stress states at each subsite relative to the total of fractures in the area (see Appendices 12 to 14). See Figure 4 for color scheme, and Appendix 12 for symbols.

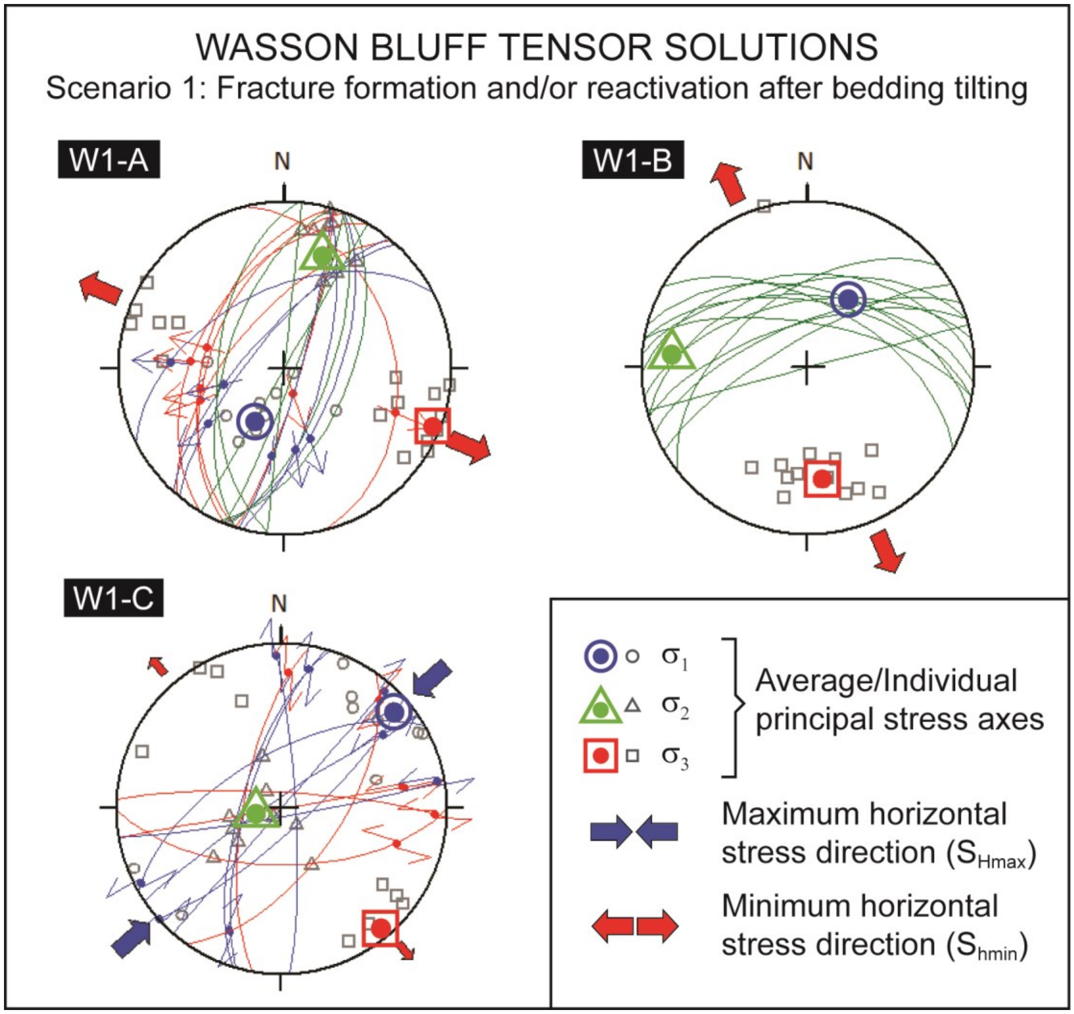

Figure 22. Reduced stress tensors and equal-area stereographic projections of fractures at Wasson Bluff assuming fracture formation and/or reactivation after bedding tilting (i.e., fractures used in stress inversion are in the present-day orientation; see Appendices 12 to 14). The solution yields three distinct stress states (A to C). See Figure 5 for color scheme of fractures.

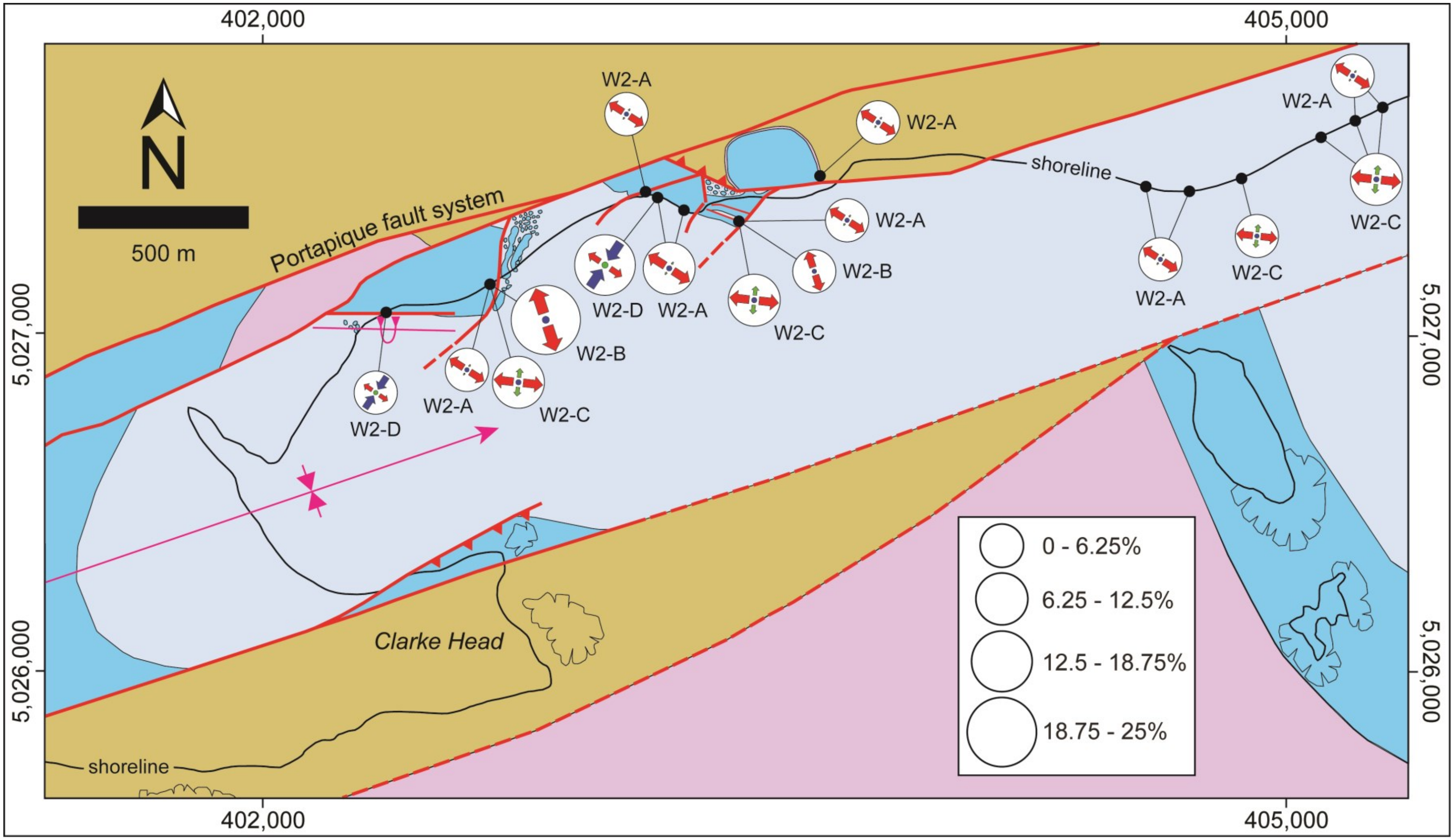

Figure 23. Geologic map of Wasson Bluff (modified from Withjack et al., 2010) showing the spatial distribution of stress states, assuming fracture formation and/or reactivation occurred before tilting (scenario 2). Percentages are based on the number of fractures contained in the stress states at each subsite relative to the total of fractures in the area (see Appendices 12, 13 and 15). See Figure 4 for color scheme, and Appendix 12 for symbols and bedding information.

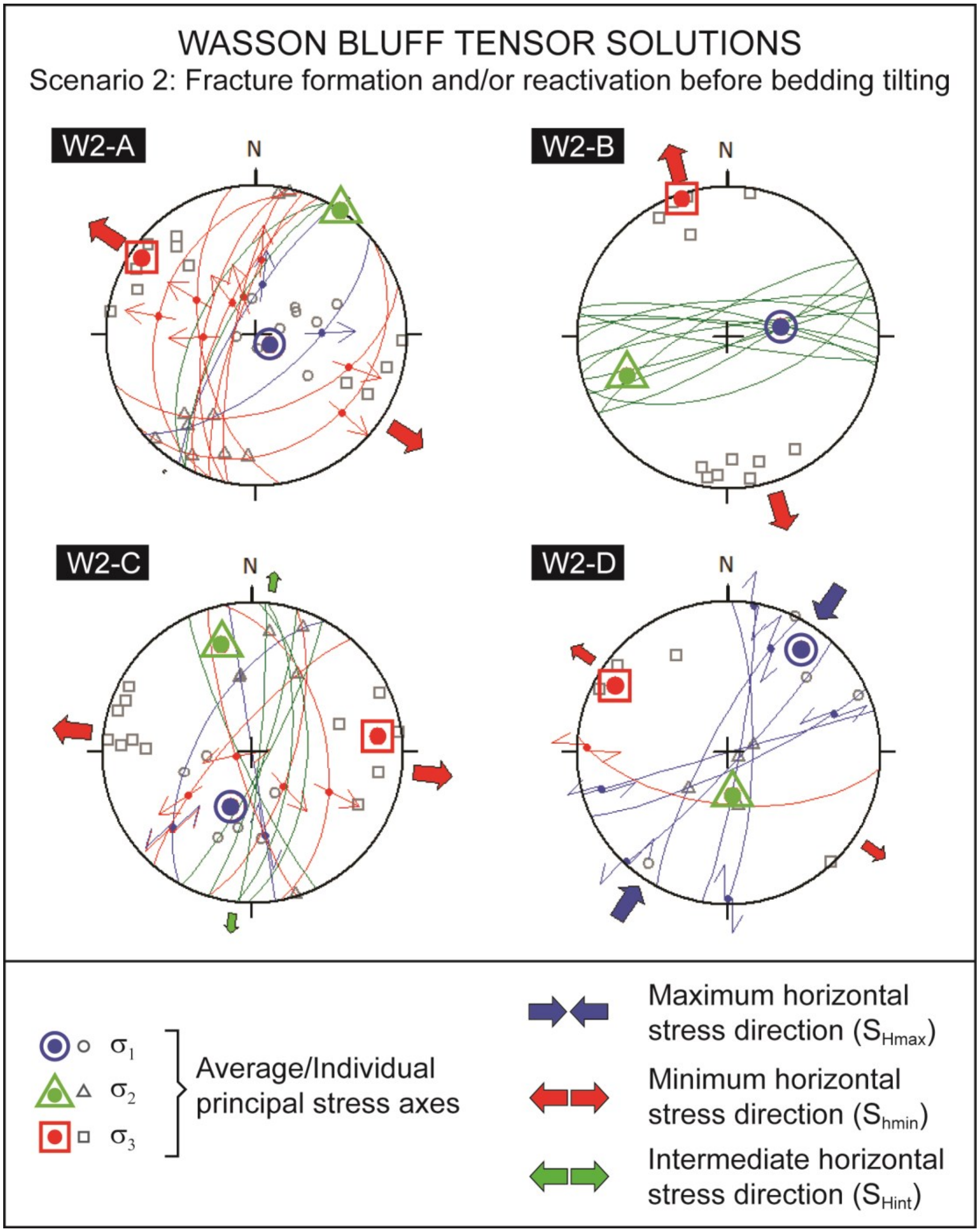

Figure 24. Reduced stress tensors and equal-area stereographic projections of fractures at Wasson Bluff assuming fracture formation and/or reactivation before bedding tilting (i.e., fractures used in stress inversion are corrected for local bedding; see Appendices 12, 13 and 15). The solution yields four distinct stress states (A to D). See Figure 5 for color scheme of fractures.

Figure 25. Example of cross-cutting relationships at Wasson Bluff. Quartz-filled tension fractures cut across mudstone-filled tension fractures.

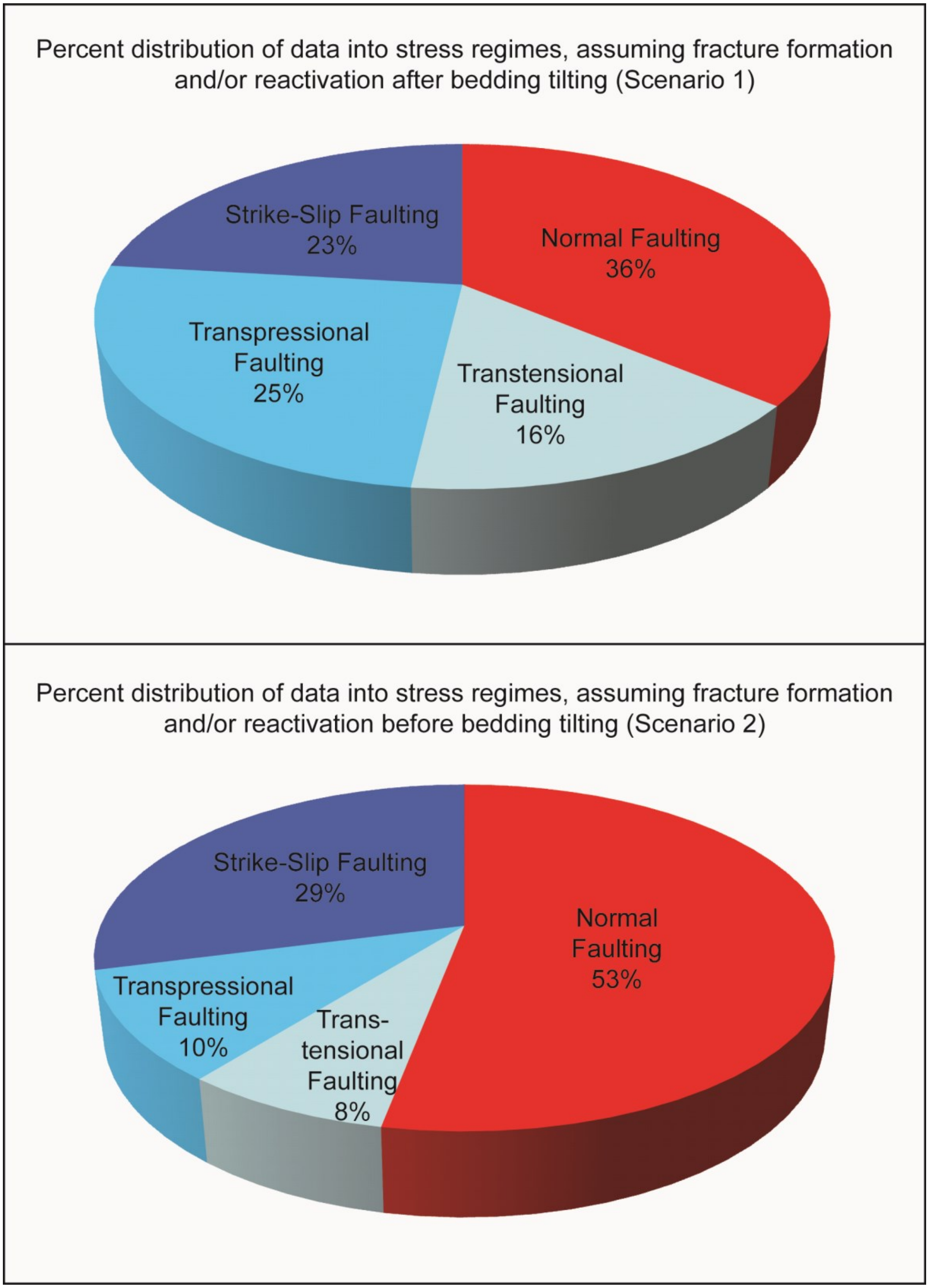

Figure 26. Percent distribution of all data into stress regimes obtained from the stress inversion. The results from Economy Point, which has only one scenario, are repeated in both graphs.

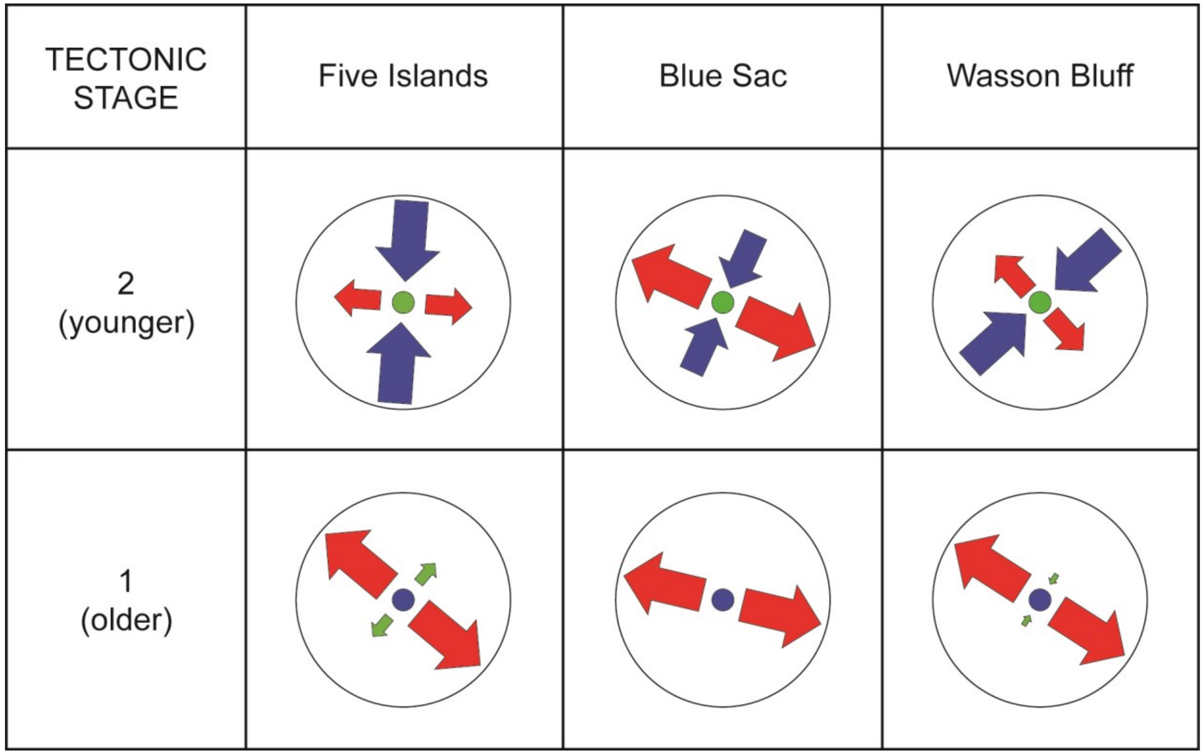

Figure 27. Relative timing of representative stress states grouped in two possible tectonic phases. See Tables 6 and 9 for more details.

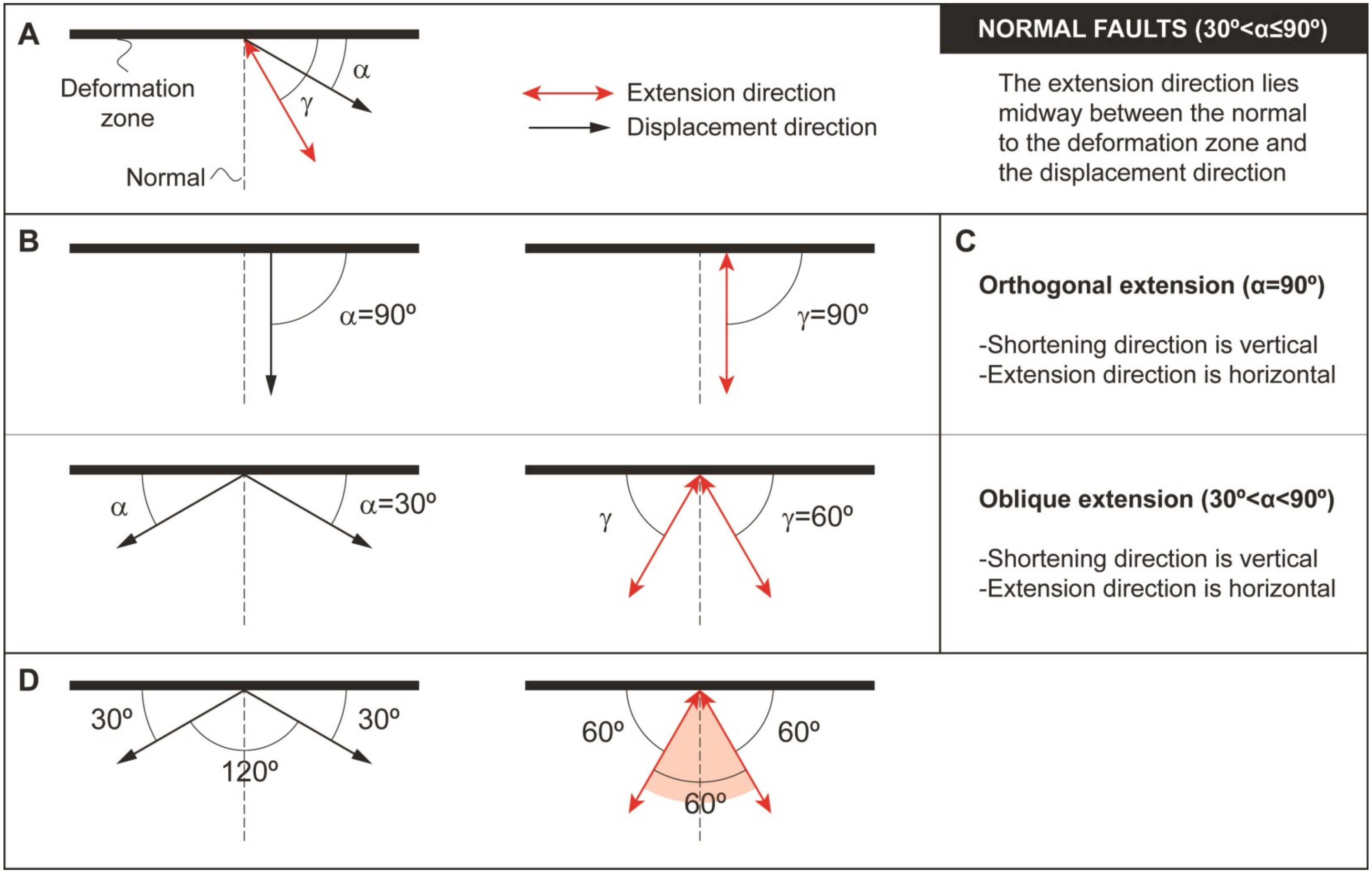

Figure 28. Relationship between strain and displacement during rifting. Normal faulting occurs when the angle between the displacement direction and the deformation zone (α) ranges from 90º to 30º (see Withjack & Jamison, 1986). A) Definition of key features. B) Relationship for two key displacement directions (α=90º, α=30º). C) Definition of key strain states. D) Range of possible displacement and infinitesimal extension directions that yield normal faulting for orthogonal and oblique extension.

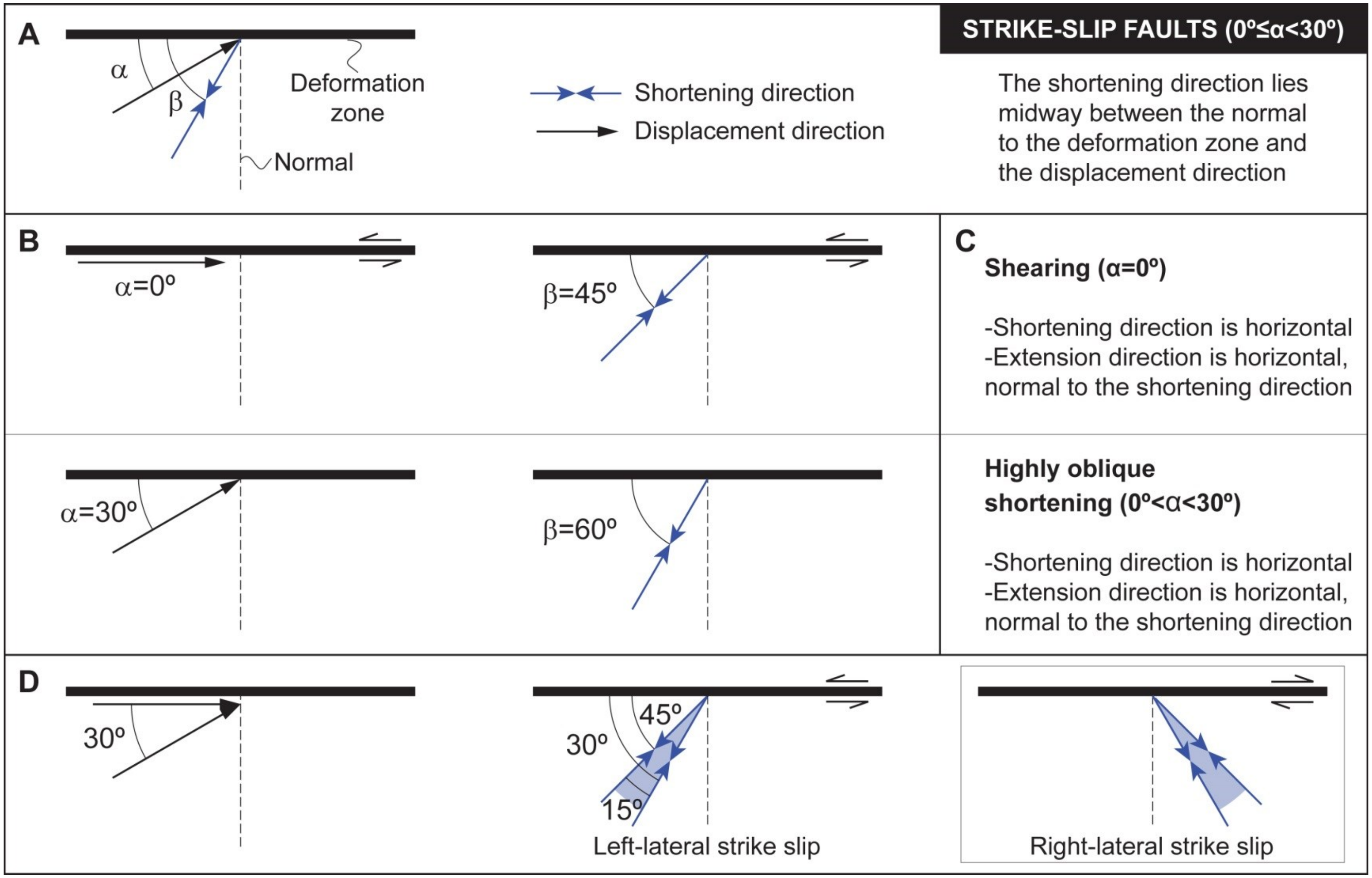

Figure 29. Relationship between strain and displacement during shearing and oblique shortening. Strike-slip faulting occurs when the angle between the displacement direction and the deformation zone (α) ranges from 0º to 30º (see Withjack & Jamison, 1986). A) Definition of key features. B) Relationship for two key displacement directions (α=0º, α=30º) that produce left-lateral strike-slip faults. Displacement directions in the opposite quadrant produce right-lateral strike-slip faults. C) Definition of key strain states. D) Range of displacement and possible infinitesimal extension directions for shearing and highly oblique shortening.

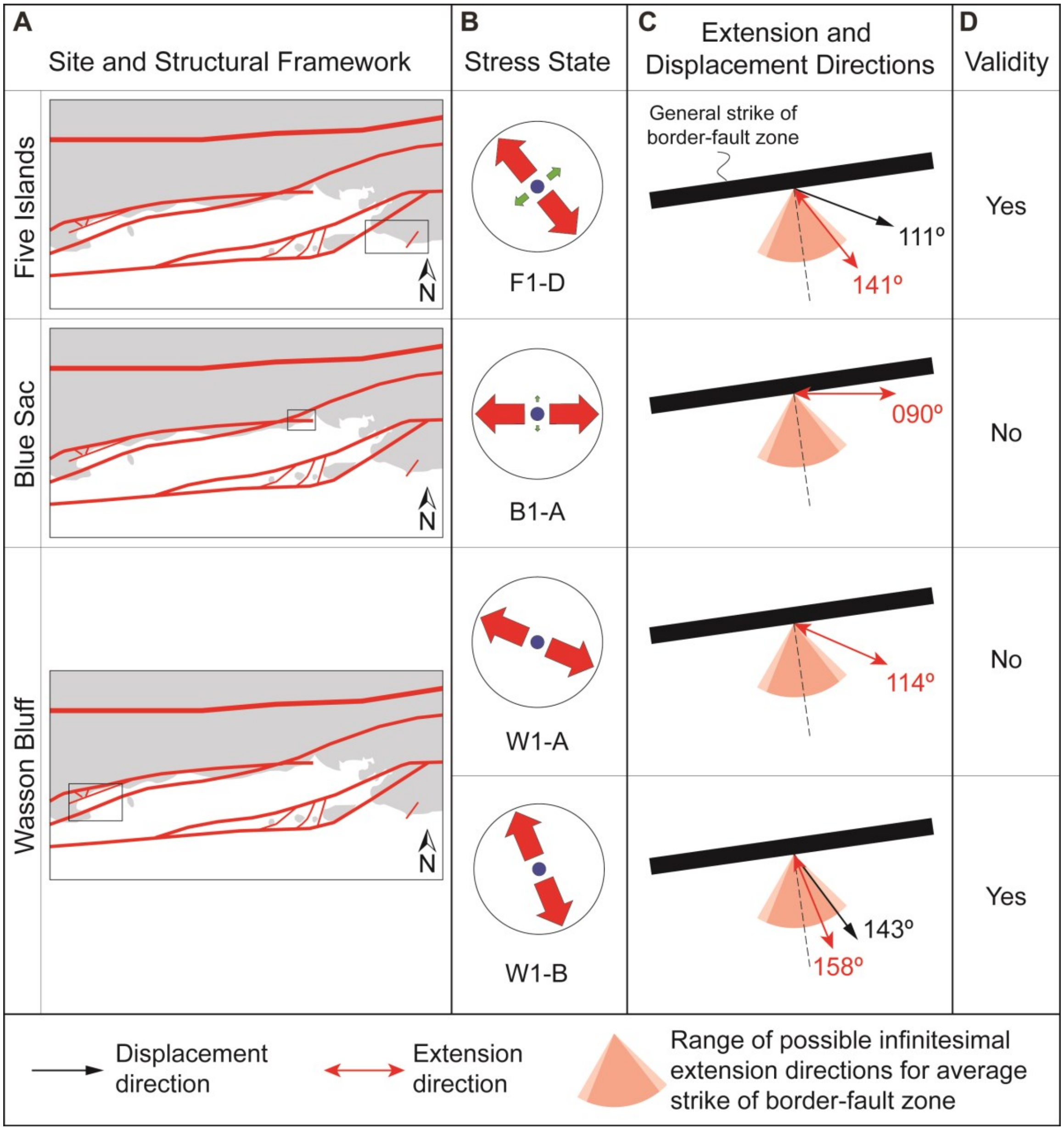

Figure 30. Inferred displacement directions of the hanging wall (southern border-fault block) during the regional normal-faulting regime assuming that faulting occurred after tilting of bedding. A) Location of field site relative to the border-fault zone. B) Stress state based on stress inversion. C) Extension direction (parallel to S_{hmin}) and inferred displacement directions (only shown if the extension direction falls within the possible range of infinitesimal directions). The strike of the border-fault zone ranges between E and ENE; therefore, the possible ranges of infinitesimal extension directions for the two end members overlap in the figure. D) Validity of the analysis. 'Yes' indicates that the inferred extension direction falls within the acceptable range for normal faulting.

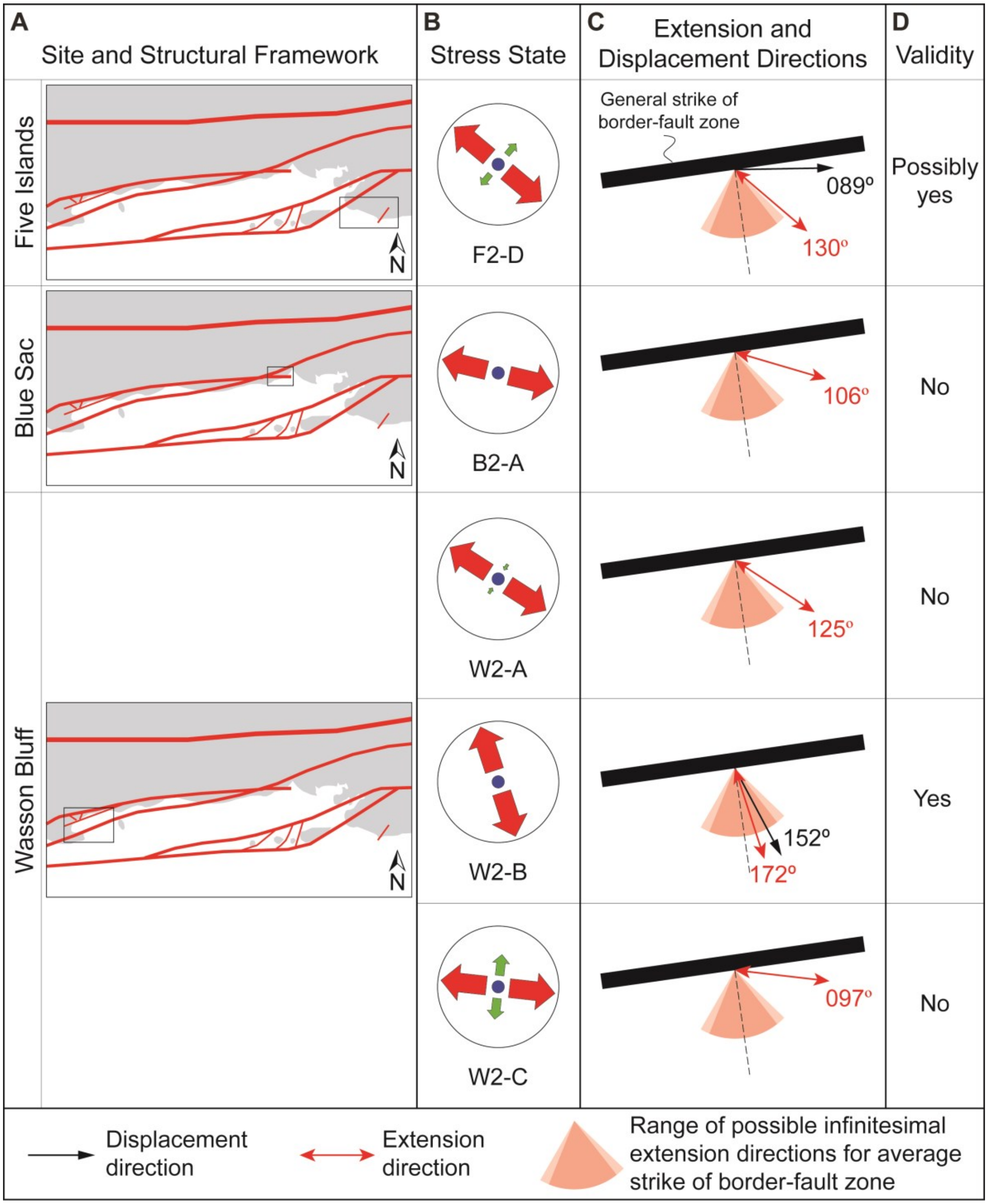

Figure 31. Inferred displacement directions of the hanging wall (southern border-fault block) during the regional normal-faulting regime assuming that faulting occurred before tilting of bedding. A) Location of field site relative to the border-fault zone. B) Stress state based on stress inversion. C) Extension direction (parallel to S_{hmin}) and inferred displacement directions (only shown if the extension direction falls within the possible range of infinitesimal directions). The strike of the border-fault zone ranges between E and ENE; therefore, the possible ranges of infinitesimal extension directions for the two end members overlap in the figure. D) Validity of the analysis. 'Yes' indicates that the inferred extension direction falls within the acceptable range for normal faulting.

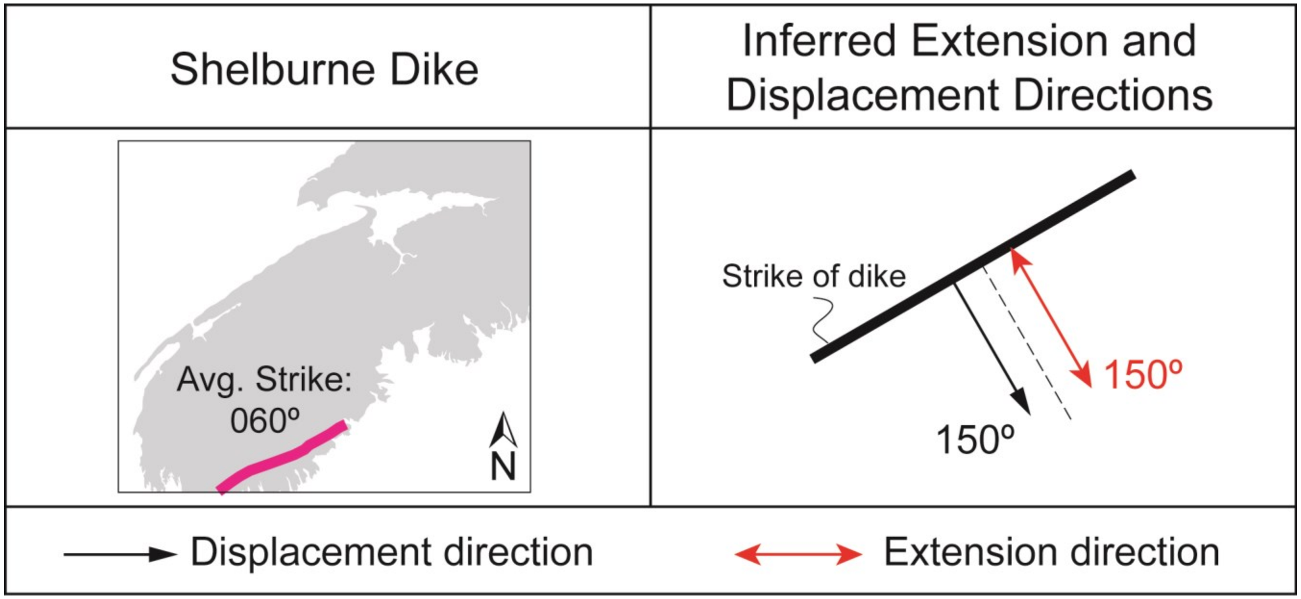

Figure 32. Inferred extension and displacement directions in the Shelburne dike during the intrusion at approximately 200 Ma (Dunn et al., 1998).

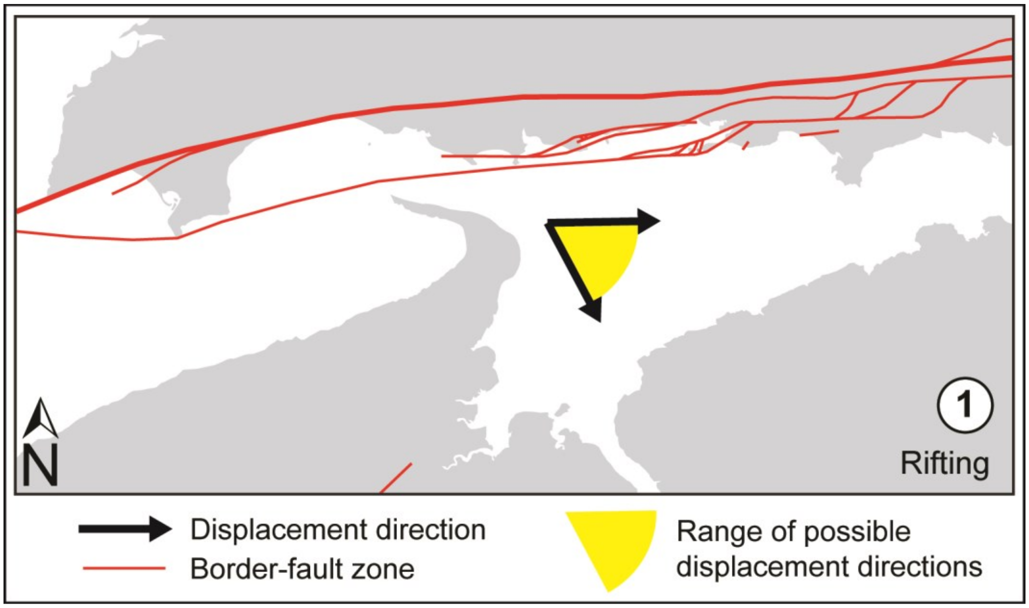

Figure 33. Range of possible displacement directions during tectonic stage 1 (rifting) based on valid extension directions. As indicated by the range, the average movement of the hanging wall (southern border-fault block) relative to the footwall is SE.

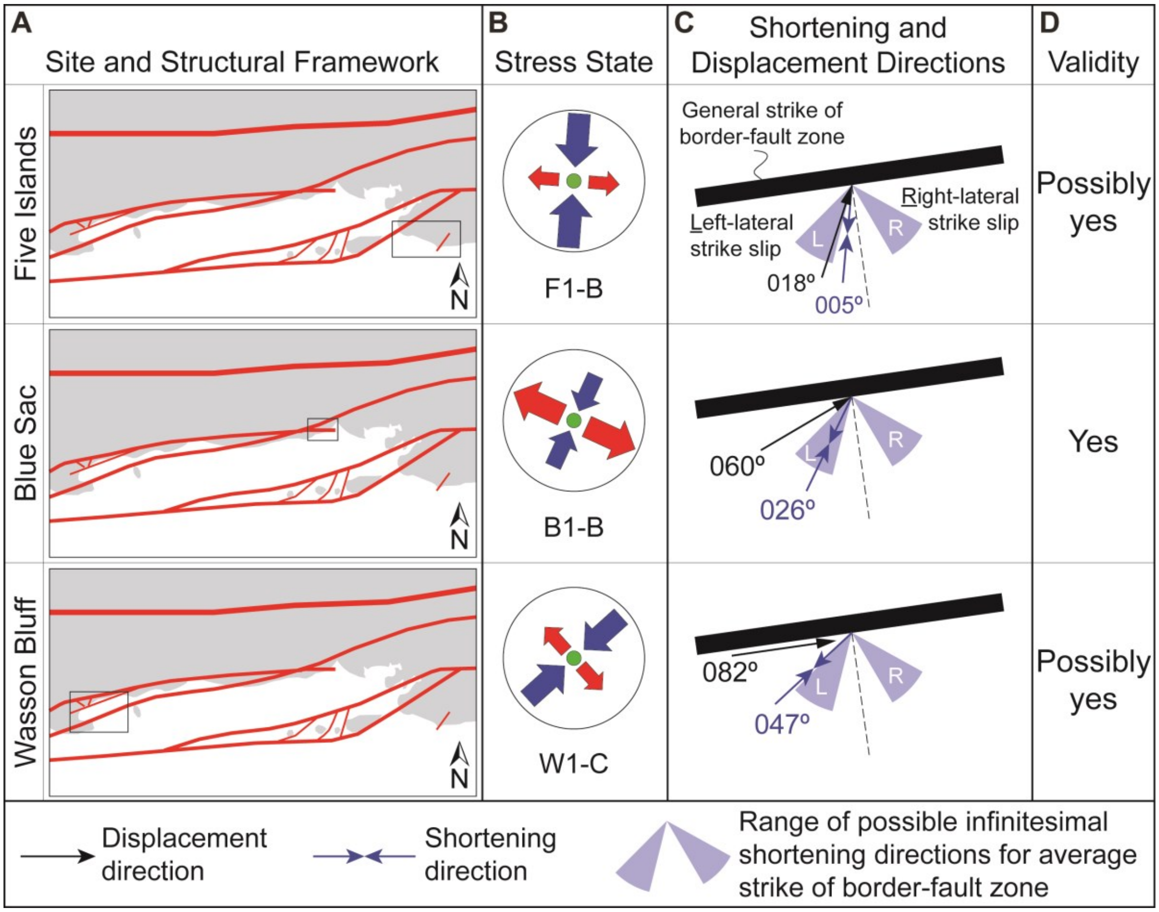

Figure 34. Inferred displacement directions of the hanging wall (southern border-fault block) during the regional strike-slip-faulting regime assuming that faulting occurred after tilting of bedding. A) Location of field site relative to the border-fault zone. B) Stress state based on stress inversion. C) Shortening direction (parallel to S_{Hmax}) and inferred displacement directions (only shown if the shortening direction falls within the possible range of infinitesimal directions). The strike of the border-fault zone ranges between E and ENE; therefore, the possible ranges of infinitesimal shortening directions for the two end members are merged and form larger arcs in the figure. D) Validity of the analysis. 'Yes' indicates that the inferred shortening direction falls within the acceptable range for strike-slip faulting.

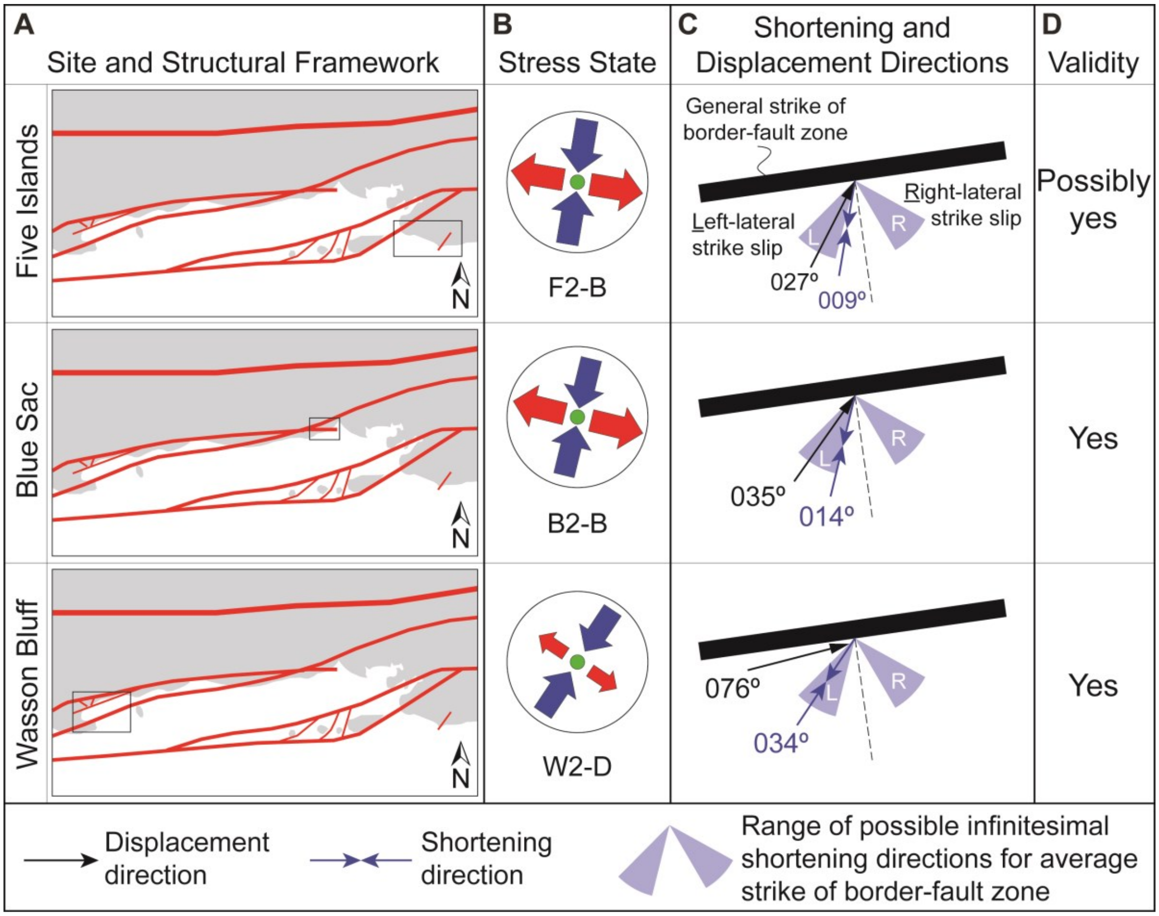

Figure 35. Inferred displacement directions of the hanging wall (southern border-fault block) during the regional strike-slip-faulting regime assuming that faulting occurred before tilting of bedding. A) Location of field site relative to the border-fault zone. B) Stress state based on stress inversion. C) Shortening direction (parallel to S_{Hmax}) and inferred displacement directions (only shown if the shortening direction falls within the possible range of infinitesimal directions). The strike of the border-fault zone ranges between E and ENE; therefore, the possible ranges of infinitesimal shortening directions for the two end members are merged and form larger arcs in the figure. D) Validity of the analysis. 'Yes' indicates that the inferred shortening direction falls within the acceptable range for strike-slip faulting.

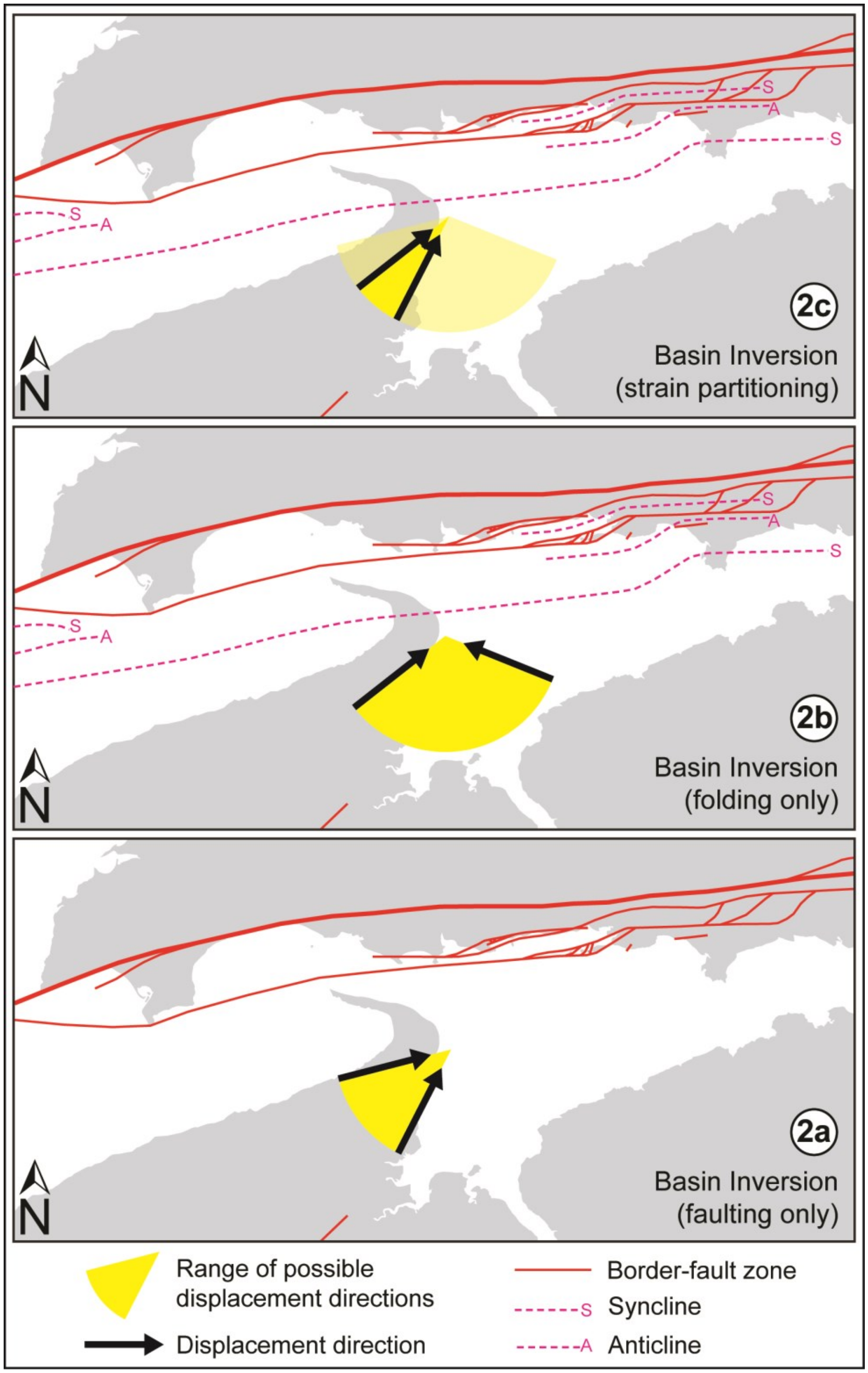

Figure 36. Range of possible displacement directions during tectonic stage 2 (basin inversion) based on valid shortening directions. As suggested by the range, the average movement on the hanging wall (southern border-fault block) relative to the footwall is a) to the NE if only faulting occurred, b) to the north if only folding occurred (folds form when $30<\beta\leq 90$), or c) to the NE if faulting and folding are coeval, and strain partitioning occurred.

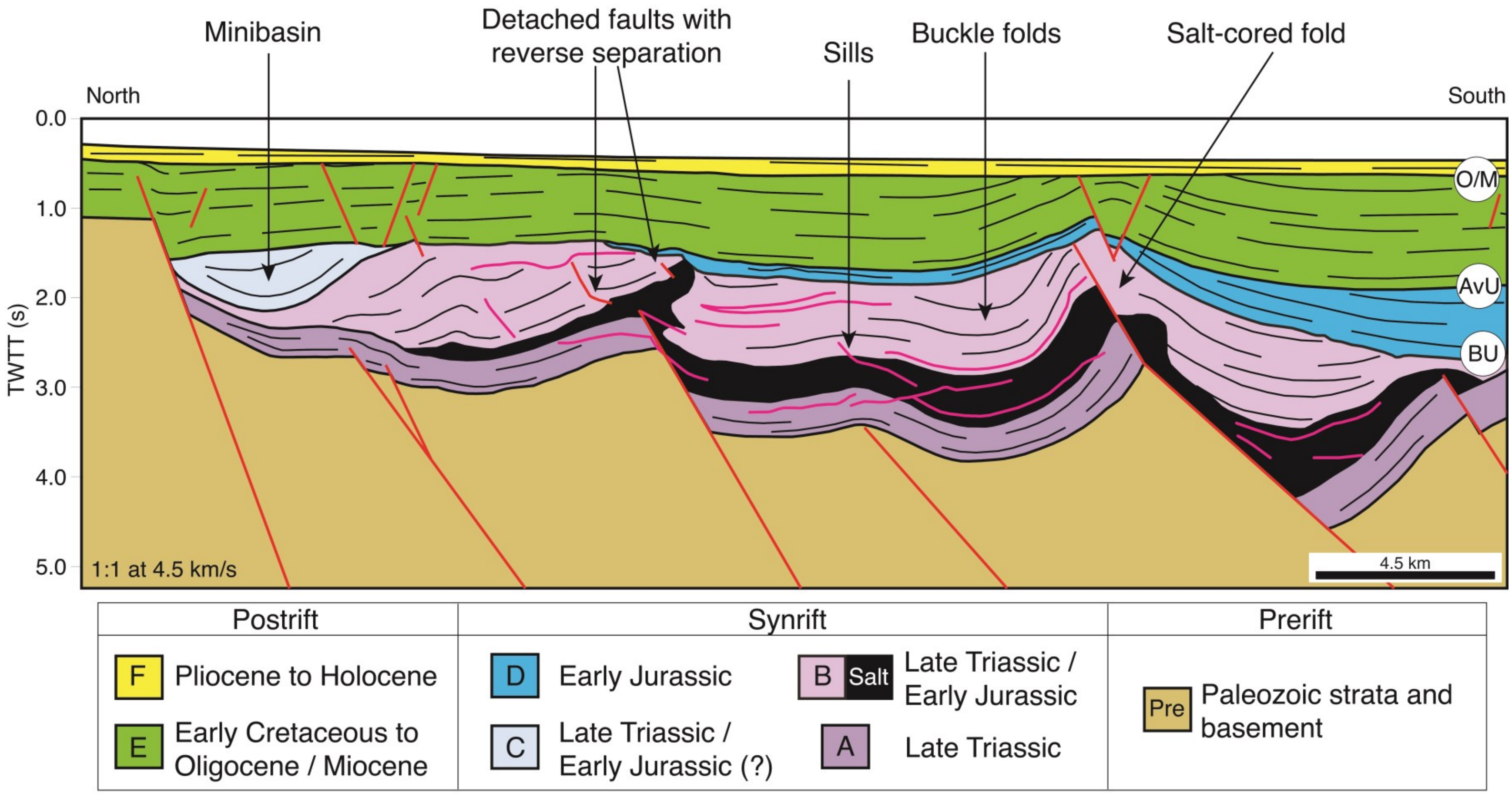

Figure 37. Illustration of an interpreted seismic line from the Orpheus (synrift) and Scotian (postrift) basins showing synrift and postrift deformation of seven tectonostratigraphic packages. Three major unconformities (BU: Early Jurassic 'breakup unconformity'; AvU: Early Cretaceous 'Avalon unconformity'; O/M: Oligocene/Miocene unconformity) are present. The nomenclature of each tectonostratigraphic package is the same as in Figure 35 and includes the prerift unit. Redrafted from Syamsir (2010) and Hanafi (2013).

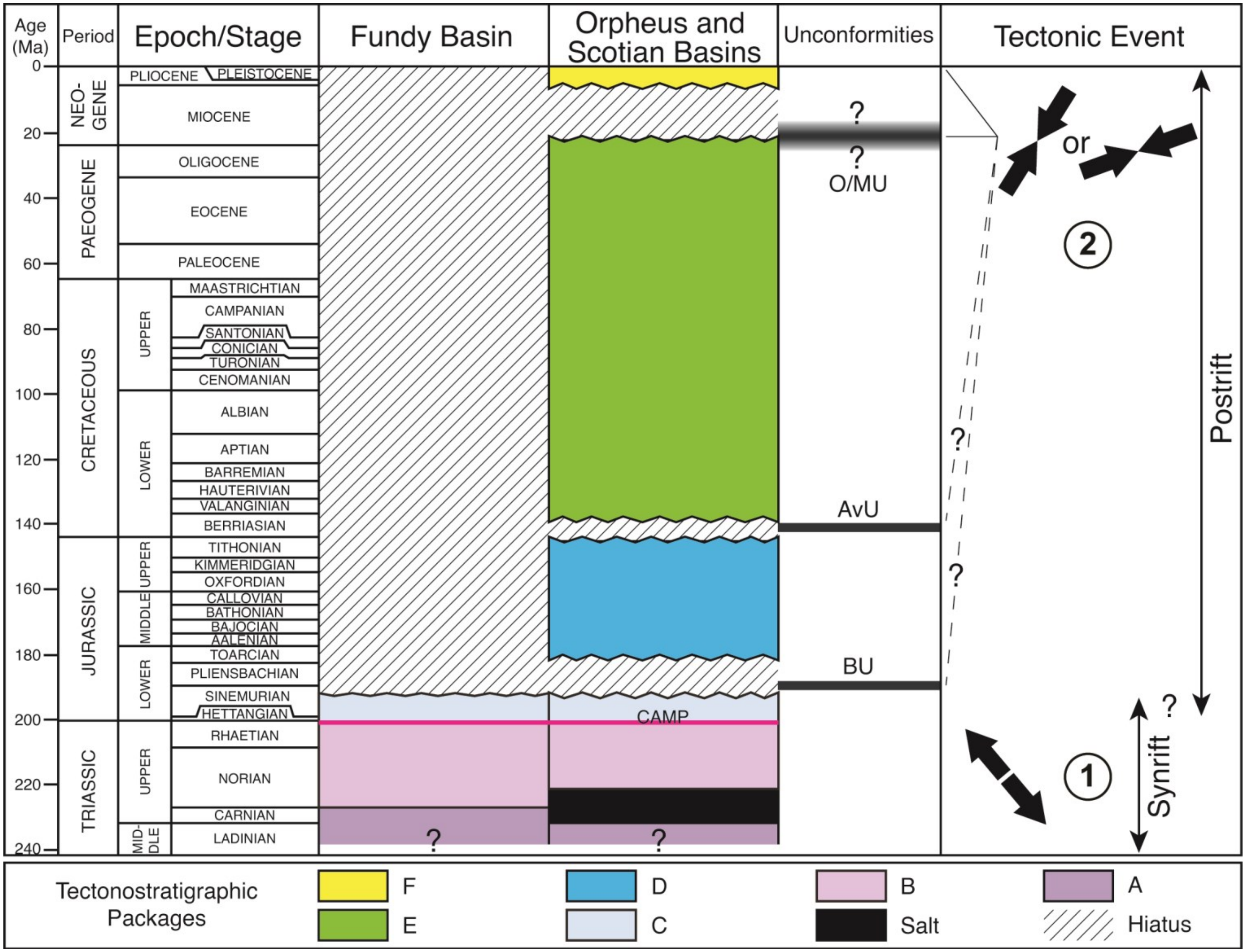

Age (Ma)
Period
Epoch/Stage
Fundy Basin
Orpheus and Scotian Basins
Unconformities
Tectonic Event
0
20
40
60
80
100
120
140
160
180
200
220
240
NEO-GENE
PAEOGENE
CRETACEOUS
JURASSIC
TRIASSIC
UPPER
LOWER
MIDDLE
MID-DLE
PLIOCENE
PLEISTOCENE
MIOCENE
OLIGOCENE
EOCENE
PALEOCENE
MAASTRICHTIAN
CAMPANIAN
SANTONIAN
CONICIAN
TURONIAN
CENOMANIAN
ALBIAN
APTIAN
BARREMIAN
HAUTERIVIAN
VALANGINIAN
BERRIASIAN
TITHONIAN
KIMMERIDGIAN
OXFORDIAN
CALLOVIAN
BATHONIAN
BAJOCIAN
AALENIAN
TOARCIAN
PLIENSBACHIAN
SINEMURIAN
HETTANGIAN
RHAETIAN
NORIAN
CARNIAN
LADINIAN
CAMP
?
O/MU
AvU
BU
or
2
1
Postrift
Synrift
Tectonostratigraphic Packages
F
E
D
C
B
Salt
A
Hiatus

Figure 38 (On previous page). Simplified stratigraphic columns (modified from Weston et al., 2012) and correlation of generalized tectonic phases from the onshore Fundy basin with events of uplift and erosion from the offshore Orpheus and Scotian basins (modified from Hanafi, 2013; see Figure 34). Rifting ended in the Early Jurassic. The postrift event possibly is late Oligocene-Miocene to the present day. CAMP: Central Atlantic Magmatic Province; BU: breakup unconformity; AvU: Avalon Unconformity; O/MU: late Oligocene-Miocene unconformity.

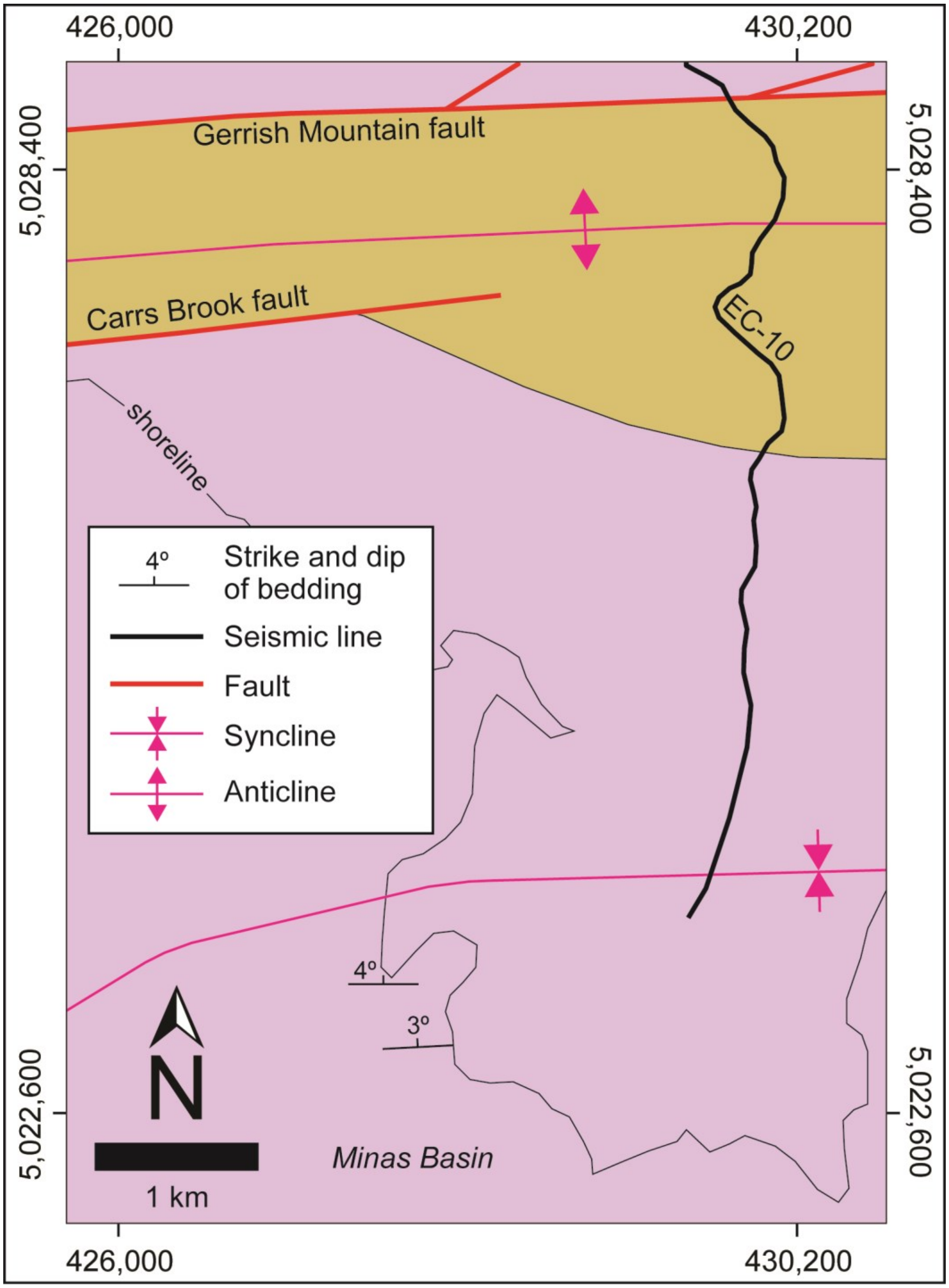

A1. Geologic map of the western part of Economy Point (modified from Donohoe & Wallace, 1982). Because the sampling area is near the trough of the syncline, the bedding is nearly horizontal and no bedding correction is necessary for the fractures. The purple unit could be either Wolfville or lower Blomidon Formations. See Figure 3 for full extension of seismic line EC-10 and Figure 4 for color scheme.

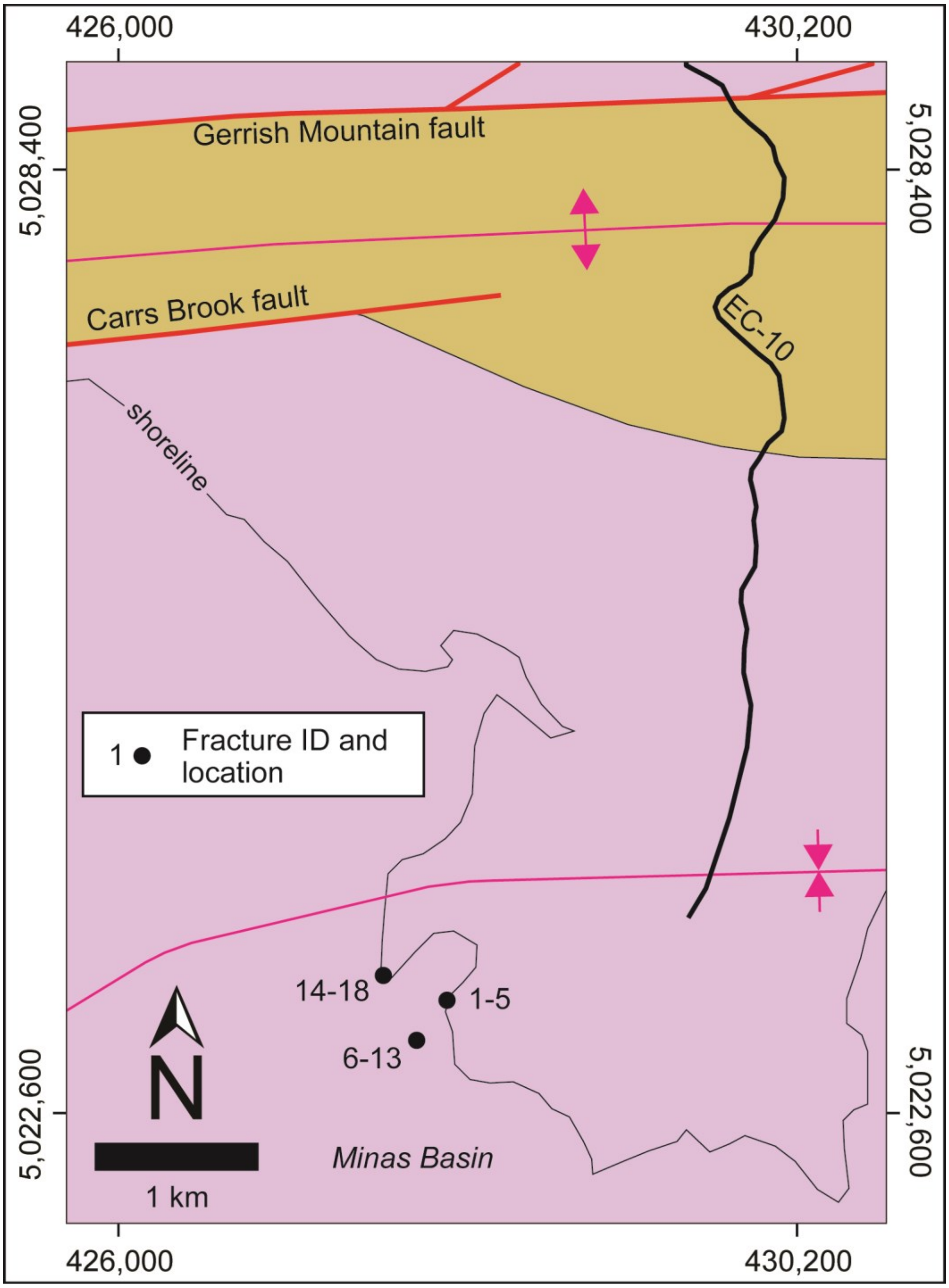

A2. Geologic map of the western part of Economy Point (modified from Donohoe & Wallace, 1982) and location of fractures listed in Appendix 3. See Figure 4 for color scheme, and Appendix 1 for symbols and bedding information.

A3. Fractures measured at Economy Point used for stress inversion.

Fracture ID	*Type of fracture*	*Plane*		*Slickenline*		*Sense*[a]
		Dip direction (°)	*Dip angle (°)*	*Trend (°)*	*Plunge(°)*	
1	Tension fracture	057	80	-	-	-
2	Tension fracture	064	90	-	-	-
3	Tension fracture	246	86	-	-	-
4	Tension fracture	261	88	-	-	-
5	Tension fracture	235	89	-	-	-
6	Conjugate fault	245	81	156	09	L
7	Conjugate fault	020	90	110	13	R
8	Conjugate fault	245	80	156	04	L
9	Conjugate fault	355	90	085	11	R
10	Conjugate fault	006	83	094	16	R
11	Conjugate fault	245	79	158	14	L
12	Conjugate fault	245	81	157	14	L
13	Conjugate fault	352	79	080	12	R
14	Tension fracture	250	86	-	-	-
15	Tension fracture	070	90	-	-	-
16	Conjugate fault	207	90	297	05	R
17	Conjugate fault	065	87	335	04	L
18	Tension fracture	040	85	-	-	-

[a] *L: left-lateral strike slip; R: right-lateral strike slip*

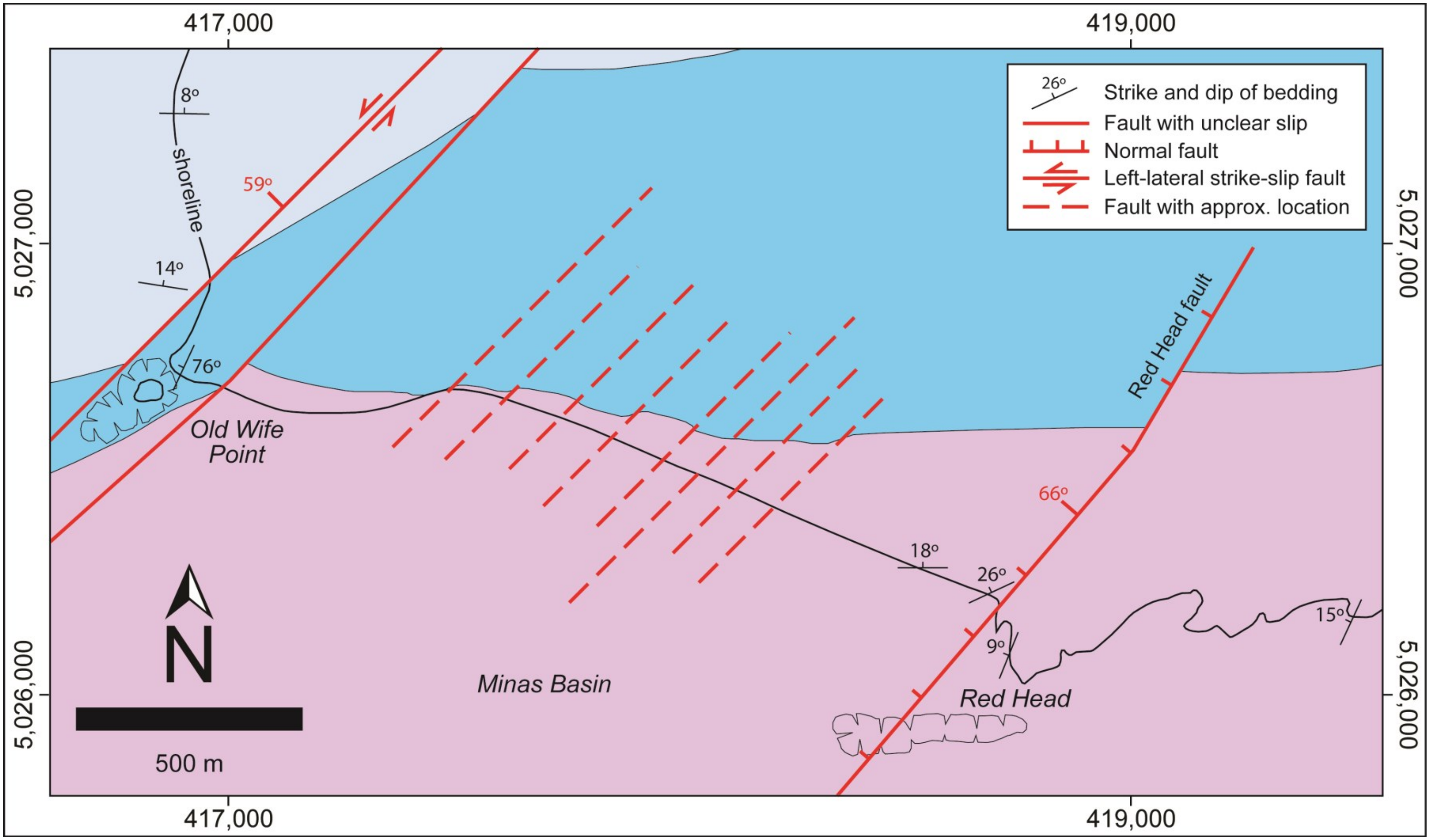

A4. Geologic map of Five Islands (modified from Withjack et al., 2009). See Figure 4 for color scheme.

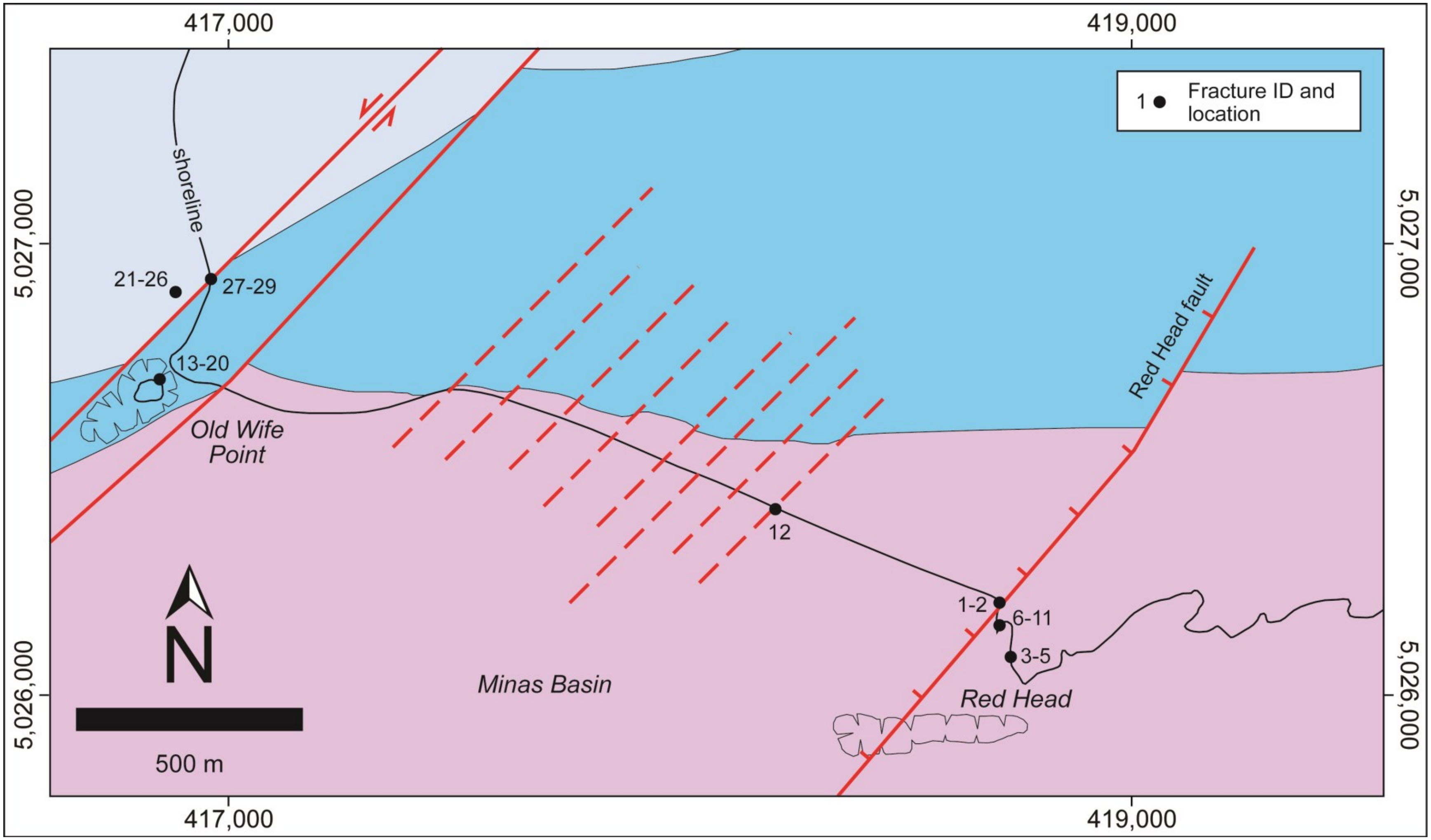

A5. Geologic map of Five Islands (modified from Withjack et al., 2009) and location of fractures listed in Appendices 6 and 7. See Figure 4 for color scheme, and Appendix 4 for symbols and bedding information.

A6. Fractures measured at Five Islands and used for stress inversion assuming fracture formation and/or reactivation after bedding rotation (Scenario 1).

Fracture ID	*Type of fracture*	*Plane*		*Slickenline*		*Sense*[a]	*Stress state*
		Dip direction (°)	*Dip angle (°)*	*Trend (°)*	*Plunge(°)*		
1	Fault	134	27	120	26	N	F1-D
2	Fault	307	66	336	63	N	F1-D
3	Fault	000	83	341	83	N	F1-A
4	Fault	353	70	020	68	N	F1-A
5	Fault	355	84	325	84	N	F1-A
6	Conjugate fault	355	90	085	57	N	F1-A
7	Conjugate fault	190	68	128	49	N	F1-A
8	Conjugate fault	355	90	085	62	N	F1-A
9	Conjugate fault	190	64	136	50	N	F1-A
10	Conjugate fault	350	80	066	54	N	F1-A
11	Conjugate fault	190	71	124	50	N	F1-A
12	Fault	312	77	260	69	N	F1-D
13	Conjugate fault	295	78	018	31	L	F1-B
14	Conjugate fault	260	62	341	17	R	F1-B
15	Conjugate fault	061	82	332	07	L	F1-C
16	Conjugate fault	013	90	283	11	R	F1-C
17	Conjugate fault	070	77	342	09	L	F1-C
18	Conjugate fault	190	88	279	16	R	F1-C
19	Conjugate fault	045	74	324	29	L	F1-C
20	Conjugate fault	174	74	255	29	R	F1-C
21	Conjugate fault	160	66	077	16	L	F1-B
22	Conjugate fault	270	80	355	27	R	F1-B
23	Conjugate fault	164	76	079	19	L	F1-B
24	Conjugate fault	269	74	354	17	R	F1-B
25	Conjugate fault	166	82	079	19	L	F1-B
26	Conjugate fault	264	72	351	10	R	F1-B

[a] *N: normal; L: left-lateral strike slip; R: right-lateral strike slip*

Continues on next page

A6 (continued from previous page). Fractures measured at Five Islands and used for stress inversion assuming fracture formation and/or reactivation after bedding rotation (Scenario 1).

Fracture ID	*Type of fracture*	*Plane*		*Slickenline*		*Sense*[a]	*Stress state*
		Dip direction (°)	*Dip angle (°)*	*Trend (°)*	*Plunge(°)*		
27	Fault	144	63	226	14	R	F1-C
28	Fault	144	63	057	06	L	F1-B
29	Fault	112	73	026	13	L	F1-B

[a] *L: left-lateral strike slip; R: right-lateral strike slip*

A7. Fractures from Five Islands assuming formation and/or reactivation before the rotation of a nearby reference bedding plane (Scenario 2).

Fracture ID	*Type of fracture*	*Plane*		*Slickenline*		*Sense*[a]	*Stress state*	*Reference bedding*
		Dip direction (º)	*Dip angle (º)*	*Trend (º)*	*Plunge(º)*			
1	Fault	143	52	107	46	N	F2-D	335º/26º
2	Fault	297	44	336	37	N	F2-D	335º/26º
3	Fault	001	80	313	75	N	F2-A	292º/09º
4	Fault	356	66	359	66	N	F2-A	292º/09º
5	Fault	356	80	308	76	N	F2-A	292º/09º
6	Conjugate fault	355	86	077	65	N	F2-A	292º/09º
7	Conjugate fault	187	70	132	58	N	F2-A	292º/09º
8	Conjugate fault	355	86	074	70	N	F2-A	292º/09º
9	Conjugate fault	186	66	142	58	N	F2-A	292º/09º
10	Conjugate fault	352	75	055	60	N	F2-A	292º/09º
11	Conjugate fault	187	73	127	59	N	F2-A	292º/09º
12	Fault	307	66	303	65	N	F2-D	000º/18º
13	Conjugate fault	295	08	354	01	T	-	295º/76º
14	Conjugate fault	176	35	172	35	T	-	295º/76º
15	Conjugate fault	224	58	178	48	N	F2-C	295º/76º
16	Conjugate fault	022	78	089	62	N	F2-C	295º/76º
17	Conjugate fault	234	52	181	38	N	F2-C	295º/76º
18	Conjugate fault	019	76	087	56	N	F2-C	295º/76º
19	Conjugate fault	226	75	148	39	L	F2-C	295º/76º
20	Conjugate fault	360	66	073	32	R	F2-C	295º/76º
21	Conjugate fault	162	78	074	10	L	F2-B	009º/14º
22	Conjugate fault	268	82	356	13	R	F2-B	009º/14º
23	Conjugate fault	165	89	075	14	L	F2-B	009º/14º
24	Conjugate fault	265	77	355	03	R	F2-B	009º/14º
25	Conjugate fault	346	85	075	14	L	F2-B	009º/14º
26	Conjugate fault	260	76	171	03	R	F2-B	009º/14º

[a] *N: normal; T: thrust/reverse; L: left-lateral strike slip; R: right-lateral strike slip*

Continues on next page

A7 (continued from previous page). Fractures from Five Islands assuming formation and/or reactivation before the rotation of a nearby reference bedding plane (Scenario 2).

Fracture ID	*Type of fracture*	*Plane*		*Slickenline*		*Sense*[a]	*Stress state*	*Reference bedding*
		Dip direction (º)	*Dip angle (º)*	*Trend (º)*	*Plunge(º)*			
27	Fault	148	73	229	25	R	-	009º/14º
28	Fault	148	73	237	03	L	F2-B	009º/14º
29	Fault	116	77	206	00	L	F2-B	009º/14º

[a] *L: left-lateral strike slip; R: right-lateral strike slip*

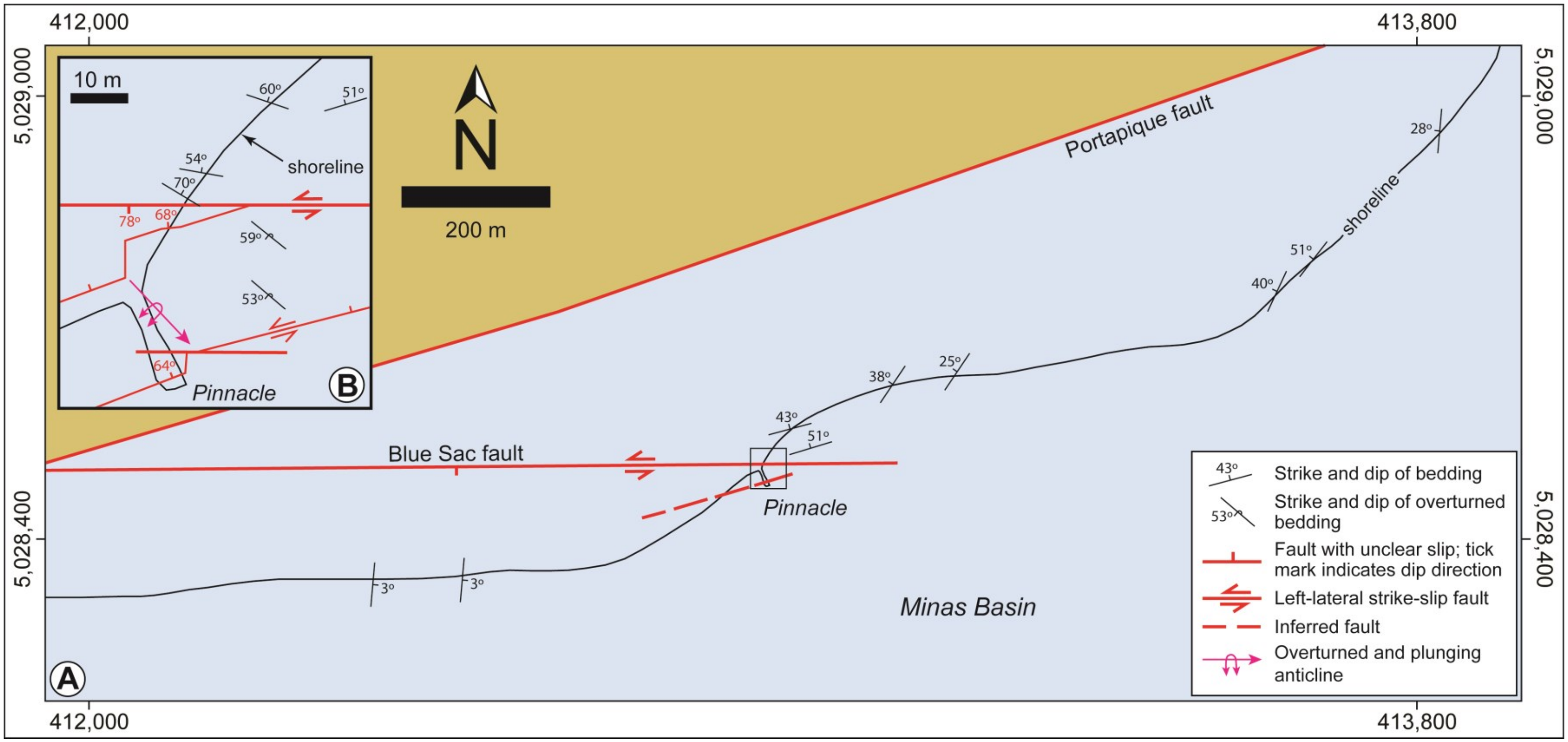

A8. Geologic map of Blue Sac (modified from Withjack et al. [2010] and Donohoe & Wallace [1982]). Some bedding data from Elder Brady (2003) and Baum (2006). See Figure 4 for color scheme.

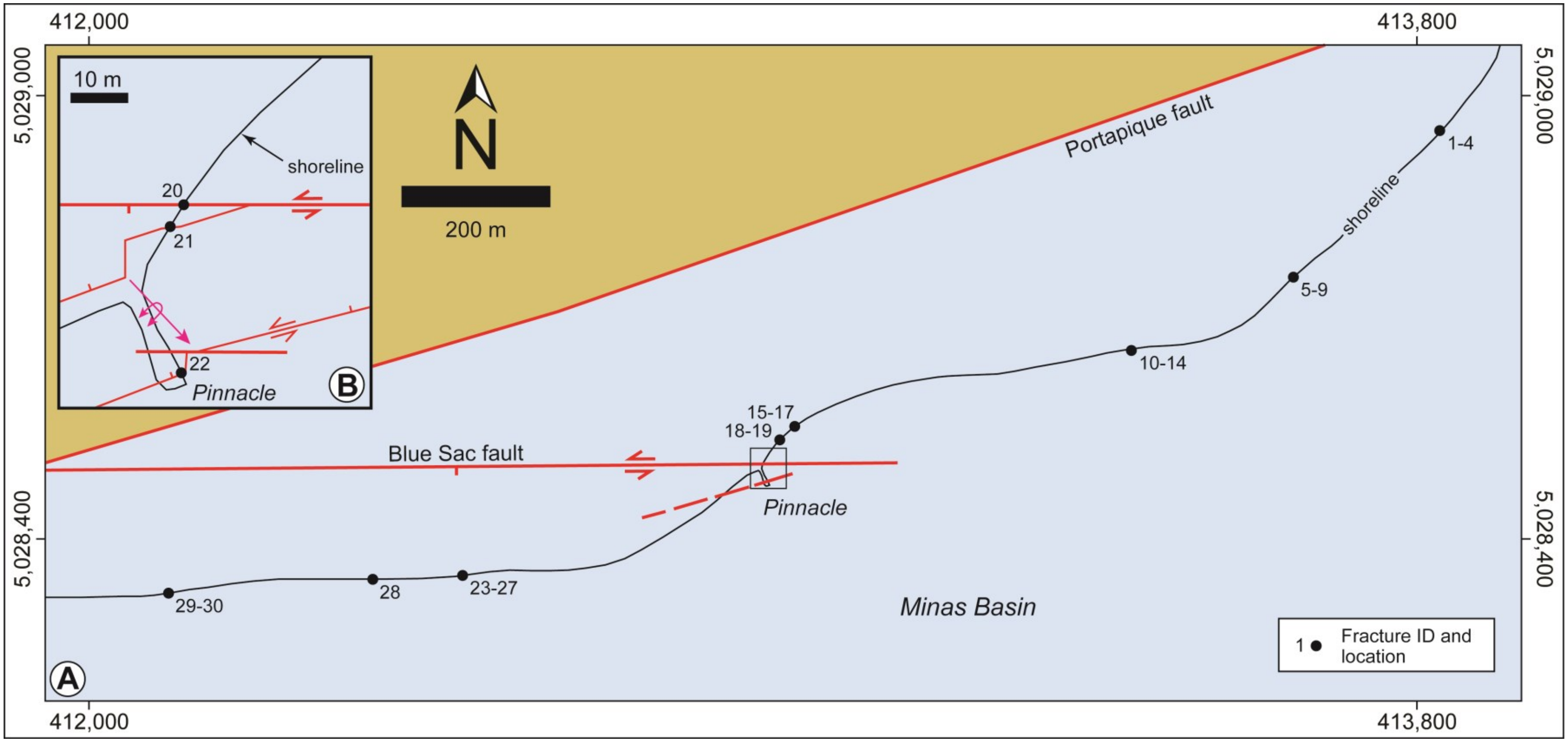

A9. Geologic map of Blue Sac (modified from Withjack et al. [2010] and Donohoe & Wallace [1982]) and location of fractures listed in Appendices 10 and 11. See Figure 4 for color scheme, and Appendix 8 for symbols and bedding information.

A10. Fractures measured at Blue Sac and used for stress inversion assuming fracture formation and/or reactivation after bedding rotation (Scenario 1).

Fracture ID	*Type of fracture*	*Plane*		*Slickenline*		*Sense*[a]	*Stress state*
		Dip direction (°)	*Dip angle (°)*	*Trend (°)*	*Plunge(°)*		
1	Fault	039	83	310	02	L	-
2[b]	Fault	070	90	160	07	L	-
3[b]	Fault	070	90	340	18	L	B1-C
4	Fault	023	85	294	16	L	-
5	Fault	066	90	156	16	R	B1-B
6	Fault	024	60	339	51	T	-
7	Fault	032	60	089	22	N	B1-A
8[c]	Fault	063	45	108	35	N	B1-A
9[c]	Fault	063	45	153	00	R	B1-B
10[d]	Fault	025	40	068	32	N	B1-A
11[d]	Fault	025	40	320	20	T	-
12[e]	Fault	065	43	065	43	N	B1-A
13[e]	Fault	065	43	134	19	N	B1-B
14[e]	Fault	065	43	037	33	R	B1-B
15[f]	Fault	065	41	138	15	R	B1-B
16[f]	Fault	065	41	134	18	R	B1-B
17	Fault	060	70	144	16	R	B1-B
18	Fault	023	80	297	24	R	B1-C
19	Fault	032	80	305	16	N	B1-C
20	Fault	185	78	270	21	L	B1-B
21	Fault	000	68	284	31	L	B1-B
22	Fault	352	64	290	44	L	B1-B
23	Fault	144	60	065	17	L	B1-B

[a] *N: normal; T: thrust/reverse; L: left-lateral strike slip; R: right-lateral strike slip*

[b-f] *Faults with multiple slickenlines. Repeated superscript indicate same fault and a different set of slickenlines*

Continues on next page

A10 (continued from previous page). Fractures measured at Blue Sac and used for stress inversion assuming fracture formation and/or reactivation after bedding rotation (Scenario 1).

Fracture ID	*Type of fracture*	*Plane*		*Slickenline*		*Sense*[a]	*Stress state*
		Dip direction (°)	*Dip angle (°)*	*Trend (°)*	*Plunge(°)*		
24	Fault	118	77	037	33	L	B1-B
25	Fault	144	66	060	13	L	B1-B
26	Fault	340	60	251	02	L	B1-B
27	Fault	240	70	150	00	R	B1-B
28	Fault	162	75	252	01	L	B1-B
29	Fault	240	70	326	10	L	B1-C
30	Fault	128	78	217	04	L	B1-B

[a] *L: left-lateral strike slip; R: right-lateral strike slip*

A11. Fractures from Blue Sac assuming formation and/or reactivation before the rotation of a nearby reference bedding plane (Scenario 2).

Fracture ID	*Type of fracture*	*Plane*		*Line*		*Sense*[a]	*Stress state*	*Reference bedding*
		Dip direction (º)	*Dip angle (º)*	*Trend (º)*	*Plunge(º)*			
1	Fault	219	81	133	21	L	B2-C	275º/28º
2[c]	Fault	247	65	166	18	L	B2-C	275º/28º
3[c]	Fault	247	65	334	07	L	B2-C	275º/28º
4	Fault	203	86	114	11	L	B2-C	275º/28º
5	Fault	237	69	183	56	I	-	308º/51º
6	Fault	055	61	327	04	R	B2-B	308º/51º
7	Fault	082	57	054	53	N	B2-D	308º/51º
8[d]	Fault	087	78	046	74	N	B2-D	308º/51º
9[d]	Fault	087	78	165	45	R	B2-A	308º/51º
10[e]	Fault	062	54	034	51	N	B2-D	295º/40º
11[e]	Fault	062	54	139	17	R	B2-A	295º/40º
12[f]	Fault	082	74	017	56	N	B2-D	295º/40º
13[f]	Fault	082	74	148	55	N	B2-A	295º/40º
14[f]	Fault	082	74	165	25	R	B2-A	295º/40º
15[g]	Fault	109	51	121	51	N	B2-A	345º/43º
16[g]	Fault	109	51	113	51	N	B2-A	345º/43º
17	Fault	078	65	129	54	N	B2-A	345º/43º
18	Fault	045	46	120	14	R	B2-A	343º/51º
19	Fault	053	52	122	25	R	B2-A	343º/51º
20	Fault	350	41	313	35	N	B2-A	031º/70º
21	Fault	340	43	311	40	N	B2-A	220º/53º [b]
22	Fault	328	45	328	45	N	B2-A	220º/53º [b]

[a] *N: normal; I: reverse; L: left-lateral strike slip; R: right-lateral strike slip*

[b] *Overturned*

[c-g] *Faults with multiple slickenlines. Repeated superscript indicate same fault and a different set of slickenlines*

Continues on next page

A11 (continued from previous page). Fractures from Blue Sac assuming formation and/or reactivation before the rotation of a nearby reference bedding plane (Scenario 2).

Fracture ID	*Type of fracture*	*Plane*		*Line*		*Sense*[a]	*Stress state*	*Reference bedding*
		Dip direction (º)	*Dip angle (º)*	*Trend (º)*	*Plunge(º)*			
23	Fault	145	58	065	14	L	B2-B	095º/03º
24	Fault	118	74	039	31	L	B2-B	095º/03º
25	Fault	145	64	060	11	L	B2-B	095º/03º
26	Fault	338	61	251	05	L	B2-B	095º/03º
27	Fault	241	72	330	02	R	B2-B	095º/03º
28	Fault	163	74	252	04	L	B2-B	095º/03º
29	Fault	241	72	326	12	L	B2-C	095º/03º
30	Fault	128	75	217	06	L	B2-B	095º/03º

[a] *L: left-lateral strike slip; R: right-lateral strike slip*

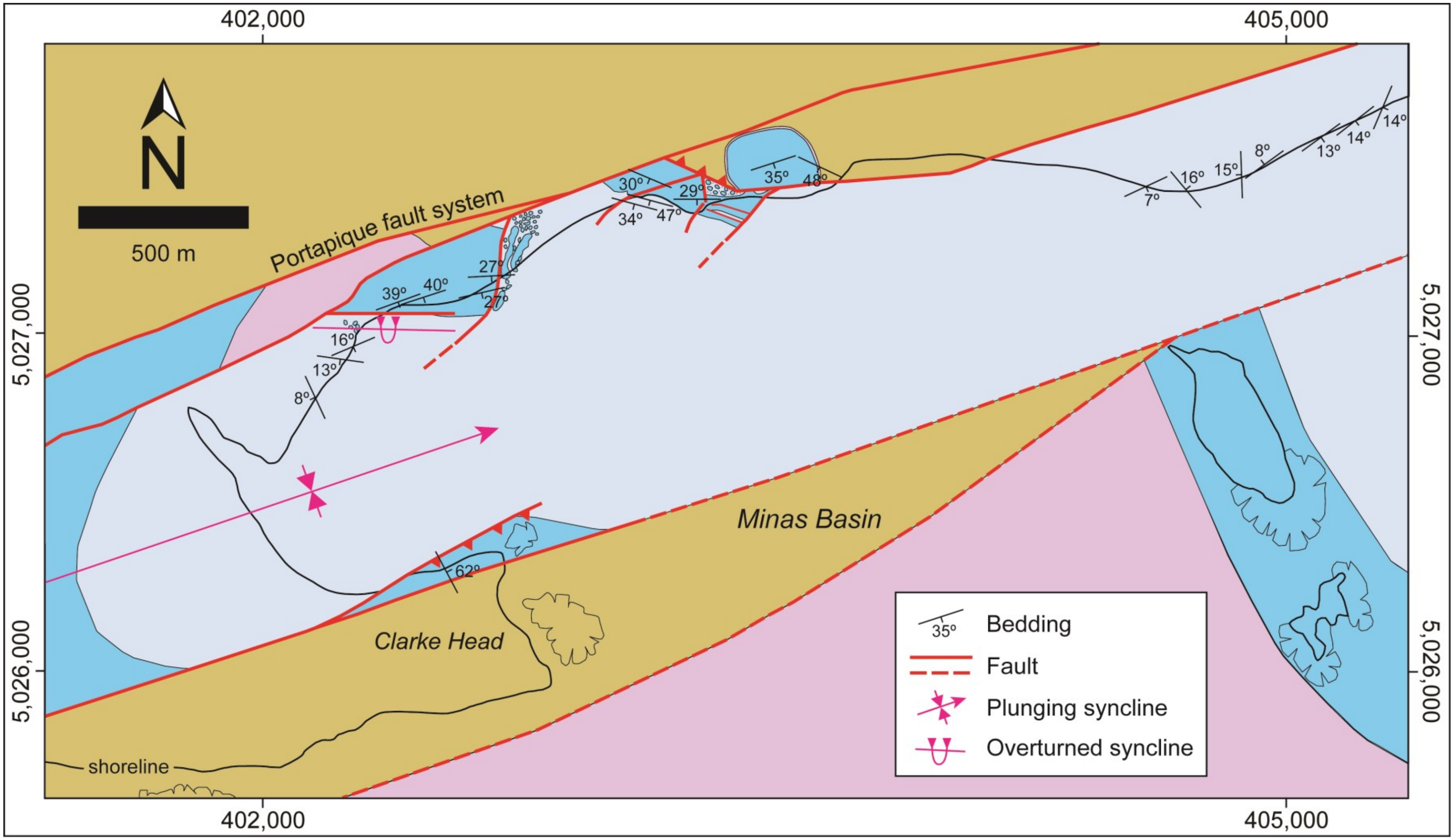

A12. Geologic map of Wasson Bluff (modified from Withjack et al., 2010). Some bedding data from Elder Brady (2003). See Figure 4 for color scheme.

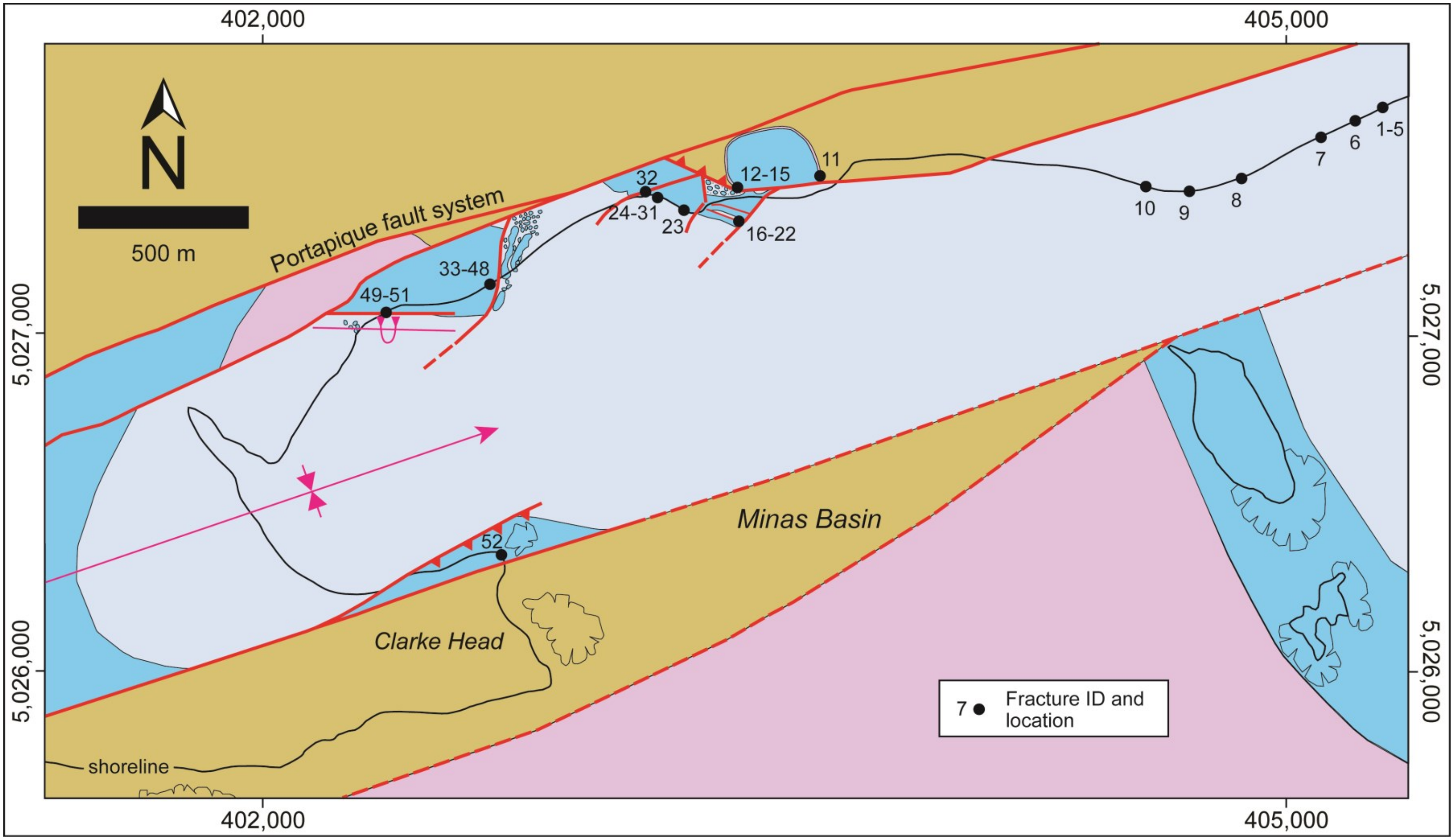

A13. Geologic map of Wasson Bluff (modified from Withjack et al., 2010) and location of fractures listed in Appendices 14 and 15. See Figure 4 for color scheme, and Appendix 11 for symbols and bedding information.

A14. Fractures measured at Wasson Bluff and used for stress inversion assuming fracture formation and/or reactivation after bedding rotation (Scenario 1).

Fracture ID	*Type of fracture*	*Plane*		*Slickenline*		*Sense*[a]	*Stress state*
		Dip direction (°)	*Dip angle (°)*	*Trend (°)*	*Plunge(°)*		
1	Fault	107	82	161	77	N	W1-A
2	Fault	287	50	285	50	N	W1-A
3	Fault	300	46	274	43	N	W1-A
4	Conjugate fault	300	46	274	43	L	-
5	Conjugate fault	260	78	184	49	R	-
6	Fault	255	47	299	38	N	-
7	Fault	310	64	249	45	N	W1-A
8	Fault	076	34	112	29	N	W1-A
9	Fault	291	53	256	47	N	W1-A
10	Fault	280	74	340	61	N	-
11	Fault	180	62	107	28	L	W1-C
12	Conjugate fault	312	72	255	59	N	W1-A
13	Conjugate fault	111	64	160	53	N	W1-A
14	Conjugate fault	138	79	228	00	L	W1-C
15	Conjugate fault	087	83	358	08	R	W1-C
16	Tension fracture	110	68	-	-	-	W1-A
17	Tension fracture	165	90	-	-	-	W1-B
18	Tension fracture	275	57	-	-	-	W1-A
19	Tension fracture	029	58	-	-	-	W1-B
20	Tension fracture	113	58	-	-	-	W1-A
21	Tension fracture	300	90	-	-	-	W1-A
22	Tension fracture	111	85	-	-	-	W1-A
23	Fault	280	71	003	19	R	W1-C
24	Conjugate fault	333	51	273	32	N	W1-A
25	Conjugate fault	105	71	172	49	N	W1-A
26	Conjugate fault	330	63	242	04	L	W1-C

[a] N: normal; L: left-lateral strike slip; R: right-lateral strike slip

Continues on next page

A14 (continued from previous page). Fractures measured at Wasson Bluff and used for stress inversion assuming fracture formation and/or reactivation after bedding rotation (Scenario 1).

Fracture ID	*Type of fracture*	*Plane*		*Slickenline*		*Sense*[a]	*Stress state*
		Dip direction (°)	*Dip angle (°)*	*Trend (°)*	*Plunge(°)*		
27	Conjugate fault	286	73	203	21	R	W1-C
28	Conjugate fault	287	70	011	15	R	W1-C
29	Conjugate fault	326	85	054	25	L	W1-C
30	Conjugate fault	309	74	234	43	N	W1-A
31	Conjugate fault	106	82	188	46	N	W1-A
32	Fault	170	90	080	26	L	W1-C
33	Tension fracture	287	61	-	-	-	W1-A
34	Tension fracture	064	87	-	-	-	-
35	Tension fracture	276	90	-	-	-	W1-A
36	Tension fracture	322	53	-	-	-	W1-B
37	Tension fracture	343	68	-	-	-	W1-B
38	Tension fracture	337	68	-	-	-	W1-B
39	Tension fracture	010	68	-	-	-	W1-B
40	Tension fracture	350	57	-	-	-	W1-B
41	Tension fracture	330	76	-	-	-	W1-B
42	Tension fracture	005	54	-	-	-	W1-B
43	Tension fracture	015	51	-	-	-	W1-B
44	Tension fracture	010	57	-	-	-	W1-B
45	Tension fracture	358	43	-	-	-	W1-B
46	Tension fracture	343	48	-	-	-	W1-B
47	Fault	250	88	336	63	T	-
48	Fault	282	56	335	42	R	-
49	Fault	003	82	092	08	L	W1-C
50	Conjugate fault	170	86	080	05	L	W1-C
51	Conjugate fault	131	90	041	06	R	W1-C
52	Fault	125	61	042	12	R	W1-C

[a] *N: normal; T: thrust/reverse; L: left-lateral strike slip; R: right-lateral strike slip*

A15. Fractures from Wasson Bluff assuming formation and/or reactivation before the rotation of a nearby reference bedding plane (Scenario 2).

Fracture ID	*Type of fracture*	*Plane*		*Slickenline*		*Sense*[a]	*Stress state*	*Reference bedding*
		Dip direction (°)	*Dip angle (°)*	*Trend (°)*	*Plunge(°)*			
1	Fault	107	68	137	65	N	W2-C	113°/14°
2	Fault	288	34	281	34	N	W2-A	113°/14°
3	Fault	299	60	268	56	N	W2-C	113°/14°
4	Conjugate fault	299	60	226	27	L	W2-C	113°/14°
5	Conjugate fault	261	90	171	43	R	W2-C	113°/14°
6	Fault	261	59	301	52	N	W2-A	142°/14°
7	Fault	311	77	236	47	L	W2-C	142°/13°
8	Fault	079	49	117	42	N	W2-C	268°/15°
9	Fault	282	62	268	61	N	W2-A	050°/16°
10	Fault	281	78	341	68	N	W2-A	155°/07°
11	Fault	142	25	132	24	N	W2-A	205°/48°
12	Conjugate fault	133	77	210	46	L	-	162°/35°
13	Conjugate fault	089	47	161	18	R	-	162°/35°
14	Conjugate fault	129	48	052	13	L	-	162°/35°
15	Conjugate fault	080	76	41	003	R	-	162°/35°
16	Tension fracture	096	69	-	-	-	W2-C	195°/34°
17	Tension fracture	160	61	-	-	-	W2-B	195°/34°
18	Tension fracture	298	58	-	-	-	W2-A	195°/34°
19	Tension fracture	207	89	-	-	-	-	195°/34°
20	Tension fracture	092	60	-	-	-	W2-C	195°/34°
21	Tension fracture	118	82	-	-	-	W2-C	195°/34°
22	Tension fracture	107	83	-	-	-	W2-C	195°/34°
23	Fault	288	78	004	48	R	W2-A	180°/29°
24	Conjugate fault	344	90	254	13	N	W2-D	195°/47°
25	Conjugate fault	091	77	180	04	R	W2-D	195°/47°
26	Conjugate fault	155	81	070	27	L	W2-D	195°/47°

[a] *N: normal; L: left-lateral strike slip; R: right-lateral strike slip*

Continues on next page

A15 (continued from previous page). Fractures from Wasson Bluff assuming formation and/or reactivation before the rotation of a nearby reference bedding plane (Scenario 2).

Fracture ID	*Type of fracture*	*Plane*		*Slickenline*		*Sense*[a]	*Stress state*	*Reference bedding*
		Dip direction (°)	*Dip angle (°)*	*Trend (°)*	*Plunge(°)*			
27	Conjugate fault	298	79	023	26	R	W2-D	195°/47°
28	Conjugate fault	301	78	007	62	R	W2-A	195°/47°
29	Conjugate fault	139	65	088	53	L	W2-A	195°/47°
30	Conjugate fault	133	84	222	03	L	W2-D	195°/47°
31	Conjugate fault	100	84	010	01	R	W2-D	195°/47°
32	Fault	161	48	109	35	L	W2-A	195°/47°
33	Tension fracture	298	73	-	-	-	W2-A	177°/27°
34	Tension fracture	245	83	-	-	-	W2-C	177°/27°
35	Tension fracture	095	86	-	-	-	W2-C	177°/27°
36	Tension fracture	329	76	-	-	-	W2-B	177°/27°
37	Tension fracture	164	86	-	-	-	W2-B	177°/27°
38	Tension fracture	158	86	-	-	-	W2-B	177°/27°
39	Tension fracture	189	86	-	-	-	W2-B	177°/27°
40	Tension fracture	351	84	-	-	-	W2-B	177°/27°
41	Tension fracture	150	80	-	-	-	W2-B	177°/27°
42	Tension fracture	004	81	-	-	-	W2-B	177°/27°
43	Tension fracture	011	77	-	-	-	W2-B	177°/27°
44	Tension fracture	008	83	-	-	-	W2-B	177°/27°
45	Tension fracture	358	70	-	-	-	W2-B	177°/27°
46	Tension fracture	346	74	-	-	-	W2-B	177°/27°
47	Fault	253	81	258	81	T	W2-C	177°/27°
48	Fault	294	70	323	68	N	W2-A	167°/27°
49	Fault	186	62	272	07	L	W2-D	160°/39°
50	Conjugate fault	174	48	261	02	L	-	160°/39°
51	Conjugate fault	124	57	050	23	R	-	160°/39°
52	Fault	169	55	213	46	R	-	062°/62°

[a] *N: normal; T: thrust/reverse; L: left-lateral strike slip; R: right-lateral strike slip*

Appendix B: Data separation using Win_TENSOR

After separating of the data by site, the second separation requires the PBT tool (i.e., P: compressional axis; T: tensional axis; B: null axis) provided in Win_TENSOR. This tool, which applies the direct inverse method of Angelier (1984), assumes that sets of faults lacking of antithetic faults have a σ_1 oriented 45º away from the maximum shear vector (i.e., slickenline) and not the average value of 30º proposed in Anderson's (1951) theory. Faults formed and/or reactivated during the same stress state will have similar principal stress directions; therefore, I separate clusters of similar stress directions for faults with similar strikes, and combine subsets with the same clusters.

Subsequently, the Rotational Optimization tool in Win_TENSOR allows the adjustment of the stress ratio and the orientation of the mean principal stress axes, allowing σ_1 to be 30º away from the maximum shear vector. Such operation reduces significantly the global misfit of the data. The program applies least-squares minimization to calculate the average principal stress directions and the angle of deviation of each data point relative to the mean value.

After the correction of the principal stress axes for faults, I incorporate the conjugate faults and tension fractures in each subset, and reject the fractures that do not fit the model within an arbitrary maximum global deviation value of 30º (Kipata et al., 2012). This number can be lower; however, it would produce more rejected data. Conversely, higher misfit angles include fractures with unrealistic mechanical compatibility. With the inclusion and rejection of data points, I adjust the orientation of the average principal stress axes and stress ratio until I obtain a stable tensor solution, in which data and the global deviation is within the range of the 30-degree threshold.